Design and Characterization of the Measurement Electronics for a Magnetic Induction Tomography Imaging System

Hsin-Yu Wei

A dissertation submitted to the Department of Electrical Engineering,
University of Cape Town, in fulfilment of the requirements
for the degree of Master of Science in Engineering.

Cape Town, September 2008

Declaration

I declare that this dissertation is my own, unaided work. It is being submitted for the degree of Master of Science in Engineering in the University of Cape Town. It has not been submitted before for any degree or examination in any other university.

Signature of Author .....Signed by candidate.....

Cape Town

17 September 2008

Abstract

A data acquisition transceiver circuit for magnetic induction tomography (MIT) has been developed. MIT is a type of tomography technique that is sensitive to the conductivity of objects, and which can be used in both industrial and biomedical applications. A detailed design process of the MIT transceiver board and the coupling sensor coils are presented in this dissertation.

For the purpose of testing the designed hardware, a three channel MIT measuring system was assembled, and various experiments were run on the system. Several different samples with high conductivity (metal sheets) or low conductivity (saline solution) were used to test the performance of the designed transceiver. Its suitability for being applied to the actual MIT system could then be assessed. The noise characteristics and stability of the system were also characterised. A complete eight channel MIT measurement system is presently being assembled based on the prototypes presented in the dissertation.

The results obtained from the experiments are very promising. The construction of the multi-channel MIT system and the image reconstruction can confidently be expected in future development.

To my family

Acknowledgments

My sincere thanks to all the people who gave of their knowledge and time to this research dissertation, as this dissertation would not have been possible without their help.

Specifically, thanks to:

- Dr. Andrew Wilkinson, my supervisor, for all his help in many ways throughout the dissertation. He guided me into the right direction with his knowledge and experience whenever I needed it. I would also like to thank him for his patience and the time he spent with me when I encountered the problems.
- Mr. Chris Wozniak, the principal technical officer of the Electrical Engineering Department for all his advice in the development of the circuit board.
- Mr. Phillips Titus, for helping me to solve various mechanical problems with my MIT hardware system.
- All the post-graduate students working in the Signal Lab, Andrew Markham, Kushwant Mussai, Rachel Chao and Ross Macfarlane Allardice, for their creative suggestions for my dissertation and the time they spent with me during lunch breaks.
- My family, for their moral support in Taiwan.

Contents

Declaration i

Abstract ii

Acknowledgements iv

List of Symbols xiii

Acronyms xiv

Nomenclature xv

1 Introduction 1

1.1 What is Tomography? . . . 1

1.2 Electrical Tomography . . . 2

1.3 Applications of MIT . . . 6

1.3.1 Industrial MIT . . . 6

1.3.2 Biomedical MIT . . . 6

1.4 Aims and Objectives of the Dissertation . . . 7

1.5 Plan of Development . . . 8

2 Literature Review 9

2.1 Overview of MIT Systems . . . 9

2.1.1 Mutual Inductance . . . 10

2.1.2 Principles of MIT . . . 11

2.1.3 Existing Industrial MIT Systems . . . 12

2.1.4 Existing Biomedical MIT Systems . . . 15

2.2 Summary of Existing MIT Systems . . . 20

2.2.1 Sensor Coil . . . 22

2.2.2 Operating Frequency . . . 22

2.2.3 Demodulation Techniques . . . 22

2.2.4 Screening . . . 23
2.3 MIT System Architecture for the Prototype System . . . 23

3 Induction Coil Sensor Design 26
3.1 Air-Core Coil . . . 27
3.2 Ferromagnetic-Core Coil . . . 27
3.3 PCB Planar Coil . . . 28
3.4 Gradiometer . . . 28
3.5 Screening . . . 29
3.6 My Coil Design and Operating Frequency Selection . . . 30
3.7 Electronic Circuits Connected to the Coil Sensors . . . 33
3.7.1 Transmitter . . . 33
3.7.2 Receiver . . . 34

4 Signal Demodulation 36
4.1 Operation Theory of Synchronous Detection . . . 37
4.2 Mixer Selection . . . 39
4.2.1 Analog Device - AD8333 [55] . . . 41
4.2.2 Analog Device - AD607 [56] . . . 42
4.3 Using the AD607 [56] . . . 44
4.3.1 Bias System . . . 45
4.3.2 Diode Clipping Circuit . . . 46
4.3.3 IF Amplifier . . . 47
4.3.4 PLL loop filter . . . 48
4.3.5 Fast PRUP Control Signal . . . 49
4.3.6 Gain Scaling and Gain Distribution . . . 50
4.3.7 General Circuit Layout Design . . . 50

5 Post Demodulation Signal Conditioning 52
5.1 Low Pass Filter . . . 53
5.2 Level Shifter . . . 55
5.2.1 Non-inverting Level Shifter . . . 55
5.2.2 Inverting Level Shifter . . . 56

6 Channel Switching, Voltage Gain Control and Data Acquisition 57
6.1 Channel Switching and Voltage Gain Control . . . 58
6.2 Data Acquisition . . . 61

7 Results **65**
7.1 System Setup . . . 66
7.2 Transceiver Board Testing . . . 67
7.2.1 I/Q Demodulation Testing . . . 68
7.2.2 Checking the current measurement capability . . . 68
7.3 Noise Characteristics . . . 71
7.4 Measurement - Saline Solution . . . 73
7.5 Measurement - Metal . . . 78
7.6 Stability . . . 80
7.7 Phase Skew . . . 82

8 Tomography Image Reconstruction **83**
8.1 General Algorithm . . . 83
8.1.1 The Forward Problem . . . 83
8.1.2 Inverse Problem . . . 85

9 Conclusion and Recommendations **88**

A Mathematical Model for MIT system **90**

B High Speed PCB Layout Guide **93**
B.1 Decoupling of Power Supplies . . . 93
B.2 System Grounding . . . 94
B.3 Selection of External Components . . . 95
B.4 Parasitic . . . 96

C Data Acquisition Card **98**

D Comedi Instruction **100**
D.1 Using Linux Debian Archive . . . 100
D.2 Using the Comedi website . . . 101

E MIT Transceiver Circuit Schematics **102**

Bibliography **103**

List of Figures

1.1 The ERT data capture system developed at the UCT and its computed image (images from [8]). 4

1.2 The ECT data capture system developed at UCT and its computed image (images from [9]). 4

1.3 MIT data capture system and computed image (images from [11]). 5

2.1 MIT system block diagram. 9

2.2 Mutual flux linkages between two coils. 10

2.3 Magnetic field at a thin disk due to a small excitation coil (illustration from [24]). 11

2.4 Phaser diagram representing the primary (B) and secondary (ΔB) magnetic fields detected in a biomedical MIT system (illustration from [5]). . 12

2.5 (A) Cross-sectional structure of Yu's MIT system. (B) Reconstruction image where a bar is placed within the measuring space (illustration from [15]). 13

2.6 Cross-sectional structure of Lyon et al.'s MIT system (illustration from [26]). 14

2.7 Photography of Ma et al.'s MIT system and the physical sensor structure (images from [27]). 15

2.8 Reconstruction image where different numbers of metal bars are placed within the measuring space (images from [27]). 15

2.9 (A) Front-end structure of Korjenevsky et al.'s MIT system. (B) Reconstructed image where several saline water bottles with different concentrations were placed within the measuring space (images from [11]). . . . 16

2.10 Front-end structure of Watson et al.'s MIT system (image from [33]). . . . 17

2.11 (A) Cross-sectional structure of Goss's MIT system. (B) Reconstruction image where a water tank was placed within the measuring space (images from [38]). 18

2.12 Schematic of H. Scharfetter et al.'s two channel MIT system (illustration from [17]). 19

2.13 Schematic of the 8 channel ZFGRAD system (illustration from [39]). . . 20

2.14 Result of 3D reconstructed images: (A) Top view, (B) Side view, (C) Front view. The dotted circle shows the position of the actual perturbation (images from [39]). 20
2.15 Conductivity measurement of biological tissue at various frequency (graph from [17]). 23
2.16 A complete MIT system block diagram. 24
2.17 Perspex cylindrical tube with a 20 cm diameter 25
2.18 Agilent 33250A signal generator. 25

3.1 A simple sensor of a magnetic field in the form of a coil (image from [52]). 26
3.2 An example of a PCB planar coil and a PCB electrostatic screening. . . . 28
3.3 Operating principle of a gradiometer sensor (illustration from [52]). . . . 29
3.4 5 turns screened coil with inductance = 2.3 μH. 30
3.5 5 turns + 5 turns balanced screened coil with inductance = 6.9 μH. 31
3.6 The magnitude of the input impedance of a 5 + 5 turns balanced coil. . . . 32
3.7 MIT transceiver circuit with a balanced coil. 33
3.8 Transmitting circuit. 34
3.9 Receiver circuit. 35

4.1 An example of using XOR Gate to extract phase difference information. . 37
4.2 The principle of the synchronous detection technique. 37
4.3 Phasor representation of $Ae^{-j\theta}$. 39
4.4 Block diagram of the AD8348 architecture (diagram from [54]). 40
4.5 Functional block diagram of the AD8333 (diagram from [55]). 41
4.6 Size comparison between a AD8333 and a R1 coin. 42
4.7 Functional block diagram of the AD607 (diagram from [56]). 43
4.8 Schematic diagram of the AD607. 45
4.9 Suggested methods for AD607 input biasing (diagrams from [56]). 46
4.10 Schematic diagram of a diode clipping circuit. 46
4.11 The comparison between the 4 Vp-p, 10 MHz input signal and the output signal of the diode clipping circuit (A) with and (B) without the phase compensation capacitor. 47
4.12 Simplified schematic diagram of the IF interface (diagram from [56]). . . 48
4.13 Maximum signal levels at each stage in the AD607 (diagram from [56]). . 50

5.1 Schematic diagram of one stage Sallen-Key low pass filter. 53
5.2 Sallen-Key low pass filter's (A) schematic diagram and (B) its simulated frequency response. 54

5.3 Schematic diagram of a non-inverting level shifter. 55
5.4 Schematic diagram of an inverting level shifter. 56

6.1 Circuitry block diagram. 57
6.2 Final PCB layout of the analog measurement electronics. 58
6.3 Signal flows in the transmitting mode. 59
6.4 Signal flows in the receiving mode. 59
6.5 The dsPIC33FJ256GP710 on the Explorer 16 evaluation board, with a MPLAB ICD2 debugger. 60
6.6 TLV5630 circuit board on the Explorer 16 daughter board. 61
6.7 (A) NI PCI-6070E data acquisition card and NI CB-68LP connector block, (B) Shielded SH68-68-EP cable (images from [60]) 62
6.8 A complete system level block diagram of the MIT system. 63
6.9 Main Board. 63

7.1 One channel of the MIT system. 65
7.2 Perspex tube with the sensor coils attached. 66
7.3 System block diagram of the initial experiment setup. 67
7.4 The changes of I/Q outputs in (A) Y-t mode and X-Y mode when the phase difference varies from (B) 0° to (C) 180°(D) 45° and (E) 135°. . . . 69
7.5 The change of I/Q outputs in X-Y coordinates when the magnitude of driving signal changes from (A) 4 Vp-p to (B) 2 Vp-p. 70
7.6 The predicted current flow versus the measured current flow. 70
7.7 Uncorrelated I/Q outputs and the calculated phase and magnitude measurements. 72
7.8 The system setup for the saline measurement. 74
7.9 Saline bottles. 74
7.10 Phase change versus the saline bottle position along the x-axis. 75
7.11 Phase change versus the saline bottle position along the y-axis. 76
7.12 Phase change and magnitude measurement when the 5 % saline bottle is moved along the y-axis. 76
7.13 Measured phase shift as a function of position of the test object along the x-axis and the y-axis in the single channel measurements (graphs from [11]). 77
7.14 Phase measurement comparison when operating at 10 MHz and 3 MHz. . 78
7.15 (Top, from left to right): A 0.5 mm thick aluminum sheet, a 1 mm thick steel sheet and a 2 mm thick aluminum sheet. (Bottom): Edge view of the metal sheets. 79

7.16 Magnitude change versus the metal sheet position along the x-axis. 80
7.17 Output stability result: plot of I(t) and Q(t) over five hours. 81

8.1 Flow chart of the Gauss Newton Method. 86

A.1 Model of the electromagnetic coupling between a cylindrical sample and a two coil system (illustration from [25]). 90

B.1 AC impedance versus frequency with different capacitor values (graph from [71]). 93
B.2 Pulse response with (green) and without (red) ground plane (graph from [71]). 95
B.3 Typical op-amp circuit, as (A) designed and (B) with parasitic (images from [71]). 96
B.4 Additional peaking caused by a 1 pF stray capacitance (graph from [71]). 97

C.1 Layout of CB-68LP connector board (diagram from[74]). 98
C.2 Pin out for NI PCI-6070E DAQ Card (diagram from [74]). 99

E.1 MIT transceiver schematics. 102

List of Tables

1.1 Characteristics and applications of different tomography techniques (table from [4]). 3

1.2 Sensing techniques of an electrical tomography system (table from [15]). 6

2.1 Summary of Existing Tomography System. 21

3.1 Coil's inductance and impedance (at 10 MHz) with respect to different number of turns. 31

7.1 Results of the measured current flow with different resistor values. 70

7.2 Characteristics of aluminum and steel. 78

7.3 Phase skew versus driving amplitude. 82

9.1 Characteristics of the transceiver circuits. 88

List of Symbols

B — Magnetic field, which has the SI units of teslas - (T)
L — Magnetic inductance, which has the SI units of henry - (H)
σ — Electrical conductivity - (Sm^{-1})
ε — Permittivity - (Fm^{-1})
μ — Permeability (Electromagnetism) - (Hm^{-1})
Φ — Magnetic flux (Wb)
I — In-phase output of the synchronous detector
Q — Quadrature output of the synchronous detector
H — Magnetic field intensity, which has the SI units of Amperes/meter - (Am^{-1})
E — Electric field, which has the SI units of volts/meter - (Vm^{-1})

Acronyms

ADC	—	Analog to Digital Converter
AGC	—	Automatic Gain Control
COMEDI	—	Control and Measurement Device Interface
DAC	—	Digital to Analog Converter
DAQ	—	Data Acquisition
DDS	—	Direct Digital Synthesis
ECT	—	Electrical Capacitance Tomography
EIT	—	Electrical Impedance Tomography
EMI	—	Electro-Magnetic Interference
EMT	—	Electro-Magnetic Tomography
FEM	—	Finite Element Method
IC	—	Integrated Circuit
MIT	—	Magnetic Induction Tomography
PCB	—	Printed Circuit Board
PGRAD	—	Planar Gradiometer Sensor
PLL	—	Phase Lock Loop
PSD	—	Perturbation to Signal Ratio
SPICE	—	Simulation Program with Integrated Circuit Emphasis
SPI	—	Serial Peripheral Interface
SQUID	—	Superconducting Quantum Interference Device
VFQO	—	Variable Frequency Quadrature Oscillator
UCT	—	University of Cape Town
UHF	—	Ultra-High Frequency
ZFC	—	Zero Flux Coil
ZFGRAD	—	Zero Flux Gradiometer

Nomenclature

Conductivity—Electrical conductivity is a measure of a material's ability to conduct an electric current. When an electrical potential difference is placed across a conductor, its movable charges flow, giving rise to an electric current.

Direct Digital Synthesis (DDS)— DDS is an electronic method of producing an analog waveform (usually a sine wave) digitally from a single, fixed source frequency. Because operations within a DDS device are primarily digital, it can offer fast switching between output frequencies, fine frequency resolution, and operation over a broad spectrum of frequencies (Wikipedia, the free encyclopedia).

I/Q demodulation—In-phase and Quadrature Demodulation, sometimes it is also known as Synchronous Detection

Permittivity—Permittivity is a physical quantity that describes how an electric field affects and is affected by a dielectric medium, and is determined by the ability of a material to polarize in response to the field, and thereby reduce the total electric field inside the material. Thus, permittivity relates to a material's ability to transmit an electric field.

Permeability—Permeability is the degree of magnetization of a material that responds linearly to an applied magnetic field.

Chapter 1

Introduction

1.1 What is Tomography?

Tomography is a technique that can create an image of the internal physical properties of an object. The word 'tomography' is derived from the Greek words 'tomos', which means 'a slice, a section' and 'graph', which means 'image'. The formal definition of the word 'tomography' in the *Oxford English Dictionary* [1] is:

"Radiography in which an image of a predetermined plane in the body or other object is obtained by rotating the detector and the source of radiation in such a way that points outside the plane give a blurred image. Also in extended use, any analogous technique using other forms of radiation. "

The *McGraw-Hill Dictionary of Scientific and Technical Terms* [2] gives the following definition for tomography:

"The technique of making radio-graphs of plane sections of a body or an object; its purpose is to show detail in a predetermined plane of the body, while blurring the images of structures in other planes. "

One need to be aware of the definitions above given in [1] *and* [2] are not general enough to cover all the tomography techniques. Those definitions only define one specific area of the tomography, which is called 'hard field tomography', such as X-ray and γ-ray tomography. However, hard field tomography has completely different characteristics to 'soft field tomography', which will be discussed mainly in this dissertation. They are different in a way that, for hard field tomography, such as X-ray, the path of the transmitting signal is in a straight line pattern, and the only factor that can affect the signal strength is the material along that path, regardless the position of the material. In the case of soft field tomography, such as magnetic induction tomography (MIT), there are other factors that can influence the transmitting signal, like the position of the material in the measurement volume, as well as the distribution of electrical parameters (conductivity and permeability) inside and outside the measuring region. This presents a great difficulty when computing the image reconstruction algorithm for soft field tomography [3].

At present, there is a huge demand for tomographic techniques in scientific and industrial fields, as these fields often require a detailed instrumentation system to examine the internal structure of an object (human body, vessels...etc). The *Wikipedia*, the on-line encyclopedia states the following (http://en.wikipedia.org/wiki/Tomography):

"Tomography is used in medicine, archeology, biology, geophysics, oceanography, materials science, astrophysics and other sciences. In most cases it is based on the mathematical procedure called tomographic reconstruction. "

During the past decades, several tomography systems have been developed using several different physical phenomena. Each physical phenomenon will have its own suitable measuring properties and constraints, such as target range and object size. Table 1.1 [4] summarises a number of existing tomography techniques with their characteristics and suitable applications:

This dissertation will mainly focus on magnetic induction tomography (MIT), which falls within the electrical tomography category. Therefore the other non-electrical tomographic techniques will not be discussed further in this chapter.

1.2 Electrical Tomography

Electrical tomography is a technique that can image the passive electromagnetic properties of material non-invasively. In the last 20 years, electrical tomography has been applied to a wide variety of diverse applications, but most of this interest has been in the areas of medical imaging [5], where the cross sectional images of human body can be examined, and industrial imaging, to visualise and monitor the distribution of material in vessels and pipelines. Most of these applications have focused on a low frequency (<20 MHz) approach [5, 6]. Electrical imaging has also been used in environmental monitoring for tracking the migrations of pollutants underground [7]. Electrical tomography systems have several advantages; despite their relatively modest image resolution, they have proved to be very useful because of their high imaging speed, low cost and non-invasive characteristic.

The oldest technique of electrical imaging is electrical impedance tomography (EIT) [5], which normally involves attaching multiple electrode sensors around the measuring object, such as water vessels, pipelines and human bodies. Current signals are injected into a pair of electrodes, and 'trans-impedance' measurement are taken from all other pairs of electrodes. The cross sectional image of electrical conductivity and permittivity can then be computed from the measurements. EIT is sometimes referred to as electrical resistance tomography (ERT), if the reactive capacitive component of the measured impedance is negligible. Figure 1.1 shows the ERT data capture system developed at the University of Cape Town (UCT) and its computed image.

	Tomography Technique	Characteristics	Applications
EM (Hard field)	γ-ray	Radio-active sources Fast scanning speed Potentially fast	Industrial applications
	X-ray	High resolution Mechanically scanned Radiation confinement	Medical imaging Industrial applications
	UV Optical Infrared	Fast Optical access	Micro-structural Medical monitoring
	Millimeter Wave	System component Emerging	Air traffic monitoring
EM (Soft field)	Microwave	Fast Moderate resolution (Wavelength dependent)	Thermal mapping of reactors
	Capacitance (ECT)	Low resolution	Passive electric properties mapping
	Impedance (EIT)	Fast	
	Inductance (MIT)	Robust	
		Low cost	
Nuclear Particle	Positron Emission	Uses labeled particles Similar to CT reconstruction algorithm	Medical imaging
	Neutron	High resolution Pulse or radioactive source Radiation confinement	Micro-structural monitoring (Medical)
Others	Nuclear Magnetic Resonance		Micro-structural monitoring (Medical)
	Ultrasound	High Resolution Phase array for beam steering	Medical imaging Industrial monitoring
	Thermal Conduction (Heat Flux)	Slow Soft field	

Table 1.1: Characteristics and applications of different tomography techniques (table from [4]).

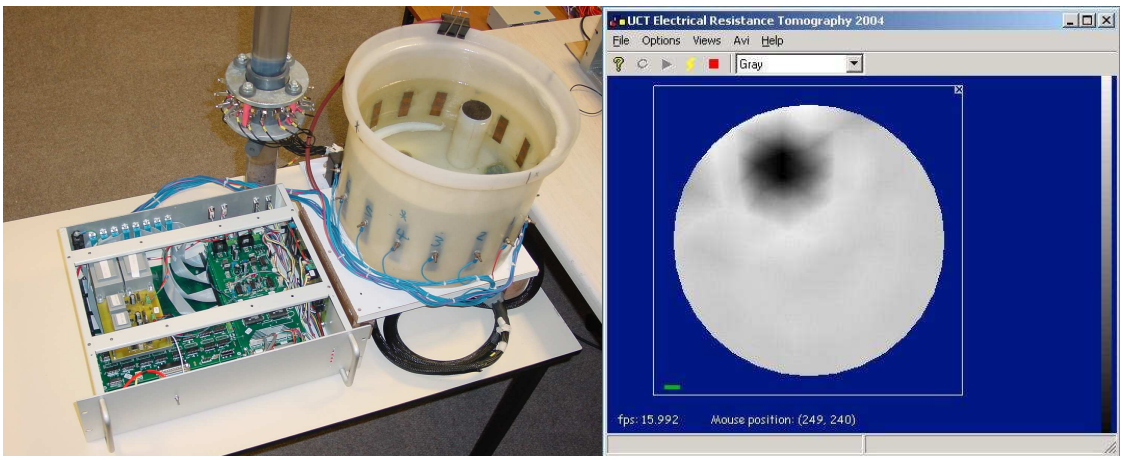

Figure 1.1: The ERT data capture system developed at the UCT and its computed image (images from [8]).

Electrical capacitance tomography (ECT) is another electrical tomographic technique [9]. It is very similar to EIT in that it also uses an array of sensors (in metal plate form) and applies an electric field to the material. It differs in the way the measurements are taken: in EIT, current is usually injected into a pair of driving electrodes, and the voltages are then measured between all the other sensing electrode pairs, whereas in ECT, one electrode is usually voltage driven, and one or more of the other electrodes are grounded into a transimpedance amplifier (which measures the current), and the current signal is then measured between each unique pairs of sensing plates. ECT is able to image variation in permittivity inside a medium, and is well suited to applications where the impedance between electrodes is dominantly capacitive, such as monitoring/imagine pipe flow of non-conducting fluids (e.g. oils) and rotten wood detection. The ECT sensor plates are usually attached to an insulating boundary with appropriate shielding. Figure 1.2 shows the ECT data capture system developed at the UCT and its computed image.

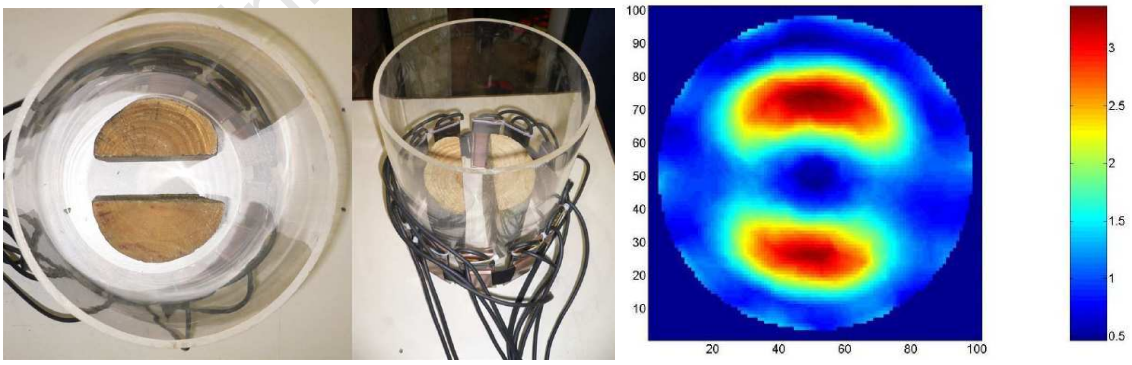

Figure 1.2: The ECT data capture system developed at UCT and its computed image (images from [9]).

The most recent technique is magnetic induction tomography (MIT) [5, 10], an electrical tomography technique which is based on inductance measurement, by using induction coil sensors. The arrangement of the coils is similar to EIT and ECT. By injecting a sinusoidal signal into an excitation coil, a magnetic field can be generated which induces

an eddy current on (or inside) the measuring object. The magnetic field caused by the eddy current on the measuring object is then detected by the rest of the sensing coils. By measuring these changes of mutual inductance between coils, the cross section of electromagnetic properties can be computed from the measurements. It should be noted that MIT is sensitive to all three passive electromagnetic properties: conductivity, permeability and permittivity [5], although conductivity is usually the focus. The technique has also been referred to variously as mutual inductance tomography, eddy current tomography and electromagnetic tomography (EMT). Figure 1.3 shows the MIT data capture system published in paper [11] and its computed image.

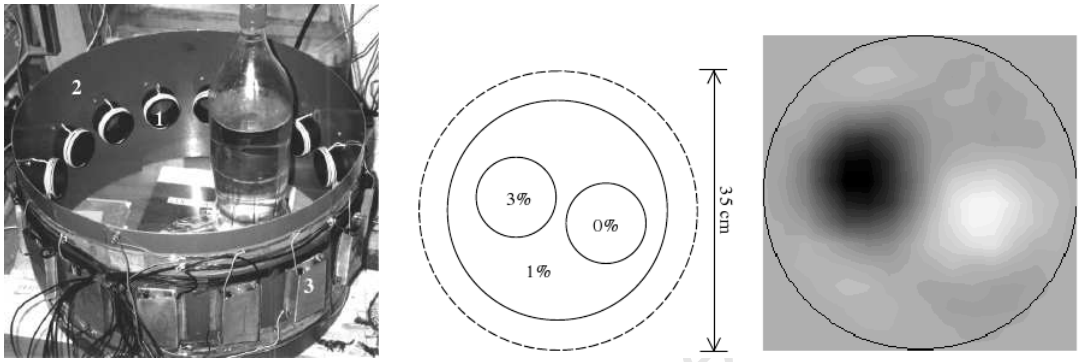

Figure 1.3: MIT data capture system and computed image (images from [11]).

There are some hybrid systems which implement multiple electrical tomography techniques. Those systems normally involve combining the transmitter and receiver from different tomography systems, for example, the system reported in [12], has the magnetic excitation with coils and measurement of surface potentials with electrodes. The system in [13] has a pair of current injection electrodes and an external magnetic field sensing coils. And the system reported in [14] takes the measurements of both electric field and magnetic field from the electrodes and the coil respectively, the measured magnetic field is induced by the current excited in the object by the standard EIT procedures.

Table 1.2 is a comparison of three different types of electrical tomography, namely ECT, ERT and MIT.

Tomographic Technique	Sensor type	Sensor arrangement	Measure Values	Range of property imaged	Typical material
Capacitance	Capacitive plates	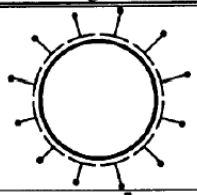	Capacitance	**Relative permittivity** ε_r 10^0 to 10^2 **Conductivity** Low σ 10^{-1} S/m	**Oil and water**
Resistance	Electrodes	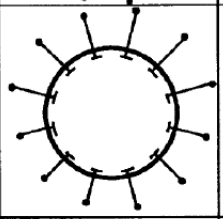	Resistance (Impedance)	**Conductivity** wide σ 10^{-1} to 10^7 S/m , **Relative permittivity** ε_r 10^0 to 10^2	**Water/ saline**
Electro-magnetic	Coils	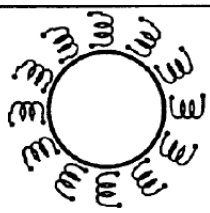	Self/ Mutual Inductance	**Conductivity** High σ 10^2 to 10^7 S/m, **Relative permeability** μ_r 10^0 to 10^4	**Metal/ minerals and water**

Table 1.2: Sensing techniques of an electrical tomography system (table from [15]).

1.3 Applications of MIT

1.3.1 Industrial MIT

As is shown in Table 1.2, the sensors of a MIT system are sensitive to and more appropriate for measuring materials with high electrical conductivity and high permeability. As a result, the majority of MIT systems for the industry have been designed for detecting metallic or ferromagnetic objects. Several industrial applications for MIT have been suggested in [5]:

- Tracking ferrite labeled powder in separation processes.
- Foreign body detection (metal) in food, textiles or pharmaceuticals.
- Detection of defects in metal components (e.g. surface corrosion on metal).
- Monitoring of bulk ionized water in pipelines.

1.3.2 Biomedical MIT

In the past few decades, EIT has developed as a medical imaging technique in which an image of the conductivity or permittivity of part of the body can be measured from electrical measurements. Typically, several conducting electrodes are attached to the skin of the human body and a small alternating current is applied to some of the electrodes [16, 3]. The resulting electrical potentials are measured from the rest of the electrodes, and the

process repeated for numerous different configurations of electrode patterns. This technique has a main disadvantage that the electrode sensors need to be attached at a regular intervals around a patient, which presents great difficulties in biomedical EIT where the position of the electrodes attached to the patient body can be changed continually due to the movement of the patient. This can certainly interfere the quality of the reconstructed image, because the tomography reconstruction algorithm requires an accurate knowledge of the sensor positions. But with MIT, these electrodes are replaced by coils, which do not touch the patient and can therefore eliminate the problem. Since MIT coil sensors are also sensitive to conductivity and do not need physical contact with the body during investigation, it has the following advantages over EIT:

- No more electrode positioning problem, as the movement of the patient body does not interfere the position of the sensor coils.
- No more problem with uncertain electrode contact impedance.
- No more inconvenience of attaching electrodes to patients.

Several research groups have successfully used MIT techniques in biomedical applications, as a replacement for EIT. The following applications have been suggested:

- General human body tissue conductivity imaging - a replacement of EIT [3].
- Imaging of brain conductivity - the advantage of MIT is that the magnetic field can easily penetrate through the skull, whereas for EIT, skull acts as a resistive barrier [17].
- The inductive measurement of wound conductivity - performing impedance measurements of a wound from electrodes is very difficult as the surrounding skin is often uneven and in poor condition [18].

1.4 Aims and Objectives of the Dissertation

The objective of this dissertation is to construct a data acquisition system for MIT, in order to demonstrate the feasibility of MIT as a method to detect both metallic objects and saline solution (which is equivalent to some high water content tissue, such as muscle), which can therefore be used for both industrial and biomedical applications. MIT also has a potential to be applied in pipe-flow measurement applications, if the flowing content within the pipe has a similar conductivity to saline solution or the liquid itself contain magnetic or metallic material [19, 20]. The captured data must correspond to the predicted MIT theory, which is described in Chapter 2. The other objective is to make recommendations for further work in terms of improving the electronic system.

The development of an algorithm for conductivity cross section imaging is considered to be future work.

1.5 Plan of Development

The remainder of this dissertation is divided into the following sections:

- **Chapter 2** is a literature review, which briefly describes the MIT theory and lists a number of existing MIT systems in both industrial and biomedical applications, which can aid our system design. A complete system design layout for our MIT system is also concluded in this chapter.
- **Chapter 3** investigates the coil structural design, and several type of coils are investigated to assess pros and cons.
- **Chapter 4** introduces several signal demodulation methods for MIT systems. The selection of a suitable integrated circuit (IC) for demodulation is also discussed in this chapter.
- **Chapter 5** discusses the post-demodulation signal conditioning stage in our design; the circuit design for a low pass filter and a level shifter can be found in this chapter.
- **Chapter 6** deals with the digital control signal generation and the data acquisition hardware.
- **Chapter 7** presents and discusses the captured result under different conditions for the designed system.
- **Chapter 8** discusses the general image reconstruction algorithms, and both the forward and the inverse model for MIT are discussed here.
- **Chapter 9** draws conclusions based on the results obtained and makes recommendations for future work.

Chapter 2

Literature Review

This chapter will firstly illustrate the basic mathematical theory of MIT. Then, it will report on existing industrial and biomedical MIT before summarising the existing MIT hardware, which can help us with our system design at the end of this chapter.

2.1 Overview of MIT Systems

Because MIT is a non-contact modality, it is a suitable non-intrusive and non-hazardous imaging system. A typical MIT system is illustrated in Figure 2.1, which consists of the following [3]:

- an array of evenly spaced coils that are arranged around the measuring object,
- a custom data acquisition electronic system, and
- a computer for image reconstruction.

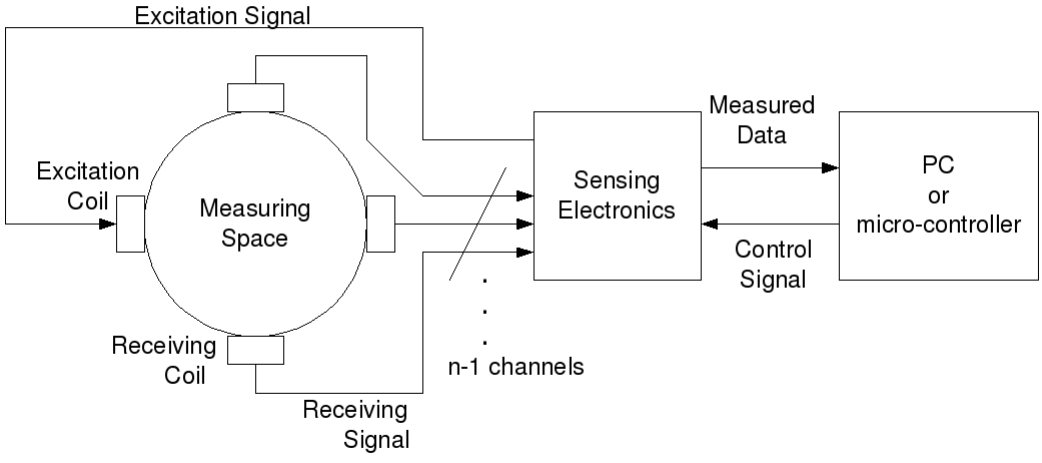

Figure 2.1: MIT system block diagram.

A brief description on MIT operation is given in this section, whereafter several existing MIT systems are discussed.

2.1.1 Mutual Inductance

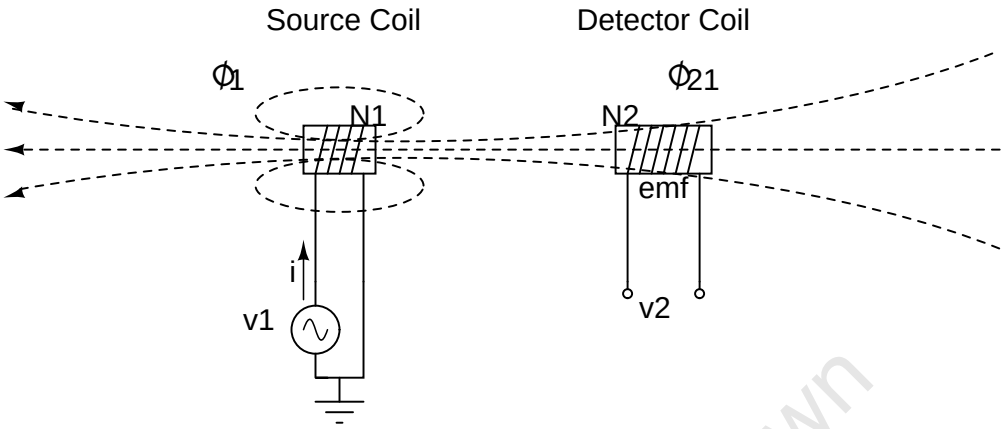

Figure 2.2: Mutual flux linkages between two coils.

Consider two coils that are placed co-axially, with the number of turns N_1 and N_2 respectively, as illustrated in Figure 2.2. The current i in the source coil establishes a flux Φ that links to the detector coil, which induces an emf in the detector coil. The induced emf in the detector coil is [21, 22]:

$$emf = N_2 \frac{d\Phi_{21}}{dt} \tag{2.1}$$

with a polarity that is always opposed to the change of the magnetic field produced in it by the source coil. If v_2 is the open-circuit voltage across the detector coil, then

$$v_2 = N_2 \frac{d\Phi_{21}}{dt} \tag{2.2}$$

Since $\Phi_{21} \propto i$, we can define a constant called the 'mutual inductance' L_{21}, then Equation 2.2 becomes

$$v_2 = L_{21} \frac{di}{dt} \tag{2.3}$$

then

$$L_{21} = N_2 \frac{d\Phi_{21}}{di} \tag{2.4}$$

L_{21} is the mutual inductance of the detector coil due to the flux generated by the source coil. The mutual inductance between two coils is therefore defined as the total flux linking one coil per unit change in current in the other coil.

The mutual inductance theory briefly shows the phenomenon of the inductance coupling between two coils, i.e. it explains how a coil acts as an inductance sensor, which can pick up the signal from the transmitting coil. The more sensor coils are involved, the more complicated the system's mathematical model is. The next section will describe the

mathematical model of a two channel MIT system, with an object placed between the coils.

2.1.2 Principles of MIT

A simple two channels MIT system is used in [23] to illustrate the basic theory for MIT:

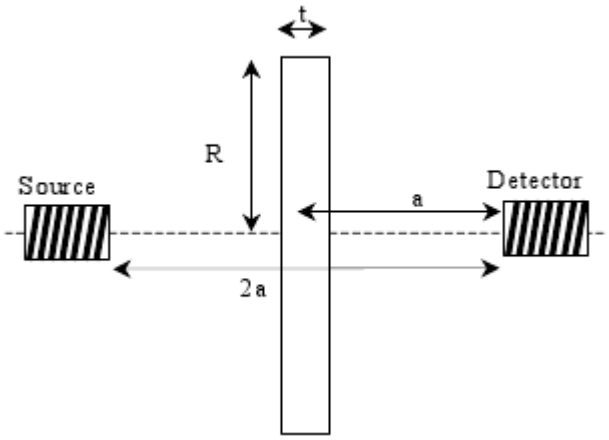

Figure 2.3: Magnetic field at a thin disk due to a small excitation coil (illustration from [24]).

Consider two coils, which are positioned co-axially and spaced apart by a distance $2a$. A sinusoidal signal, with angular frequency ω, is injected into one coil, because of the mutual magnetic coupling, the other coil will pick up a magnetic field signal B as well. Let a circular disk of dielectric of radius R, thickness t, conductivity σ, and relative permittivity ε_r be positioned co-axially and at the center between two coils, as shown in Figure 2.3. The eddy current induced in the disk causes a magnetic field perturbation, ΔB, in B, where B is the primary magnetic field that is picked up by the detector coil. One can consider B as a phasor representation of a sinusoidal magnetic field, which contains a magnitude and a phase (phase relative to the driving current) components, as shown in Figure 2.4. If the skin depth of the electromagnetic fields in the dielectric is large compared with t (i.e. the interaction is weak), it can be shown that [25]:

$$\frac{\Delta B}{B} = \frac{a^3 t}{2}\left\{\chi_m \frac{R^2(8a^2-R^2)}{(a^2+R^2)^4} + (\omega\varepsilon_0\varepsilon_r - j\sigma)\omega\mu_0\left[\frac{1}{a^2} - \frac{a^2+2R^2}{(a^2+R^2)^2}\right]\right\} \tag{2.5}$$

where ε_0 and μ_0 are the permittivity and permeability of the free space respectively, χ_m is the magnetic susceptibility of the material, which can be equated to $\mu_r - 1$. A detailed mathematical explanation of Equation 2.5 can be found in Appendix A. It should be noted from Equation 2.5, that the ΔB component caused by the induced eddy current is proportional to the excitation frequency. Furthermore, the imaginary part of the equation, $\mathrm{Im}(\Delta B/B)$ is theoretically only a function of the tissue's conductivity. The real part, $\mathrm{Re}(\Delta B/B)$, is a function of the object's permeability and permittivity.

In biological applications, ΔB is much smaller in magnitude than B and is normally dominated by the conductivity term, i.e. $|\Delta B/B| \propto \sigma$, Thus, the phase shift is normally the data that is required for image reconstruction. However, for a metallic object, where the conductivity is high and the permittivity is relatively small, the skin-depth is much smaller than the thickness of the sample and the behavior of $\Delta B/B$ is different to the proportionality equation: $|\Delta B/B| \propto \sigma$; its value is much larger than for the same volume of biological tissue, and it does not only contain a negative imaginary part but also a negative real part, which decreases the amplitude of the receiving MIT signal.

An explanation of the different $\Delta B/B$ behaviors between biological objects and metallic objects, as mentioned above, is to consider the path's impedance between the driving coil and the receiving coil. The path's impedance seen by circulating eddy currents is the sum of the path's resistance and the path's reactance, i.e. $R + jX$. The driving flux will induce a net voltage around a loop, which is 90° out of phase with the driving flux. If R dominates, i.e. the low conductivity case, the current will then be in phase with the voltage, and hence the current induced flux will lead the driving flux by 90°. Thus the Q component will be affect. On the other hand, if X dominates, as in the case with a highly conductive metal, the current lags the induced voltage by 90°, and hence the eddy current induced flux is in phase with the driving flux. The real component will then be affected.

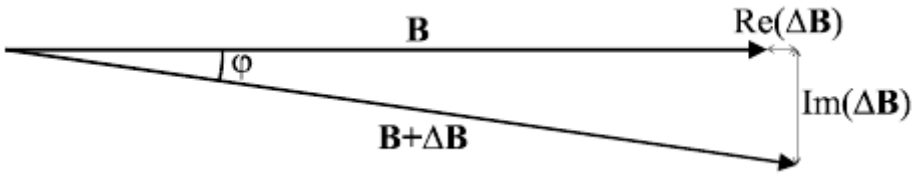

Figure 2.4: Phaser diagram representing the primary (B) and secondary (ΔB) magnetic fields detected in a biomedical MIT system (illustration from [5]).

One of the difficulties in MIT is that the signal induced by the eddy current ΔB is much smaller than the primary background signal B, especially in biomedical applications (in the case where $\mathrm{Im}(\Delta B/B)$ is generally $\approx$1 % [5]).

Figure 2.4 shows the phasor diagram of the primary (B) and secondary (ΔB) signal, ($B + \Delta B$) is the detected signal from the coil without subtracting any background signal. In order to increase the system's sensitivity, it may be a good idea to suppress the primary field signal B at the front-end before demodulating the signal. Several MIT systems have implemented this technique, in various ways, which will be described later.

2.1.3 Existing Industrial MIT Systems

As shown, MIT systems have been employed in industry mainly for metal detection, and to identify ferrite materials. It has been reported in [5], for ferromagnetic materials, that the ΔB is in-phase with the primary signal (i.e. ΔB is real and positive) and for highly

conductive objects, that the ΔB contained a negative real component and a negative imaginary component. This means that phase-sensitive detection was necessary in order to distinguish between these two materials. For industrial applications, ΔB could be as high as 25 % of the magnitude of B [5], much more significant than in biomedical applications.

Some early MIT systems for industrial used had been summarised in [5] and [10]. These papers described the theoretical background of the MIT technique, the coil design system electronics and several image reconstruction techniques. This section will describe some later MIT systems, which were not covered in those summary papers.

Yu et al. discussed a MIT system in [15], which employs a parallel excitation magnetic field created by two pairs of coils. Twenty-four detection coils were arranged in a circle around the imaging space. The coils were situated within two screens: an inner-ferrite magnetic screen and an outer-conducting electrostatic screen. Screening of the coils was essential for the MIT system, as it would reduce electromagnetic interference from the outside environment, which would increase the sensitivity to the measuring object inside. More importantly, the electrostatic interference between the excitation coil and the receiving coil could be minimised, as this interference could sometimes have a serious effect on the measurement. The system was operated at a frequency of 156 kHz. A correlation algorithm was used for image reconstruction, and the image of a metallic bar was demonstrated in the report. The maximum image capture rate of this system is 240 frames/sec. The cross sectional structure of the system and its produced image are shown in Figure 2.5:

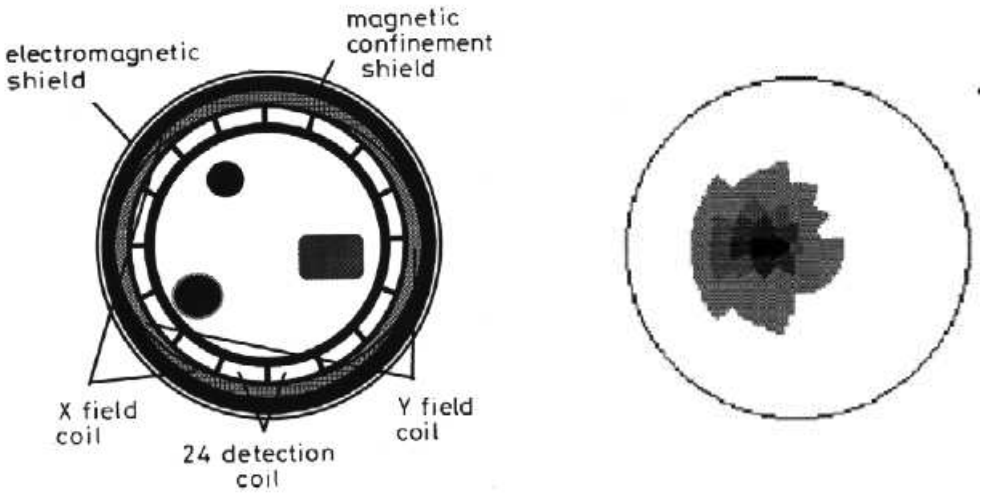

(A) (B)

Figure 2.5: (A) Cross-sectional structure of Yu's MIT system. (B) Reconstruction image where a bar is placed within the measuring space (illustration from [15]).

G. M. Lyon et al. published a paper [26] to describe a MIT system's sensor and instrumentation developed at UMIST and University of Lancaster, which combines the advanced features of two existing systems [10]:

1. The INSEC Multi-pole MIT scanner, which uses point source solenoid excitation.

2. The UMIST parallel field EMT system, which uses a uniform parallel excitation field.

The system contained 16 coils, which were situated in a circular form around the imaging space; the coils could be switched to become either a transmitter or a receiver. During the developing stage, the coil size, shape and positioning of the coils were carefully designed to reduce inter-coil coupling and environmental interference. The operating frequency for the system was chosen to be 2 MHz. The background signal subtraction stage was implemented in the electronic stage. A parallel in-phase and quadrature (I/Q) demodulation technique was used to compute the amplitude and phase angle of the receiving signals. The reference signal was synthesised by a second identical excitation control module. This paper, however, only described the data acquisition system, and no image reconstruction method was mentioned, Figure 2.6 shows the cross-sectional structure of the MIT system published in [26].

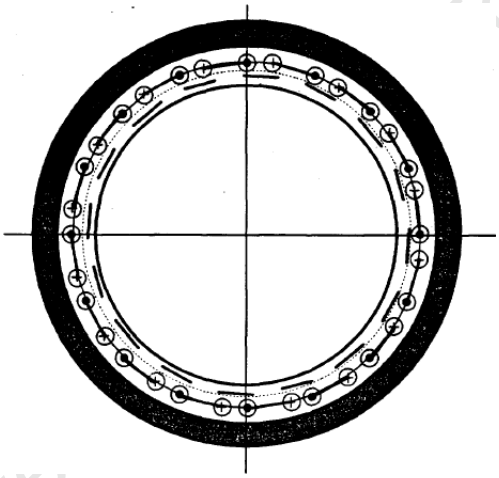

Figure 2.6: Cross-sectional structure of Lyon et al.'s MIT system (illustration from [26]).

In paper [27], X. Ma et al. proposed a MIT system operating at 5 kHz. The system was developed for the metal production industry - detecting the extent of solidification of molten metal flowing in a pipeline. The system's operating frequency was chosen to be very low so that the temperature durable material would not disturb the measurement. Eight 50 turn coils were used in the system, and these were evenly spaced along the circumference of the circular object space. The in-phase and quadrature demodulation technique was also implemented in this system. The image reconstruction algorithm of the system was further discussed in [28]. An iterative algorithm based on the simultaneous iterative reconstruction technique (SIRT) and two non-integrative algorithms using Tikhonov regularization and singular value decomposition (SVD), were selected for the system. Detailed descriptions of these algorithms can be found in [29]. Various reconstruction images in different conditions were shown in [28]. Since the operating frequency is relatively low compared

to the other systems (5 kHz excitation signal), the highest data rate that the system can achieve is only 10 frames/sec. Figure 2.7 and 8.1.2 show X. Ma et al.'s MIT system and its reconstructed images.

Figure 2.7: Photography of Ma et al.'s MIT system and the physical sensor structure (images from [27]).

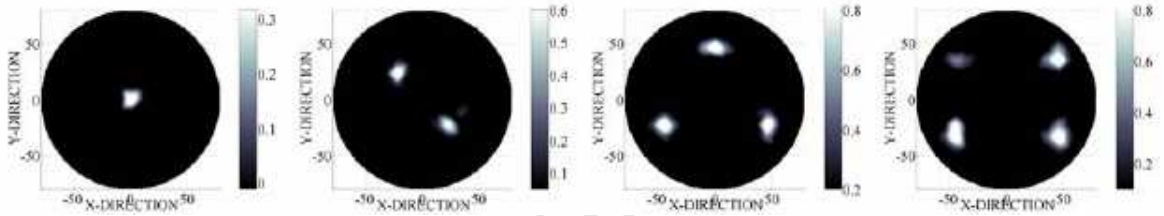

Figure 2.8: Reconstruction image where different numbers of metal bars are placed within the measuring space (images from [27]).

An overview of the industrial MIT technology is also given in [30], including coil design and electronics architecture. In an accompanying article, [31] presents a review of image reconstruction.

2.1.4 Existing Biomedical MIT Systems

Biomedical MIT was originally investigated by Al-Zeibak and Saunders [32] in the late 1980's. MIT is a non-contact technique for electrical impedance visulisation and is currently being investigated by a number of groups worldwide: H. Griffiths et al. from the University Hospital of Wales in UK [23]; S. Watson et al. from the University of Glamorgan in UK [33]; D. Goss et al. from the University of Lancaster in UK [34, 24]; H. Scharfetter et al. from the Graz University of Technology in Austria [35, 25] and A. V. Korjenevsky et al. from the Russian Academy of Sciences in Russia [6, 11, 36].

Biomedical MIT is still at a fairly early stage of development. The development of MIT for biomedical applications presents great difficulties because the conductivities of biological tissues are substantially smaller than those of metals (less than 1 S/m) and they have no appreciable permeability compare to free space; this means that biological tissue

can only produce a very weak, but nevertheless detectable response to the applied magnetic field, as discussed in Section 2.1.2. In order to increase the signal strength and the system's sensitivity, the excitation frequency needs to be much higher than in an industrial system. Therefore a medical MIT system typically operates in the range of 1-20 MHz. Increasing the operating frequency also increase the difficulties in electronic design. A proper coil screening arrangement and a fairly stable data acquisition system needs to be carefully designed in order to avoid inter-coil coupling and background interference. These difficulties are also experienced in industrial applications that involve the imaging of water ionization [5].

Some early biomedical MIT systems have also been summarised in [5] and [10]. This section will describe some newly developed biomedical MIT systems, which were not covered in those summary papers.

Korjenevsky et al. presented a practical system in [11, 37]. It is also a multi-coils system as described in [27]. Sixteen 5 cm diameter cylindrical formers were attached around a 35 cm diameter circular container, and both excitation and detection coils were reeled up in pairs on a former and placed along the circular container in a fixed interval. The inductors consisted of two turns of wire and had an inductance of 0.7 µH each. The system was housed within an electromagnetic screen. The carrier frequency of the system was 20 MHz but it was down-converted to 20 kHz to ease the signal processing and electronic design. The direct phase measurement technique was employed in the system. The coils were not individually screened but used differential detection to minimise inter-coil coupling interference. The image reconstruction was done by the filtered back-projection method, and an image of a tank of tissue-equivalent saline solution was clearly shown in the paper. However, the image was referenced to a homogeneous saline solution rather than to empty space. Figure 2.9 shows the front-end structure of the MIT system and its reconstructed images.

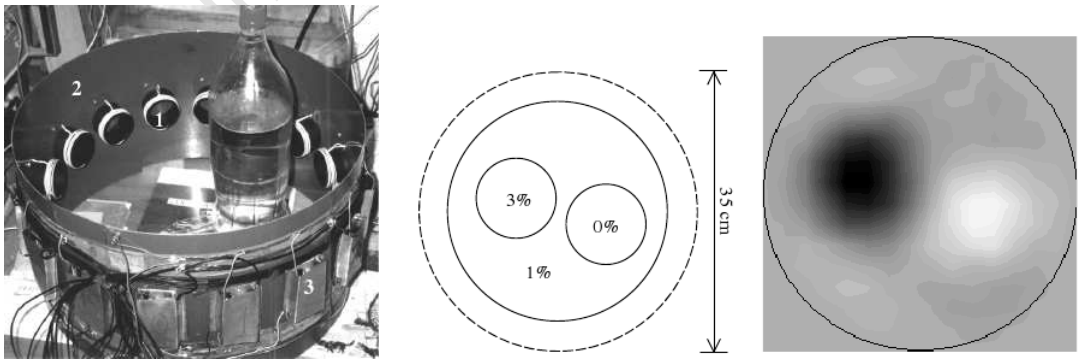

(A) (B)

Figure 2.9: (A) Front-end structure of Korjenevsky et al.'s MIT system. (B) Reconstructed image where several saline water bottles with different concentrations were placed within the measuring space (images from [11]).

S. Watson et al. proposed a MIT system in [33]. Their system consisted of a cylindrical aluminum screen (35 cm diameter, 25 cm height) and 16 perspex coil formers of 5 cm

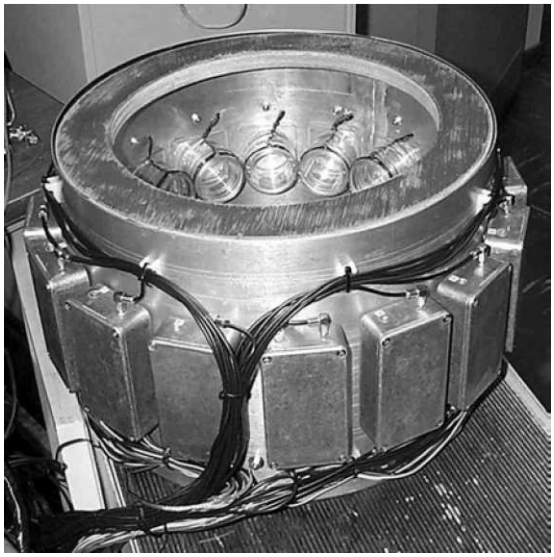

Figure 2.10: Front-end structure of Watson et al.'s MIT system (image from [33]).

diameter, which were attached to the inside of the screen. A 2 turn balanced transmitting coil and a 2 turn balanced receiving coils were wrapped on each coil former. An OPA3682 op-amp was used at the front-end of the receiver circuits, which allowed conversion of the receiving signal from balanced to single-ended while also rejecting common mode capacitive coupling. The electronic circuits for each receiver were housed inside an enclosure, which was attached to the outside of the screen. The system architecture was similar to the system described in [11]. The operating frequency of the system was 10 MHz, which would be heterodyne down-converted to 10 kHz for digital demodulation. The paper did not mention any image reconstruction algorithm, as it focused on two different signal measuring algorithms: direct phase measurement and vector voltmeter measurement. With the vector voltmeter technique, the paper claimed that a precision of 50 m$^\circ$ could be achieved. The front-end structure of the MIT system is shown in Figure 2.10.

D. Goss et al. proposed a MIT system in [34]. The system was developed to determine human body composition. The sensor array contained 16 coils, 8 excitation and 8 detection. The coils were positioned around a circular container, which provided an object space diameter of 750 mm. The coils were printed on 140 mm^2 printed circuit board (PCB), and each coil was covered by two PCB electrostatic screenings. The coil array was further screened from the external interference by an 1 mm thick aluminum sheet. The system operated at a frequency of 1 MHz. The MIT system used a ZENIX data acquisition system (manufactured by IXTREM, Chalon sur Saone, France), which used a analog to digital converter (ADC) to sample the induced signal directly. Its background signal compensation was achieved with the software approach. The image of the object space was reconstructed using a 'projected Landweber scheme', which was discussed in [38]. The pictures of the MIT system layout and its reconstructed images are shown in Figure 2.11.

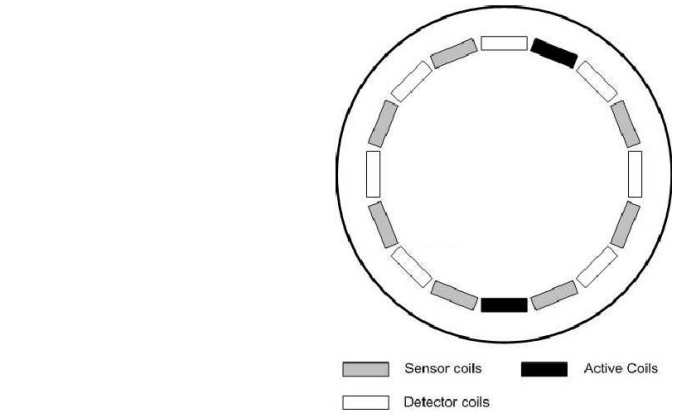

(A)

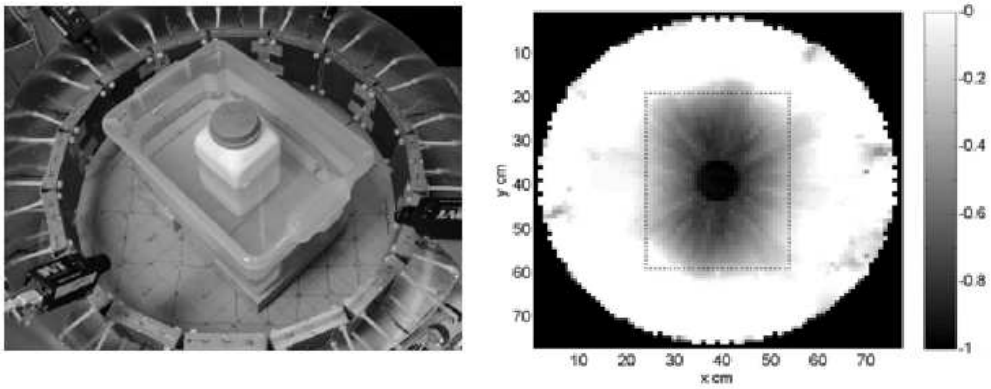

(B)

Figure 2.11: (A) Cross-sectional structure of Goss's MIT system. (B) Reconstruction image where a water tank was placed within the measuring space (images from [38]).

H. Scharfetter et al. proposed a rotatable, two channel multi-frequency MIT system in [17] which operated from 20-370 kHz with a possibility of extending the range up to 1 MHz. For such a low operating frequency, $|\triangle B/B|$ could be as low as 10^{-7} [25]. To detect such a small signal, a combination of 'planar gradiometer sensor' (PGRAD) and a high resolution phase detector were used.

A gradiometer basically consists of two coils that are connected together but differentially (opposite winding directions), so when a PGRAD is inserted into such a field that both coils will sense the same magnetic field (in the MIT case, the primary signal), and thus the influence of the external field will be eliminated. Therefore, by using PGRAD as the front-end sensors, the demands on the primary signal cancellation electronics will not be as great as in the normal coil system. However, the use of PGRAD has some disadvantages: firstly, the symmetrical alignment between excitation and detection PGRAD becomes extremely important, as it can significantly affect the performance of primary signal cancellation. Secondly, in reality, two comparatively high voltages in the two coils of a PGRAD can never be subtracted perfectly, thus leaving a residual voltage which is prone to drift. Thirdly, for multiple excitation coils, a given PGRAD can only cancel the primary signal for one excitation coil position, which makes it unsuitable for a multi-channel system design.

H. Scharfetter et al.'s system front-end contained a 47.5 mm radius, 17 turns copper solenoid which had a 35 μH inductance , a 7+7 turns PCB PGRAD with 5+5 μH inductance and a 7 turns, 5 μH reference PCB coil. The system's schematic is shown in Figure 2.12:

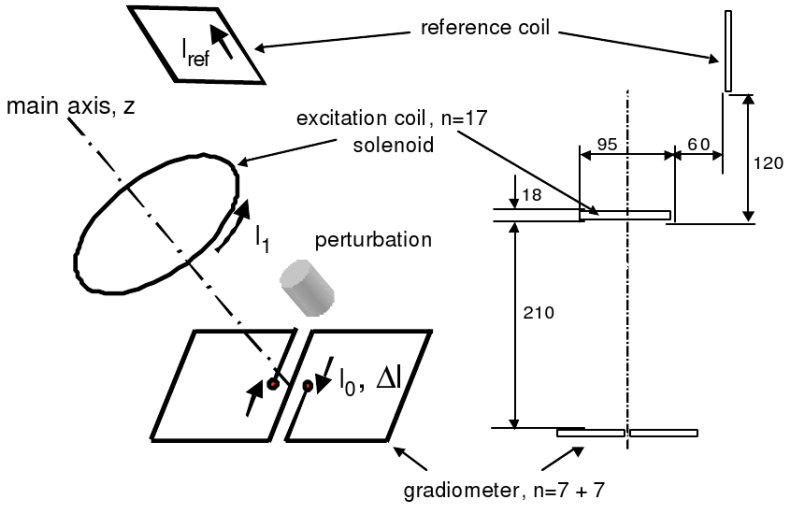

Figure 2.12: Schematic of H. Scharfetter et al.'s two channel MIT system (illustration from [17]).

In a recent publication by Scharfetter [39], a new type of gradiometer was developed, which eliminated the problems that were mentioned previously. This new type of sensor was called a 'zero-flow gradiometer (ZFGRAD),' which is a combination of PGRAD and a 'zero flux coil (ZFC)'. ZFC is a receiving coil that is orientated 90 degrees with respect to the excitation coil such that the net magnetic flow is zero within the coil. Therefore the imperfect primary signal cancellation problem could be solved by using ZFGRAD. It was also stated that ZFGRAD had a similar spatial sensitivity as the old PGRAD system, but a higher rejection on far sources perturbations than normal PGRAD and ZFC. The perturbation to signal ratio (PSR) was more than 12 times lower than the others. The MIT system demonstrated in this paper had two arrays of eight excitation coils and eight ZFGRAD respectively. A single-step Gauss Newton reconstruction algorithm was used for generating images. Figure 2.13 and 8.1.2 show the schematic of the ZFGRAD system and its reconstructed images. The basic schematic of a multi-pole PGRAD system and a multi-pole ZFC could be found in [39] as well.

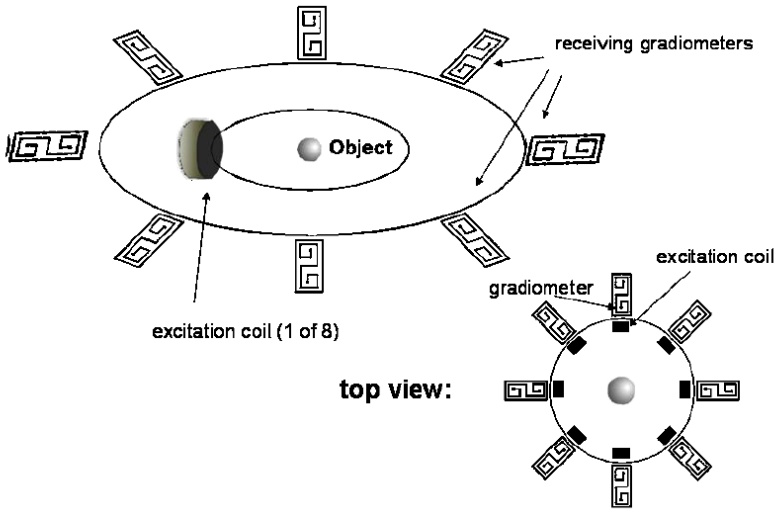

Figure 2.13: Schematic of the 8 channel ZFGRAD system (illustration from [39]).

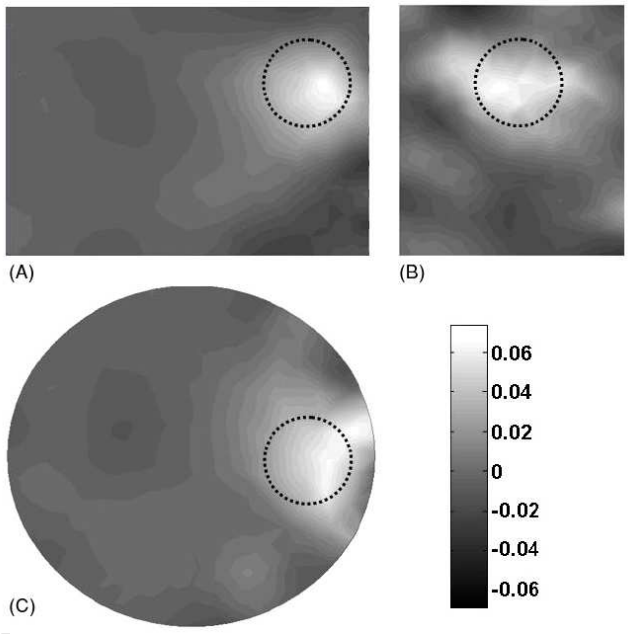

Figure 2.14: Result of 3D reconstructed images: (A) Top view, (B) Side view, (C) Front view. The dotted circle shows the position of the actual perturbation (images from [39]).

2.2 Summary of Existing MIT Systems

From our literature survey, a summary table can be constructed. Table 2.1 shows most of the existing MIT system in the world, with respect to the publishing year and the institution.

In general, MIT systems can be divided into two categories according to their applications: industrial use and biomedical use. Since the main detecting objects for each type of system differ hugely in conductivity and permeability, the design for each stage of such MIT hardware systems requires a different focus.

	Year	Research Group	Institution	Journal Paper
Industrial Application	1993	Z. Z. Yu et al.	Univ. of Manchester, UK Inst. of Sch. & Technol.	[40, 30]
	1995	R. A. Williams et al.	Univ. of Exeter, UK Camborne School of Mines	[3]
	1999	M. H. Pham et al.	The Univ. of Melbourne, Australia Dept. of Electrical and Electronic Eng.	[41, 42]
	1999	S. Ramli and A. J. Peyton	Inst. for Nuclear Tech. Research, Malaysia Engineering Unit	[43]
	2001	D. J. Sadler et al.	Univ. of Cincinnati, USA Dept. of Elec. and Comp. Eng.	[44]
	2005	X. Ma et al.	The Univ. of Manchester, UK Sch. of Electircal and Electronic Eng.	[27, 28] [45]
	2005	G. S. Park et al.	Pusan National Univ., Korea Dept. of Elec. and Comp. Eng.	[46]
Biomedical Application	1993	S. Al-Zeibak et al.	Swansea Univ., UK Dept. of Phys.	[32]
	1995	Z. Z. Yu et al.	The Univ. of Manchester, UK Process Tomography Unit	[47]
	1996	G. M. Lyon et al.	Lancaster Univ., UK Dept. of Eng.	[26]
	1999	H. Griffths	Univ. Hospital of Wales, UK Dept. of Med. Phys. and Clinical Eng.	[23]
	1999	A. V. Korjenersky et al.	Russian Academy of Sciences, Russia Inst. of Radio-Eng. and Electronics	[6, 11]
	1999	N. G. Gencer et al.	Middle East Tech. Univ., Turkey Dept of Electrical and Electronics Eng.	[48]
	2001	S. Watson et al.	Univ. of Glamorgan, UK School of Electronics	[49, 50] [33, 51]
	2001	H. Scharfetter et al.	Technical Univ. of Graz, Austria Inst. for Biomed. Eng.	[17, 39]
	2003	D. Goss et al.	Lancaster Univ., UK Dept. of Eng.	[34]

Table 2.1: Summary of Existing Tomography System.

2.2.1 Sensor Coil

Many type of coils were implemented in different MIT systems, such as air-core coils, PCB coils and gradiometers. Sensor coils that are used in industrial MIT systems generally have more turns (50 turns [27]) than the biomedical MIT system (2 turns [11, 37]). By decreasing the number of turns in a biomedical system, the impedance of the coil can be minimised and more current can flow through the coil, therefore generating a stronger flux into the measuring space, which aids improves the system's sensitivity.

In many MIT systems, the transmitting coil and the receiving coils are wound separately on the same former. This is done so the sensor coil that is next to the transmitting coil on the same former can be used to detect the primary signal. This receiving signal is going to be used for primary signal cancellation, which can improve the system performance.

2.2.2 Operating Frequency

As stated before, the operating frequency for biomedical MIT system tends to be much higher (in the MHz range) than that of most industrial systems (in the kHz range). The reason is that the perturbation signal produced by biomedical material has a magnitude that is several orders smaller than the signal produced by metallic objects, due to its relatively weak conductivity. Previous investigations have reported that a frequency that is less than 10 kHz is not feasible for biomedical MIT systems [23, 17].

Biological tissues have strong dispersion characteristics. Permittivity and conductivity are very dependent on frequency, therefore there is no absolute conductivity for them; nevertheless it is possible to find out their conductivity with a fixed excitation signal frequency. Figure 2.15 shows the conductivity of different tissues from 1 kHz to 100 MHz.

From Figure 2.15, one can see that the conductivity of biological tissues start to increase significantly when the excitation frequency is beyond 1 MHz. The upper frequency limit for MIT is determined by the penetration depth of the electromagnetic field and the desired sounding depth. So far, the highest working frequency among the existing MIT systems is 20 MHz, which is reported by A. V. Korjenevsky et al. [11].

In general, a high excitation frequency is required in biomedical MIT systems in order to increase the signal strength and the system's sensitivity. It is very temping to work at the resonance frequency of the coil, as it can increase the system's sensitivity significantly. However, it has been suggested that working at a frequency that nears the resonance of the coil should be avoided, as the interaction between the coil at resonance might be very complicated [10].

2.2.3 Demodulation Techniques

According to the literature, there are two popular demodulation techniques that can extract the signal phase change from the receiving signals which contains the conductiv-

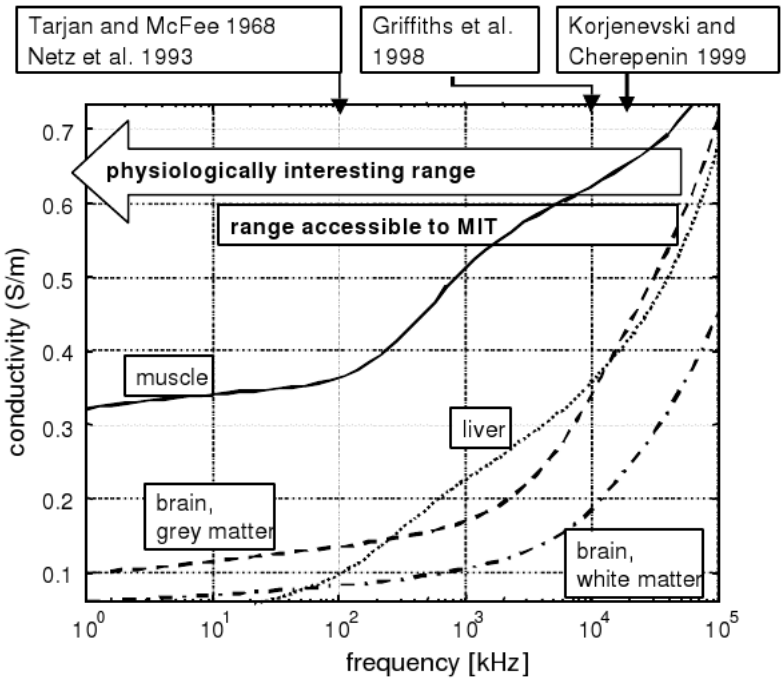

Figure 2.15: Conductivity measurement of biological tissue at various frequency (graph from [17]).

ity information within the measuring space: direct phase measurement and synchronous detection [33]. Both techniques can be implemented in industrial and biomedical MIT systems. A proper investigation of both techniques is done in Chapter 4.

2.2.4 Screening

Screening is essential for all MIT systems, as the electromagnetic interference from the outside environment can be reduced, and the capacitive coupling between the transmitting coil and the receiving coil can be minimised. All the MIT systems in the literature implemented the electrostatic screening in their design, albeit in different forms. The outer ferrite magnetic screening and metallic electrostatic screening were used to eliminate the outside electromagnetic interference. The sensor coils themselves could also be screened to prevent the direct coupling between coils.

The importance of screening the coil and the screening method are discussed in Chapter 3.

2.3 MIT System Architecture for the Prototype System

After investigating a number of existing MIT systems, a general structure of a complete MIT system was drafted. The driving frequency of our prototype MIT system was chosen to be in MHz range, because this high operating frequency approach made the project more challenging and the area of applications of the MIT system could be broadened as well (can be used in both industrial and biomedical applications). However, the exact

operating frequency must be decided based on the parameters of the coil sensor (selection of the coil, input impedance of the coil, resonance response of the coil...etc), which will be discussed in Chapter 3. This section here provides a brief overview of the system architecture and the design process of our MIT data acquisition system.

To construct a MIT data acquisition system, a general transceiver electronics circuit is needed, as it is used to supply the driving signal to the coil and also to amplify the receiving signal that is picked up from the sensor coils. Extra post processing circuitry is required to filter out the noise and to perform the level shifting of the demodulated output signals, in order to match the input range of the ADC. Thereafter, the ADC samples and stores the data on the PC and finally the PC implements the signal processing algorithm in order to retrieve the useful information from the received signal. A complete system block diagram is shown in Figure 2.16:

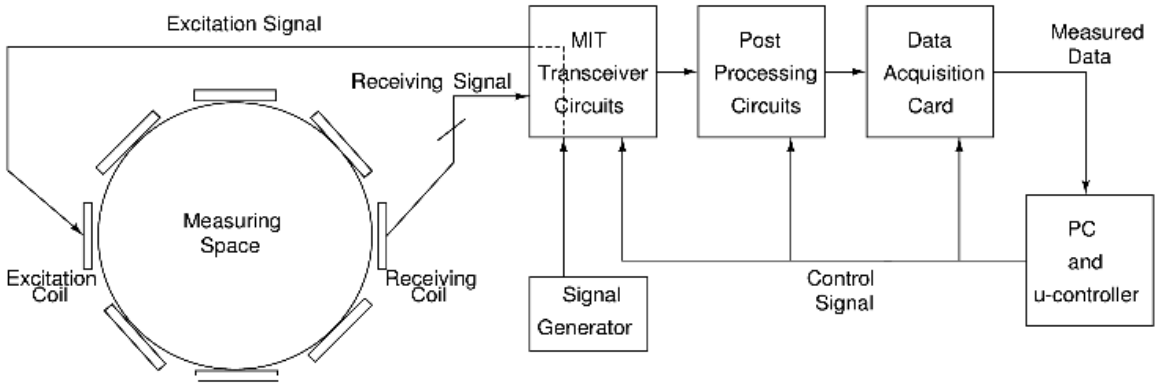

Figure 2.16: A complete MIT system block diagram.

For the prototype system, a perspex cylindrical tube with a 20 cm diameter was chosen, which is shown in Figure 2.17.

An Agilent 33250A signal generator was used as the main excitation signal source in our prototype system. It was chosen because of its signal flexibility, since the driving signal's frequency and amplitude have not been decided yet. Once those parameters are chosen, a direct digital synthesis (DDS) chip or a crystal can be implemented to reduce the power consumption and the system size. A picture of the signal generator is shown in Figure 2.18.

Figure 2.17: Perspex cylindrical tube with a 20 cm diameter

Figure 2.18: Agilent 33250A signal generator.

The design process can be divided into the following stages: coil design, signal demodulation, signal processing and data acquisition, which are discussed respectively in Chapters 3, 4, 5 and 6.

Chapter 3

Induction Coil Sensor Design

Induction coil sensors (also called search coils, pickup coils...etc) are one of the oldest and most well-known magnetic sensors. The operating principles of the coil sensor are generally known. The output signal, V, of a coil sensor is proportional to the rate of change of flux density, dB/dt. Its transfer function $V = f(B)$ can be determined from the fundamental Faraday induction law [22, 21]:

$$V = -L \cdot \frac{dI}{dt} = -N \cdot \frac{d\Phi}{dt} = -N \cdot A \cdot \frac{dB}{dt} = -\mu_0 \cdot N \cdot A \cdot \frac{dH}{dt} \tag{3.1}$$

where L is the inductance of the coil, and Φ is the magnetic flux passing through a coil with an area A and a number of turns N. It can be shown clearly that a high coil sensitivity can be obtained by using a large number of turns N and a large active area A.

Figure 3.1: A simple sensor of a magnetic field in the form of a coil (image from [52]).

Figure 3.1 shows a basic construction of a typical circular air-core coil sensor. For a coil that has a high length to radius ratio, its inductance can be determined by the following

equation [21]:

$$L = \frac{\pi \mu_0 \mu_r r^2 N^2}{l + 0.9R} \tag{3.2}$$

where N is the number of turns, r is the radius of the loop, μ_0 is permeability constant ($4\pi \times 10^{-7}$), μ_r is relative permeability (for the air-core coil sensor, μ_r is 1) and l is the side length of the coil.

As in-depth research was done to choose the suitable type of the coil sensors, this section will list the characteristics of four different types of coil sensors: air-core coils, ferromagnetic-core coils, planar coils and gradiometers.

3.1 Air-Core Coil

Air-core coils are the most common coils and they are widely used as induction coil sensors in many applications, due to their simplicity. The air-core coil is the easiest induction sensor that can be manufactured directly by a user. The method of coil manufacture is simple and the materials (winding wires) are also commonly available. Thus, almost everyone can construct simple, low cost, yet accurate coil sensors.

However, air-coil sensors have the following disadvantages:

- Low sensitivity, because of low relative permeability ($\mu_r = 1$) compared with the permeability of ferromagnetic material (μ_r is generally several orders larger than 1)
- high stray field radiation and pickup; In the literature, residual capacitive coupling between the coils has been identified as a serious factor that can affect the performance of a MIT system.

To increase the sensitivity, a ferromagnetic core sensor can be used, and in order to reduce the capacitive coupling, the coil can be enclosed in an electrostatic screen (this will be discussed later in this chapter).

3.2 Ferromagnetic-Core Coil

The relatively low sensitivity of an air-coil sensor can be partially overcome by adding a ferromagnetic core, which acts as a flux concentrator inside the coil. Modern soft magnetic materials have a relative permeability μ_r that is generally larger than 10^5, which results in a significant increase of the sensor's sensitivity. However, this enhancement is achieved with a trade off of one important advantage of air-core sensors: the linearity. For rigid air-core coils, $\mu_r = 1$, L is a function of coil's geometry and the number of turns, and independent of current (from Equation 3.2). But since μ_r for the ferromagnetic core changes with applied magnetic flux, the inductance of a coil becomes non-linear. Additional magnetic noise (e.g. Barkhausen noise [52]) also decreases the performance of the

sensor. Moreover, the ferromagnetic core will alter the distribution of the magnetic field, which needs to be considered carefully if a ferromagnetic-core coil is chosen to be the sensor.

3.3 PCB Planar Coil

PCB planar coils can be manufactured on printed circuit boards (PCB). This makes them easy to reproduce, geometrically flexible, accurate rigid construction and cost effective. Several PCB coils can be stacked together to increase the inductance. Figure 3.2 shows an example of a 7 turns PCB coil with 2.5 μH inductance and a PCB electrostatic screening.

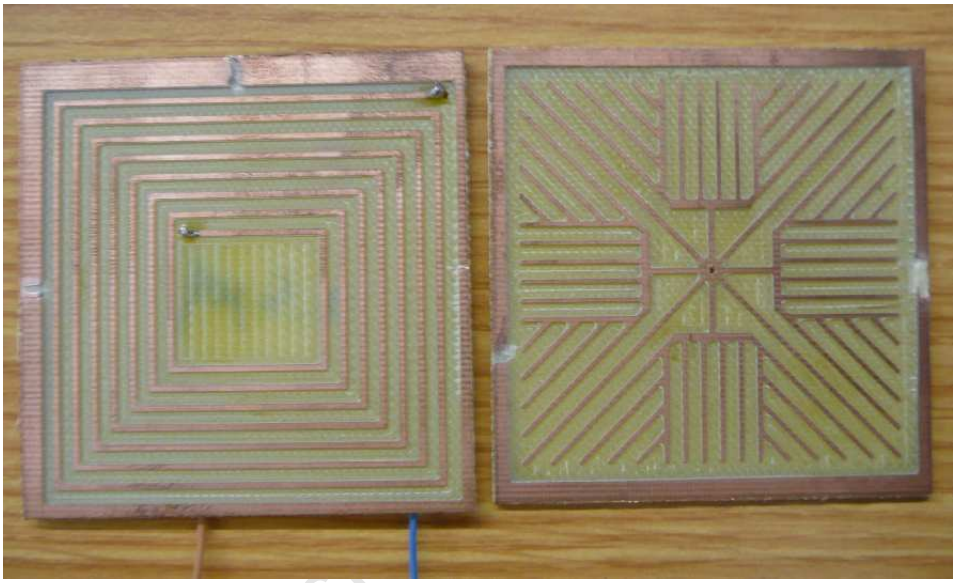

Figure 3.2: An example of a PCB planar coil and a PCB electrostatic screening.

The advantage of the PCB planar coil is that it is guaranteed that all the sensor coils are identical, which can reduce the 'amount of calibration' when processing the captured data. Also, the size of the coil can be very compact. Using PCBs also makes it it possible to integrate the front-end electronics with the coil, which can minimise the effect of the cable due to stray capacitance. An example of such a sensor with dimensions $400 \times 400 \mu m^2$ (7 turns) connected to an on-chip CMOS electronic circuit is presented in [44].

3.4 Gradiometer

The gradiometer sensors are commonly used in superconducting quantum interference device (SQUID) magnetometers to eliminate the influence of ambient fields in order to measure extremely small magnetic fields [52]. These sensors can also be used in other applications where ambient fields disturb measurements.

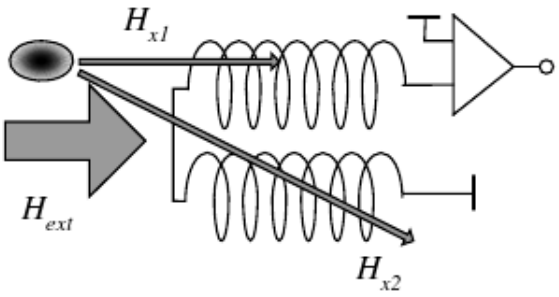

Figure 3.3: Operating principle of a gradiometer sensor (illustration from [52]).

The operating principle of the gradiometer sensor is shown in Figure 3.3. The external magnetic field is generated by a large and distant source (In the case of MIT, that is the primary background signal generated by the driving coil), so it is assumed that this field is uniform. Both coils are connected differentially. If two coil sensors are placed into such a field where both can sense the same magnetic field, the influence of the external field is eliminated. If at the same time there is a smaller source of magnetic field near one of the coils, then the coil placed nearer to such a source will sense a larger magnetic field signal than the other coil. This small difference can therefore be detected by the gradiometer sensor. In this way it is possible to detect a very small magnetic field signal that is buried in a relatively large background signal.

The advantage of using a gradiometer is that the primary fields can be canceled regardless of the stability of the electronics. Any fluctuations in the driving signal will affect the halves of the gradiometer and will not affect the cancellation.

The main disadvantage of using a gradiometer is that a precise mechanical and temperature stability is required, as it can significantly affect the performance of primary signal cancellation. To achieve ideal cancellation, both coils must receive the same magnetic flux when there is no signal source present in the ambient field. Meeting this condition for all sensor coils requires the axes of the gradiometer halves being parallel and symmetrical to the median plane, which requires an accurate mechanical design. More importantly, as has been reported in [5], a gradiometer is not suitable for a multi-channel MIT system, as for a multi-excitation coil system, a given gradiometer can only cancel the primary signal for one excitation coil position.

3.5 Screening

Screening is important in MIT system for two main reasons:

- To reduce the sensitivity of the sensor to outside magnetic signal sources;
- To reduce the capacitive coupling between the coils.

MIT system needs to measure very small changes in a magnetic signal. If a sensor coil is unscreened, the unwanted electric field coupling signal, which is usually much larger than the changes in a magnetic signal, can easily contaminate the desired magnetic receiving signal, which creates large errors in the measurements.

To screen the coils, the sensor coil can be enclosed within a grounded metallic container, which acts as a type of electrostatic screening, or a screened cable can be wound around the coil, with its outer screen being connected to the ground.

3.6 My Coil Design and Operating Frequency Selection

The process of designing the coil sensor began with the selection of the coil, which is to operate between 1 MHz and 20 MHz. A ferromagnetic-core coil was firstly eliminated from the consideration because of its non-linearity behavior, as discussed in Section 3.2. After taking the design simplicity and flexibility into consideration, a hand wound air-core sensor was chosen because of its linear performance and it is easy to adjust in prototyping (compared with PCB coils and gradiometers).

During the coil design process, it was found that there was large capacitive coupling between the transmitting and receiving coils. Furthermore, the unwanted capacitive signal can easily be greater than the true magnetic coupling signal.

To prevent this coupling, a single core screened cable (Communica, CAB1088 [1]) was chosen to wind around the coil. The cable was wound around a 5 cm diameter plastic former. The grounding was attached onto the screen at one end of the core, which forms the coil as 'shielded turns' (see Figure 3.4). The theoretical inductance for such a coil can be calculated from Equation 3.2, and the result in this case was approximately 2.02 μH. The actual inductance of the coil was measured with an Escort ELC 2260 LCR Meter, which gave us an inductance of 2.3 μH at 1 kHz. The theoretical value and the actual measured value were thus very similar at this frequency.

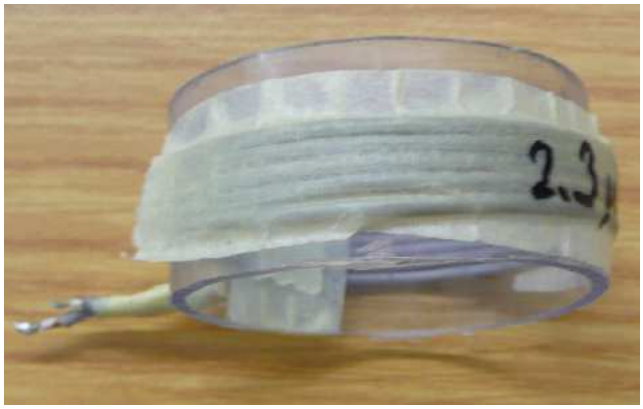

Figure 3.4: 5 turns screened coil with inductance = 2.3 μH.

[1]Audio Connector Cable - Inner core: ten 0.12 mm oxygen free copper (OFC) bare copper strands. Outer Screen : twenty-six 0.1 mm OFC copper spiral wrapped.

The coil needs to have a sufficient impedance in order to obtain a sensible range for the driving current. With our 5 cm diameter former and the Communica, CAB1088 screened cable, Table 3.1 could be made, one must note that this impedance calculation does not take into account the parasitic capacitance between the turns, which can affect the impedance as well.

Number of turns	Theoretical Inductance (μH)	Calculated Impedance at 10 MHz ($\|Z\| = \omega L\ \Omega$)
1	0.10	6.43
2	0.38	23.9
5	2.02	127
8	4.47	281
10	6.41	403
15	11.9	748

Table 3.1: Coil's inductance and impedance (at 10 MHz) with respect to different number of turns.

The inductance and the input impedance of the coil are important factors to determine the appropriate number of turns for our sensor coils. At a fixed frequency, the input impedance of the coil is proportional to the square of number of turns (i.e. $|Z| = \omega L \propto N^2$, if the parasitic capacitance is not taken into consideration). If the number of turns is too few, there will be not enough inductance and the driving current will be too high, due to its low impedance; if the number of turns is too many, the driving current will be too small to generate sufficient magnetic flux[2], hence the magnetic signal induced at the receiver will be weak. In our prototype system, a 10 turns coil is used.

To further reduce the effect of capacitive coupling, the coil can be constructed in a balanced way so that the large capacitive coupling signal is common mode rejected [49], with the aid of a differential amplifier. The operating principle and design of a balanced coil is shown in Figure 3.5. Again, its inductance (6.41 μH) can be calculated by using the same method as before, and the measured inductance at 1 kHz was 6.9 μH. In this set-up, the inductance differ by 0.49 μH.

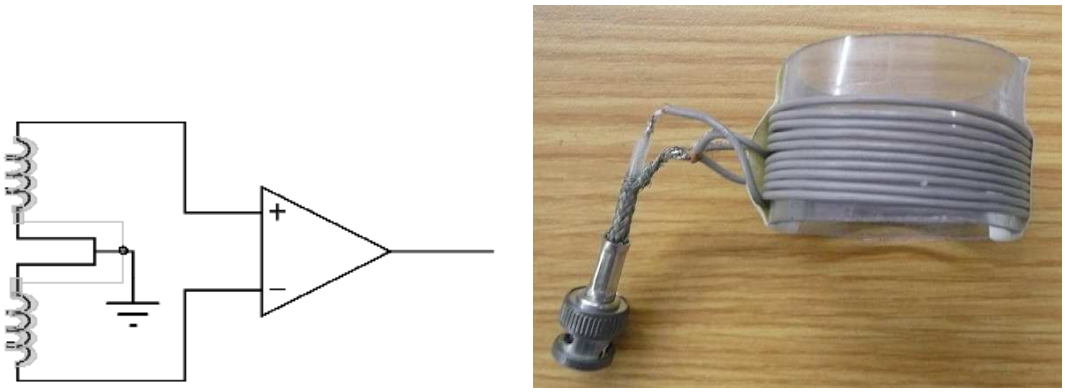

Figure 3.5: 5 turns + 5 turns balanced screened coil with inductance = 6.9 μH.

[2] $\phi \propto I_{drive} \times N \propto \frac{V}{Z}N \propto \frac{V}{N^2}N \propto \frac{V}{N} \propto \frac{1}{N}$, i.e. magnetic flux is proportional to $\frac{1}{N}$, where N is the number of turns of the coil.

To wind a coil by using a wire, extra capacitance will be introduced into a coil since each pair of turns effectively forms a parasitic capacitor. As some frequencies this capacitance will have the same magnitude of reactance as the inductance of the coil, and the coil will show a self-resonance. At the self-resonance frequency, the coil will have the highest input impedance [53].

The magnitude of the input impedance of the balanced coil was captured by an Agilent E5071B network analyser over the frequency range from 300 kHz to 13 MHz. The S_{11} parameter of the coil was first measured by the network analyser, where the S_{11} is the reflection coefficient, which can then be converted into the coil's input impedance by the network analyser's built-in function [3]. The input impedance plot of the coil is shown in Figure 3.6.

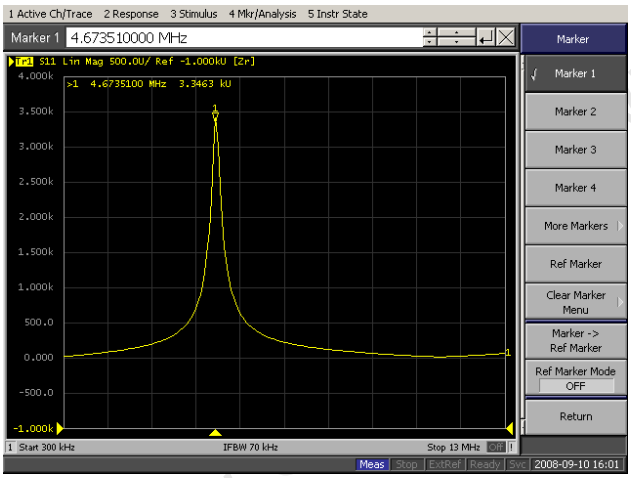

Figure 3.6: The magnitude of the input impedance of a 5 + 5 turns balanced coil.

It can be seen from Figure 3.6 that the balanced coil has an resonance of 4.67 MHz. It is suggested that the working frequency should not be at the resonance frequency, as working at resonance may present significant design difficulties under a multi-channel system because of complex interactions between the coils [10]. Also, the operating frequency of a biomedical MIT system for visualisation of the human body should be in the range of 10-20 MHz [6]. Therefore, we chose an operating frequency for our MIT system of 10 MHz; This frequency is away from the resonance frequency, which avoids the coils interaction problem.

Theoretically, one should operate the MIT system under the resonance frequency, as if the operating frequency is beyond the resonance, the coil will appear almost like a capacitor, and the current that flows into the driving coil will leads the applied voltage by 90 degrees. However, our operating frequency was still chosen to be 10 MHz, as it will be shown later in the result section (Figure 7.14 in Section 7.4) that, the system's ability to detect saline water when operating beyond the resonance frequency (10 MHz) and below the

[3] The reflection coefficient S_{11} can be used to calculate the magnitude of Z by the equation below, where Z is the impedance toward the load, and Z_0 is the impedance toward the source, which is generally 50 Ω: $Z = Z_0 \frac{1+S_{11}}{1-S_{11}}$

resonance frequency (3 MHz) are almost the same. Operating at higher frequency also increase the receiving signal strength, which means that less gain can be applied to the receiving signal.

3.7 Electronic Circuits Connected to the Coil Sensors

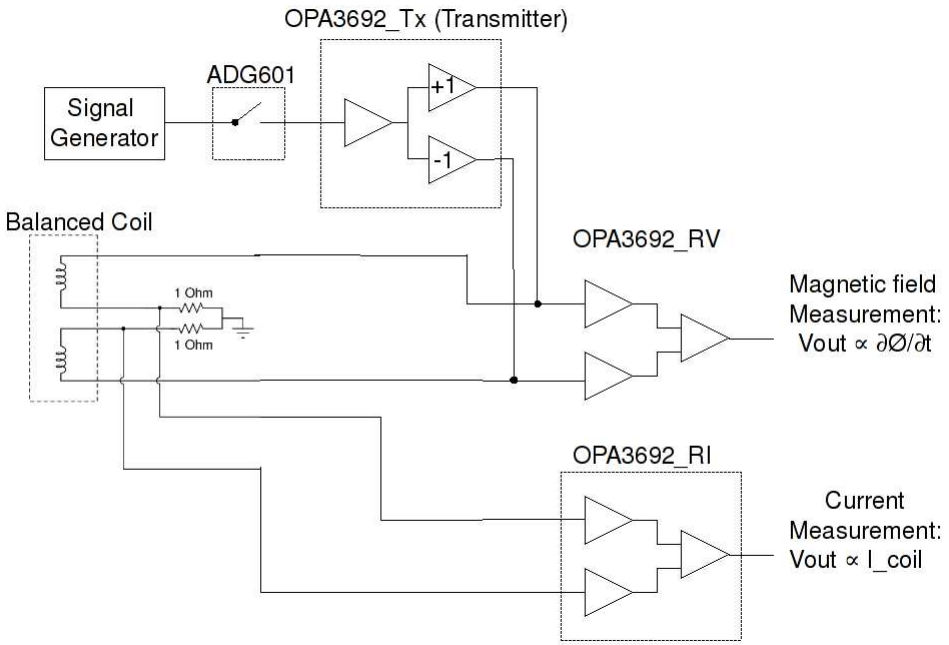

Figure 3.7: MIT transceiver circuit with a balanced coil.

Figure 3.7 shows a simplified block diagram of the electronic circuit that is connected to the balanced coil. It was decided to use the same coil for transmitting and receiving the signal, because this approach makes the prototype system design easier, and also, the primary field cancellation method will not be used in our design, therefore separating the transmitting and the receiving coil is no longer necessary.

The ADG601 is a monolithic, CMOS single-pole single-throw (SPST) switch with a 'on' resistance of typically less than 2.5 Ω and -32 dB isolation at 10 MHz. The OPA3692 is a triple, wide-band, fixed gain (+1, +2 or -1) video buffer amplifier with disable function. Its input impedance is typically 100 kΩ ||2 pF, however, when the OPA3692 is disabled, both its input and output can be viewed as a high impedance state of 1 MΩ in parallel with 2 pF, which offers a -68 dB isolation at 10 MHz. With different pin connections, the OPA3692 can be converted into a differential amplifier or an ordinary buffer.

3.7.1 Transmitter

A 4 Vp-p 10 MHz signal source for the transmitter was generated by an Agilent signal generator (Agilent 33250A). The OPA3692 was set up as a balanced driver for the transmitter coil. The OPA3692 was chosen because of its high bandwidth of 225 MHz and

its high output current, specified as 190 mA maximum. The OPA3692 also features a disable function, which can place the inputs and outputs into a high impedance state of 1 MΩ in parallel with 2 pF. By applying a logic low to the disable pin, the OPA3692 can be disabled, which allows the transmitter coil to be isolated when not in use.

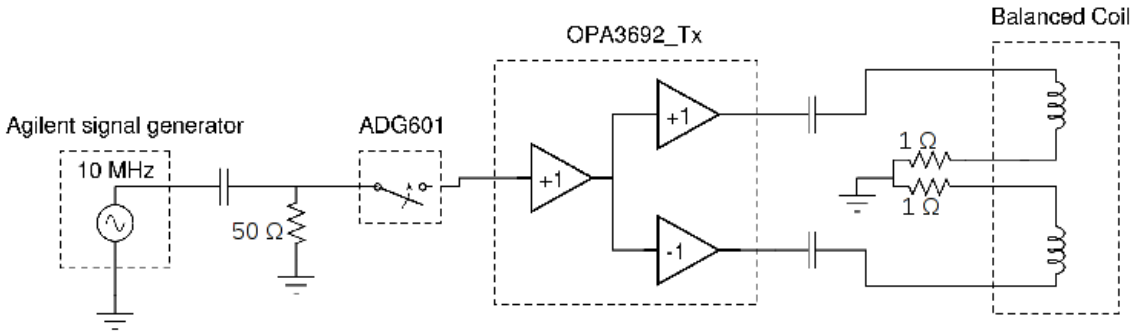

Figure 3.8: Transmitting circuit.

An extra ADG601 was added between the signal source and the OPA3692, to make sure that the relatively strong reference signal coming from signal generator did not leak through the OPA3692_Tx, which could have interfered with the output result. Complete isolation between the coil and the signal source was required when the coil was used as a receiver. Figure 3.8 shows the simplified schematic of the driving circuit.

3.7.2 Receiver

An OPA3692 (OPA3692_RV) was used at the receiver front-end, and it was configured as a differential amplifier, which allows the received voltage signal to be converted from balanced to unbalanced while rejecting some of the capacitive pickup, which was expected to be common mode. Two extra 1 Ω resistors were placed between the centre tap and the ground, which allowed a current measurement on the coil by another OPA3692 (OPA3692_RI) when the coil was in the transmitting mode. By including the current measurement, the input impedance of the coil itself could be measured, which might be helpful for improving the image resolution, as the number of independent measurement is increased. Different reconstruction algorithms may also be used for our data sets, since now both the driving voltage and current are known.

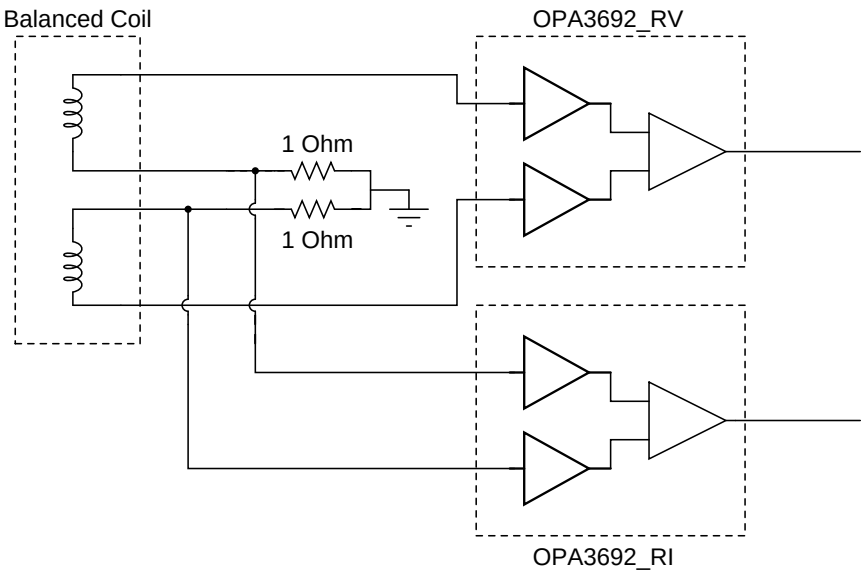

Figure 3.9: Receiver circuit.

As illustrated in Figure 3.8 and 3.9, we used three OPA3692 amplifier ICs in our design, which are labeled OPA3692_TX, OPA3692_RV and OPA3692_RI in the schematic diagrams. The OPA3692_TX was used to buffer the driving signal, the OPA3692_RV and the OPA3692_RI were used not only to buffer respectively the receiving voltage signal and the current measurement signal, but they also act as instrumentation amplifiers, which convert the balanced (differential) signal into unbalanced (single-ended) signal. When the coil was in the transmitting mode, the ADG601, the OPA3692_TX and the OPA3692_RI were in active mode and the OPA3692_RV was disabled. When the coil was in the receiving mode, the OPA3692_RV was activated, and the ADG601, the OPA3692_TX and the OPA3692_RI were disabled.

The logic switching between these buffers and the analog switch is discussed further in Chapter 6.

Chapter 4

Signal Demodulation

This chapter will discuss the demodulation methods of the MIT system. The term demodulation refers to the process of extracting the information from a carrier signal (i.e. in our case, it will be the amplitude and phase change relative to the driving signal).

In the MIT system, the phase of the receiving signal contains information about the conductivity of the tissue in the measuring space. The precision of the phase measurement directly affects the quality of the image. In the literature on MIT systems, two signal demodulation techniques have been used [33]:

- Direct phase measurement and [49, 11]
- Synchronous detection (this is also called In-phase and Quadrature (I/Q) demodulation) [27].

There are several methods to accomplish direct phase measurement. To perform direct phase measurement, the receiving signal (normally in the MHz range) generally needs to be down-converted into a lower frequency signal (in the kHz range) to ease the hardware electronic design. For the method published in [33], the received signal and a reference signal are taken directly from the transmitter coil, are amplified, limited to obtain two square wave signal which are then fed into a 74HC86 Exclusive OR Gate. The duty cycle of the periodic waveform at the output of the XOR Gate is directly proportional to the phase difference between the two signals, as shown in Figure 4.1. The phase difference between the down-converted receiving and driving signals can also be digitally measured by means of comparators and timers that are built into a micro-controller, which was implemented in [11].

The operational characteristics and performance differences of direct phase measurement and synchronous detection techniques for biomedical MIT were investigated and compared in paper [33]. According to the paper, direct phase measurement shows a performance advantage in terms of shorter data acquisition time and cost, due to its fast filter settling time and its relatively easy circuitry in the measurement system. The synchronous

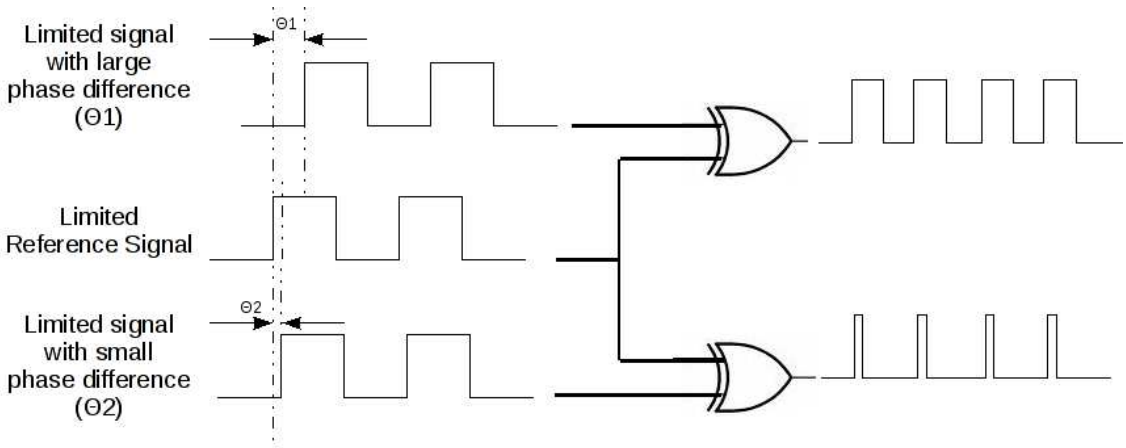

Figure 4.1: An example of using XOR Gate to extract phase difference information.

detection technique is favored because of its smaller phase drift. The most obvious difference between the two techniques is that the direct phase method can only provide the phase (related to imaginary component) information of the signal, while a synchronous detection system can provide both real and imaginary components.

For our MIT system, we chose the synchronous detection because it has better reported performance in terms of phase drift, which is the major performance limitation for MIT systems [33]. The synchronous detection method also provides more information about the measuring space. The operation theory of synchronous detection is discussed in the following section.

4.1 Operation Theory of Synchronous Detection

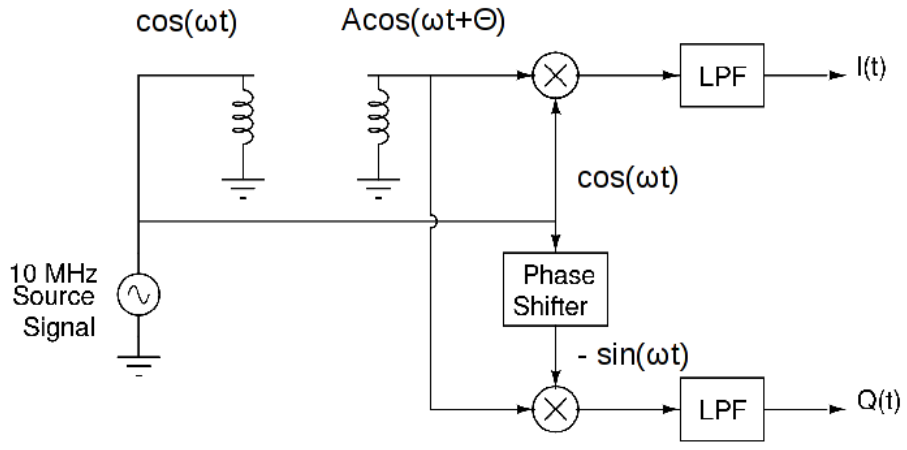

Figure 4.2: The principle of the synchronous detection technique.

Figure 4.2 shows the principles of synchronous detection. Consider a two channel MIT system, with one transmitting coil and one receiving coil. The transmitting coil is driven by a sinusoidal signal $\cos(\omega t)$. Due to the conductivity change within the measuring

space, the receiving signal that was picked up by the receiving coil will result in a magnitude change A and a phase change θ, which gives us:

$$A\cos(\omega t+\theta) \tag{4.1}$$

The driving signal $\cos(\omega t)$ is used as a reference for demodulation. The demodulation requires two reference signals, where one is the original driving signal, $\cos(\omega t)$, and the other one is the same as the driving signal but is delayed by a phase of 90°, i.e. $-\sin(\omega t)$. This can be achieved by passing $\cos(\omega t)$ into a phase lock loop (PLL) or a phase shifter. The received signal $A\cos(\omega t+\theta)$ is then multiplied with both $\cos(\omega t)$ and $-\sin(\omega t)$ by two mixers, which gives us:

$$\begin{aligned} A\cos(\omega t+\theta)\times\cos(\omega t) &= \frac{A}{2}[\cos(2\omega t+\theta)+\cos(\theta)] \\ &= \frac{A}{2}\cos(2\omega t+\theta)+\frac{A}{2}\cos(\theta) \end{aligned} \tag{4.2}$$

and

$$\begin{aligned} A\cos(\omega t+\theta)\times[-\sin(\omega t)] &= -\frac{A}{2}[\sin(2\omega t+\theta)-\sin(\theta)] \\ &= -\frac{A}{2}\sin(2\omega t+\theta)+\frac{A}{2}\sin(\theta) \end{aligned} \tag{4.3}$$

The output of the mixers contains direct current (DC) components, which are the in-phase (I) and quadrature (Q) signals. These I and Q signals contain the essential information for both phase and magnitude changes of the receiving signal. To extract the DC values, the mixer output needs to be passed through appropriate low pass filters:

$$\begin{aligned} I(t) &= LPF[\frac{A}{2}\cos(2\omega t+\theta)+\frac{A}{2}\cos(\theta)] \\ &= \frac{A}{2}\cos(\theta) \end{aligned} \tag{4.4}$$

and

$$\begin{aligned} Q(t) &= LPF[-\frac{A}{2}\sin(2\omega t+\theta)+\frac{A}{2}\sin(\theta)] \\ &= \frac{A}{2}\sin(\theta) \end{aligned} \tag{4.5}$$

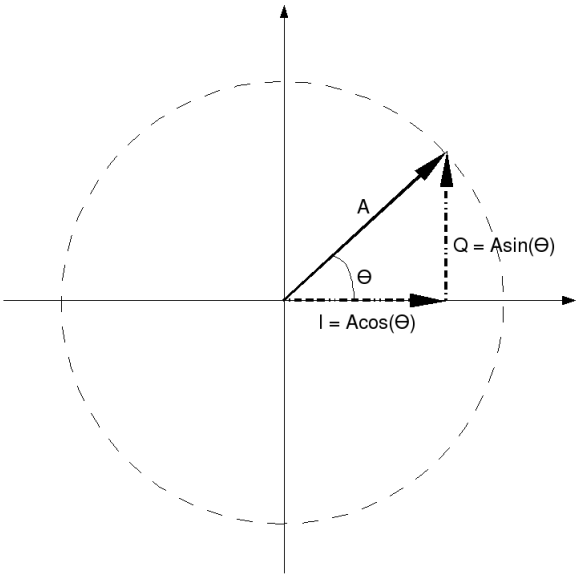

Figure 4.3: Phasor representation of $Ae^{-j\theta}$.

From Figure 4.3, one can see that the $I(t)$ and $Q(t)$ terms are actually the real and imaginary components of the phasor representation of the receiving signal $A\cos(\omega t+\theta)$, where I = Re($Ae^{-j\theta}$) and Q = Im($Ae^{-j\theta}$). The magnitude and the phase can therefore be worked out from $I(t)$ and $Q(t)$

$$\begin{aligned} Magnitude &= 2\times\sqrt{(I^2+Q^2)} \\ &= 2\times\frac{A}{2}\sqrt{(\sin^2\theta+\cos^2\theta)} \\ &= A \end{aligned} \tag{4.6}$$

and

$$Phase = arg\{I+jQ\} \tag{4.7}$$

4.2 Mixer Selection

Figure 4.2 shows that, in the I/Q demodulation process, mixers play an important role in generating I and Q outputs by mixing the receiving signal and the referencing signal. A good mixer can be selected based on the following properties: accuracy, stability (less drift), power consumption and cost. In theory, any good mixer can do the job. For example, the Analog Device AD831 double balanced, low distortion mixer is specially tailored for I/Q quadrature demodulation (up to 500 MHz). Any other balanced active or passive mixers which have IF output bandwidth extending down to DC can also be used.

However, there are some critical problems in this type of demodulator that demand a better mixer. For example, one key problem is that, if one's demodulator is built according to

Figure 4.2, with cables connecting between mixers and other modules, it is likely that there will be a local oscillator (LO) leakage signal running from the mixers' LO inputs into the mixers' radio frequency (RF) inputs. When this happens, undesired DC values are obtained from the mixers and these DC offset can cause the limiting when one applies baseband gain to the mixer output, which leads to an inaccurate result. Another typical difficulty is obtaining an accurate 90 degree phase shift in the LO over a broad range of frequencies, and related to this is the problem of maintaining good amplitude and phase balance between the two channels. To solve these problems, the IC manufacturers integrate both mixers along with a 90 degree phase shifter onto one IC. By doing this, a good matching between the mixers can be guaranteed, so that the amplitude balance of LO and RF to both mixers and the intermediate frequency (IF) output level matching from both mixers are good. They also integrate a LO circuit that includes a divide-by-two stage and a digital phase shifter. In this case, the input LO injection into the IC is at twice the desired LO frequency. So, even though the circuit layout allows signal to leak from the LO input pin to the RF input pin, which is hard to avoid, it has a much smaller effect because the frequency at the LO pin is doubled and will not be demodulated down to DC, which effectively eliminates the DC offset problem. Figure 4.4 shows an example of this type of architecture. The AD8348 is a 50 MHz to 1 GHz quadrature demodulator; it can be seen in its block diagram how the two mixers, a divide-by-two LO circuitry and a phase shifter are placed on one IC, and how all the inputs and outputs are buffered.

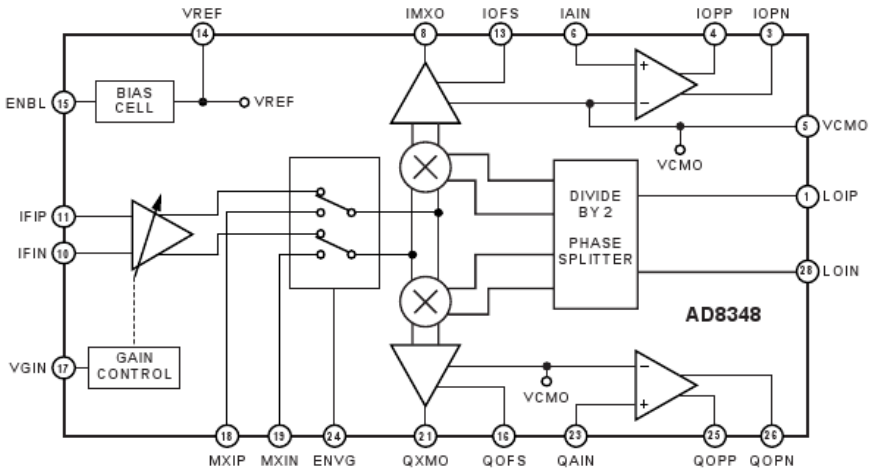

Figure 4.4: Block diagram of the AD8348 architecture (diagram from [54]).

It is quite possible that, for our selected frequency of 10 MHz, the problems of LO to RF leakage mentioned above may be fairly minor. With a good PCB layout, one may be able to construct an I/Q demodulator successfully with a less integrated design. However, utilising a suitable single IC for our I/Q demodulation is the preferred approach because we can then avoid the difficulties of constructing a high accuracy analog phase shifter at a high frequency.

4.2.1 Analog Device - AD8333 [55]

The AD8333 is a 32 pin, dual phase shifter and I/Q demodulator with a quadrature phase error less than 0.1°. It can be used for medical imaging (ultrasound beamforming) and phased array systems (radar and adaptive antennas) [55]. Its simplified functional block diagram is shown in Figure 4.5.

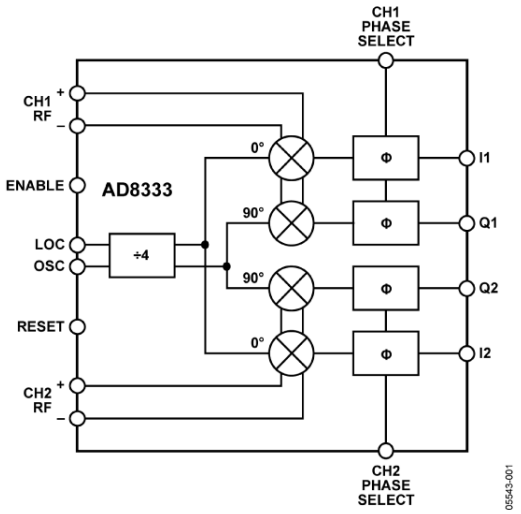

Figure 4.5: Functional block diagram of the AD8333 (diagram from [55]).

The AD8333 implements a 'divide-by-four' logic circuitry that digitally generates the internal square wave versioned $\cos(\omega t)$ and $\sin(\omega t)$ reference signals, which drive the mixers of a pair of matched I/Q demodulators. The divider is implemented such that the $4 \times$ LO signals reclock the final flip-flops that generate the internal quadrature signals, thereby minimising noise introduced by the divide circuitry and the signal leakage problem, as mentioned before. Implementing this logic circuitry also means that, the input signal should not contain any interference at harmonic frequency such as $3f_o$, $5f_o$ and $7f_o$, where f_o is the operating frequency, otherwise those harmonic signal will be down converted to DC, and affect the demodulation result.

Digital phase shifters are also implemented to compensate for the phase difference if there is an I/Q phase lead/lag between the channels. For example, if the reference signal applied to channel one (CH1) has a phase lag of 45° compared with the reference that is supplied to channel two (CH2), then one can use the built-in phase shifter to align the phase for both CH1 and CH2 by injecting the correct code into the CH2 phase select input.

The I/Q demodulators consist of double balanced Gilbert cell mixers. The RF inputs are converted into currents by trans-conductance stages, which allow a maximum differential input signal range of 2.8 Vp-p. These voltage signals are then passed into the mixers, which converts them into a DC base-band signal and a high frequency signal, and as il-

lustrated in Section 4.1. The IF signals are then injected into phase shifters, the amount of phase shift can be adjusted by applying different code to phase select input pins. Following the phase shifter, the differential current signal is converted from differential to signal ended via a current mirror. An external trans-impedance amplifier is needed to convert the I and Q current outputs to voltage. The AD8021, a low noise, high speed amplifier is used in the example of the datasheet.

The AD8333 is an ideal IC in terms of small quadrature phase error (typically $\pm 0.1^{\circ}$) and broad operating frequency range (up to 50 MHz), which would give us greater flexibility in frequency selection if the design would need to be altered in the future. The disadvantages of the AD8333 are that it is only available in a 32-Lead LFCSP (5mm $\times$ 5mm) package. This package is very difficult to solder with a soldering iron because the pads lie underneath the IC, which makes it extremely difficult to construct the prototype. A specially designed reflow soldering machine thus needs to be used to mount the chip onto a PCB. Figure 4.6 shows the size comparison between an AD8333 chip and a R1 coin.

Figure 4.6: Size comparison between a AD8333 and a R1 coin.

The AD8333's high power consumption (180 mW per channel) and high supply current (typically 65 mA) might become another issue of concern, especially for a tomography system, as it is usually involved with multi-channel design. Furthermore, the AD8333's huge power consumption would degrade the portability of the design, as it would no longer be possible to use batteries to supply the power for the entire tomography system.

The price for an AD8333 chip is 15.62 US Dollars. This price is taken from the Digi-Key Corporation, an electronic components distributor in USA.

4.2.2 Analog Device - AD607 [56]

The AD607 is a 3 V low power receiver IF subsystem for operation at input frequencies up to a limit of 500 MHz, and IFs from 400 kHz to 12 MHz. The IC contained a mixer, IF amplifiers, I/Q demodulators and a phase-locked quadrature oscillator. Figure 4.7 shows the AD607's simplified block diagram.

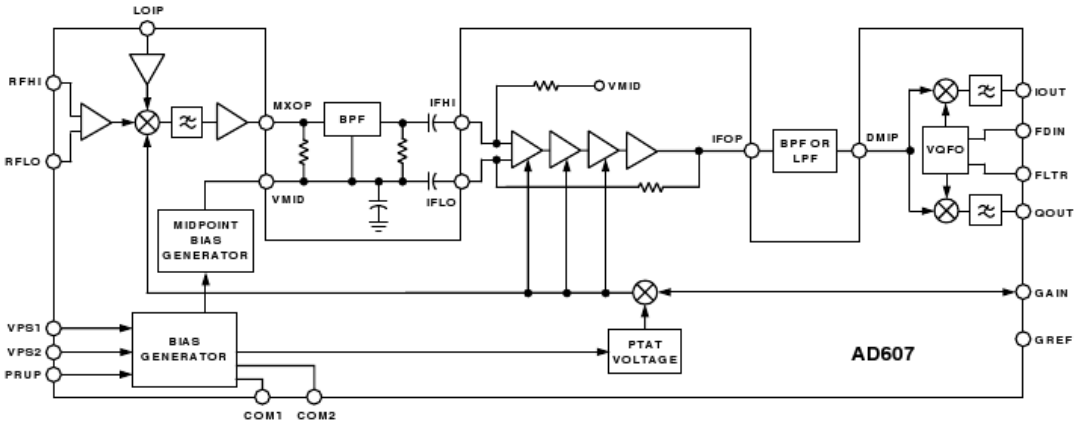

Figure 4.7: Functional block diagram of the AD607 (diagram from [56]).

The AD607 is an IC that provides most of the active circuitry required to construct a complete superheterodyne receiver, with a high input frequency limit up to 500 MHz. Figure 4.7 shows the block diagram of the main sections of the AD607. The IC includes a low noise, variable gain ultra-high frequency (UHF) mixer. This high intercept mixer is a double balanced Gilbert cell design; it also has a linear four-stages voltage controlled amplifier strip with a gain range more than 90 dB and I/Q demodulators. Each mixer is followed by a 2 pole, 2 MHz cut-off low pass filter, and a phase locked loop providing the in-phase and quadrature referencing clocks. A biasing system with CMOS compatible power-down completes the AD607.

For a MIT system, the received signal is a very small magnetically induced voltage signal picked up by the sensor coil (≈10 mV to 30 mV). To enlarge the signal and increase the sensitivity, an amplification stage is necessary. The voltage controlled IF amplifier strip within the AD607 can do the job easily, as most of the gain in the AD607 arises in this stage, thus contributing a maximum gain that exceeds 90 dB ($G = 10^9$) , with a noise figure of 17 dB (operating frequency = 10.7 MHz, gain = 90 dB). The amount of gain is controlled by the voltage which appears at the Pin GAIN. This external voltage control input can either come from an external automatic gain control (AGC) detector or from a digital to analog converter (DAC). More importantly, the overall gain is linear in dB with respect to the external voltage input at the Pin GAIN. This feature makes the gain even more controllable. If using a +5 V supply, the datasheet suggested the gain control voltage should range from 3.333 V to 0.667 V, which gives a scale factor of 33.33 mV/dB and contributes a gain from 7.5 dB to 67.5 dB respectively.

The AD607 has a built-in I/Q demodulator that is driven by the quadrature signals that are generated by a variable frequency quadrature oscillator (VFQO), phase locked to the external reference signal that is applied to the Pin FDIN. VFQO ensures good phase accuracy, as well as low electromagnetic interference (EMI) and power consumption. The PLL uses a sequential-phase detector (SPD), implemented in low-power current-mode logic, and a charge pump, which can source or sink 40 µA. Both demodulators (I and Q) received their inputs at the Pin DMIP, and each of them comprises a full-wave syn-

chronous detector, producing single ended base-band output at the pins IOUT and QOUT. The quadrature phase error of this VFQO is typically -1.2°at 10.7 MHz; it was not stated clearly in the datasheet whether this phase error would remain constant with temperature for a specific IC. The PLL uses a sequential phase detector that comprises low power emitter coupled logic and a charge pump.

Compare to the AD8333, the AD607 has disadvantages such as its smaller operating frequency range and its relatively large quadrature phase error. Although it is not stated very clearly in the datasheet, it is considered that the phase error specified by the IC maker is a steady and constant phase error, under the assumption that there is only one carrier frequency. A steady state phase error would generate a scaling error in the I/Q output signals, it is believed that the scaling error can be compensated or calibrated out by using the software. The advantages of using the AD607 would be its built-in IF amplification strip, which can largely increase the system's sensitivity; its low power consumption: at a 3 V supply, a typical supply current is 8.5 mA at midgain, corresponding to a 25 mW power consumption. And also, the AD607 comes in a 20-Lead shrink small outline package (SSOP), which is more easily soldered onto a PCB than the AD8333's 32-Lead LFCSP package.

After serious consideration, the AD607 was selected to perform the I/Q demodulation, as it was agreed that the 20-Lead SSOP would be a much more suitable package for prototyping. The AD607's low power consumption also makes it a more appropriate IC to be part of a portable device, which is a key parameter for a tomography system. More importantly, the price of an AD607 is cheaper than an AD8333. From the Digi-Key Corporation website (www.digikey.com), an AD607 IC costs 7.30 US Dollars, which is less than 50% of the price of an AD8333.

4.3 Using the AD607 [56]

This section will focus on a few areas of special importance of using the AD607. The AD607 is a wide-band high frequency component, and is thus the key component that determines the quality of our demodulation circuit. Great care is needed when laying out the circuit. Figure 4.8 shows a schematic design of the peripheral components around the AD607. The EagleCAD program was used to design the schematics and layout the PCB.

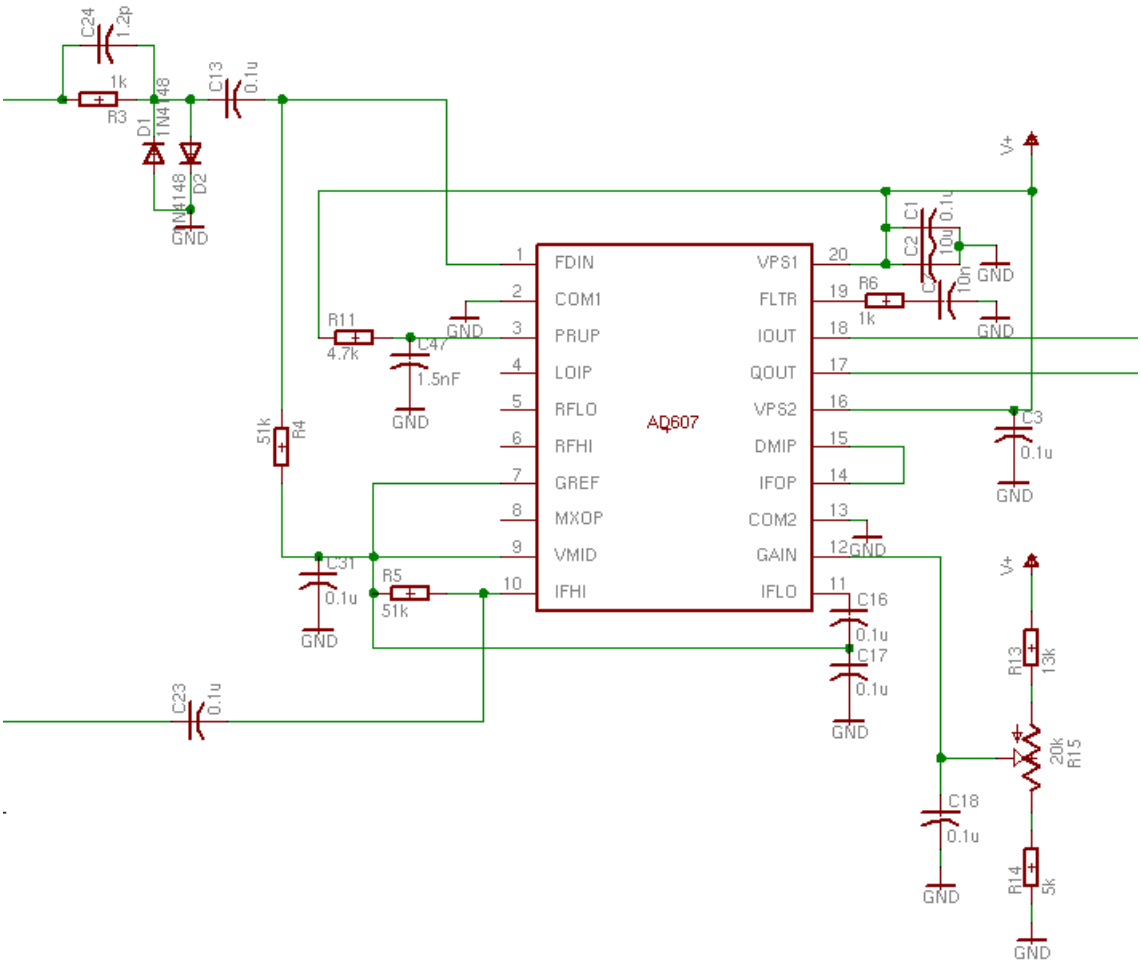

Figure 4.8: Schematic diagram of the AD607.

The AD607 consists of a variable gain UHF mixer, a linear four-stages voltage controlled amplifier strip and an I/Q demodulator. In our design, only the amplifier strip and the I/Q demodulator will be utilised, as the heterodyning stage will not be involved in the MIT system. Thus Pin 4, 5, 6 and 8 of the AD607, which are the inputs (RF and LO) and outputs (IF) of the mixer, are not connected.

4.3.1 Bias System

The AD607 operates from a single power supply, any voltage from 2.92 V to 5.5 V can be used. All the input signals must be biased at the midpoint of the supply ($V_p/2$). An independent mid-supply bias generator is implemented in the AD607, which generates a voltage at $V_p/2$, which appears at the Pin VMID at a low impedance. There are two suggested biasing methods in the data sheet, which are shown in Figure 4.9.

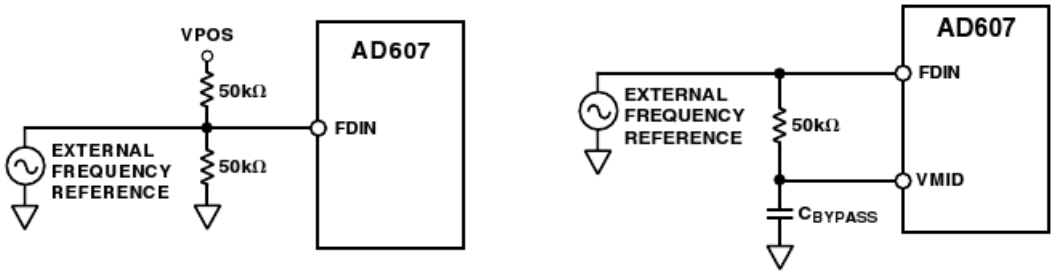

Figure 4.9: Suggested methods for AD607 input biasing (diagrams from [56]).

Our design used the Pin VMID to bias the external frequency reference. The mid-supply voltage which appeared at this pin does not shut down when the AD607 is disabled, ensuring that all the major signal interfaces remain biased at all times, and thus minimising the transient disturbances at power-up and allowing the use of substantial decoupling capacitors at all the inputs.

4.3.2 Diode Clipping Circuit

The quadrature demodulator with the AD607 requires an external driving signal, with a maximum amplitude of ±400 mV. The signal is fed into the Pin FDIN and must be biased at $V_p/2$ as well. For the sake of design simplicity, the 10 MHz, 4 Vp-p driving signal that is applied to the coil during transmission was used as the reference source for the AD607 as well. However, the signal's amplitude needed to be reduced to ±400 mV so that it would not exceed the maximum input limit of the Pin FDIN. Fortunately, the reference input for the VFQO does not necessarily need to be sinusoidal, since the VFQO is a logic circuit and all inputs will eventually be converted into limited logic signals. Therefore, the simplest solution to reduce the reference signal's amplitude was to use a diode clipping circuit.

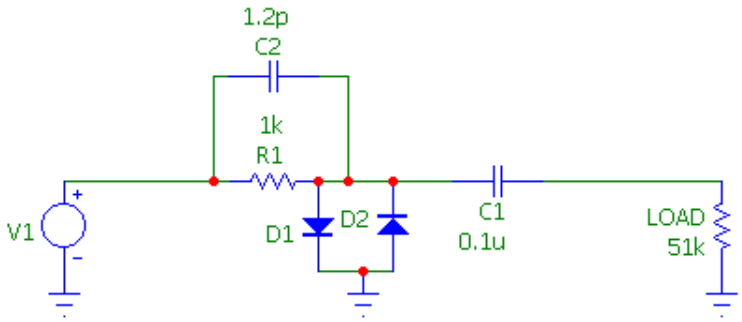

Figure 4.10: Schematic diagram of a diode clipping circuit.

Figure 4.10 shows a typical schematic diagram of a diode clipping circuit. The clipping voltage value is determined by the diode's maximum forward voltage drop, therefore diodes play an important role in this circuit. The HP 5082-2835 schottky barrier diode is

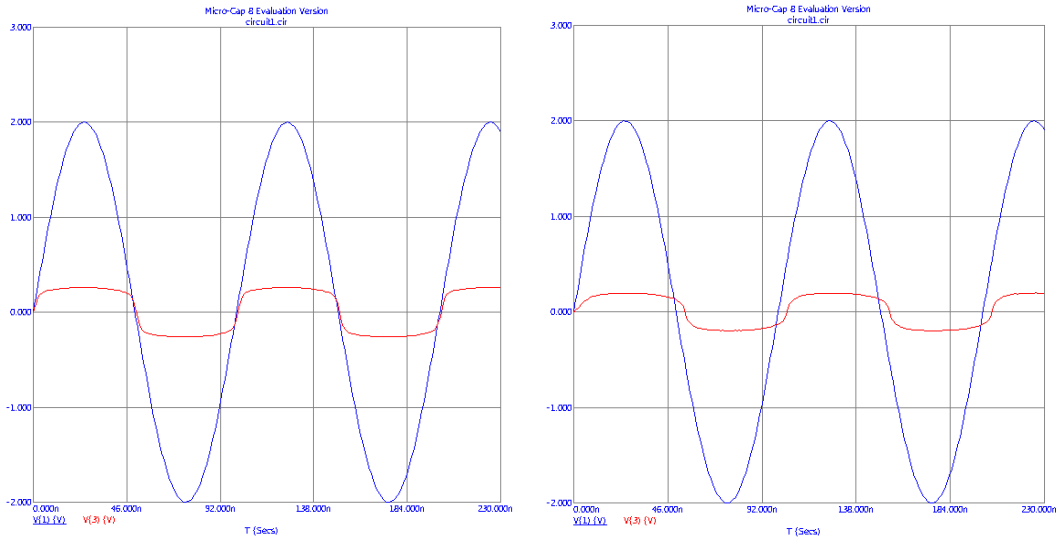

(A) (B)

Figure 4.11: The comparison between the 4 Vp-p, 10 MHz input signal and the output signal of the diode clipping circuit (A) with and (B) without the phase compensation capacitor.

chosen because of its high switching speed (pico-second) and low junction capacitance (1 pF at 1 MHz). The HP 5082-2835 also has a low turn-on voltage of 0.34 V at 1 mA, which will clip the 10 MHz input signal at $\pm$340 mV.

The junction capacitance of the diodes can introduce a phase mismatch between the input and the output of the clipping circuit. This phase shift might create a voltage offset at the I/Q demodulator's output since the reference signal that is fed into the AD607 will not have the same phase as the original signal. To compensate for the phase shift, the capacitor C2 is added in parallel with the input resistor (see Figure 4.10). The selection of the capacitor's value is essential, as the capacitance value determines the amount of phase shift compensation. Simply using a oscilloscope by probing the input and output of the clipping circuit is not an appropriate way to measure the amount of phase shift, since the probe itself can also introduce extra capacitance ($\approx$3 pF).

The capacitor value was chosen by the software simulation using Micro-Cap, Version 8.0. Figure 4.11 showed the input/output comparison when the compensation capacitor was presented and when it was not added. The SPICE parameters of the HP 5082-2835 could be found in its datasheet, and were thus used in the simulation to ensure that it was accurate.

After the simulation had been done, it was discovered that the presence of a 1.2 pF capacitor could give the optimum phase compensation.

4.3.3 IF Amplifier

The AD607 consists of a linear four-stage IF amplifier strip, which together provides a voltage controlled gain of more than 90 dB. The IF inputs are differential. The Pin IFHI

(non-inverting relative to the IF output) and the Pin IFLO (inverting) are the input pins. Figure 4.12 shows a simplified schematic of the IF interface.

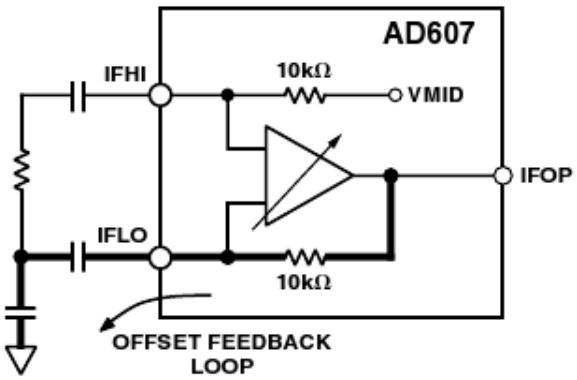

Figure 4.12: Simplified schematic diagram of the IF interface (diagram from [56]).

Since the IF amplification stage contributes a large amount of gain, any input offset voltage appear at this stage would cause a large DC output error, especially at high gain. This problem can be nulled by adding some capacitors at the inverting input, which creates an AC path to ground and thus forms a low pass feedback path from the IF output, as shown in Figure 4.12. The final stage of the IF amplification strip provides differential to single-ended conversion, therefore the signal at the output of the IF amplifier (Pin IFOP) is a low impedance single sided voltage, centered at $V_p/2$ by the DC feedback loop. It may be loaded by a resistance as low as 50 Ω, which is normally connected to the Pin VMID.

In our design, the IF output signal is directly fed into the Pin DMIP, the input of the quadrature mixers. No filtering stage is involved at the IF output. It is recommended in the datasheet, however, that a post IF filtering is needed in order to remove the interference at the harmonics frequencies, as they will also be converted to DC during the I/Q demodulation process. A bandpass filter would be added if the harmonic interference become an issue in an industrial environment.

4.3.4 PLL loop filter

The extra resistors and capacitors connected to the Pin FLTR are used for the disable function of the AD607. Although switching off the IC saves power, in general, it is not wise to 'power down' an individual IC to save power, as this simple approach may cause some problems. For example, when the supply to an IC is turned on and off, its decoupling networks will charge and discharge. These charging and discharging times need to be added to the system's power-up and power-down times, which means the power-up and power-down times need to be longer to allow extra time just for charging and discharging the decoupling networks. Thus an IC without an internal power-down function can be at a disadvantage.

If an IC has an internal power-down, like the AD607, its power supply input pin presents a high impedance to the decoupling network during shutdown, without charging and discharging the network on power-up and power-down, which speeds up the turn on/off response time.

The variable frequency quadrature oscillator (VFQO) inside the AD607 operates from 400 kHz to 12 MHz and is controlled by the voltage between Pin VPOS and Pin FLTR. Some external circuitry is required to hold a specific voltage at the PLL's loop filter output (Pin FLTR) when the AD607 is powered down, in order to minimise frequency reacquisition time upon power-up. In normal operation, a series resistors and capacitors (RC) network forming the PLL loop filter is connected from the Pin FLTR to ground. In the AD607's datasheet, a 1 kΩ resistor and a 10 nF capacitor are used. The use of the integral sample and hold system ensures that the frequency control voltage at Pin FLTR remains held during power-down, so that reacquisition of the carrier signal can occur in as short as 16.5 μs [56].

In practice, the probability of a phase mismatch at power-up is high, so the worst case linear settling period to full lock needs to be considered when designing the filter. The settling period is typically 16.5 μs at an IF of 10.7 MHz for a ±100 mV signal at Pin DMIP and FDIN.

4.3.5 Fast PRUP Control Signal

The Pin PRUP is a power-up control input of the AD607. If a logic high is inserted, the chip is in the active mode; a logic low will put the chip into the idle mode, with a standby current of 550 μA only. Thus this pin can be used to disable the chip when it is not used, which can further decrease the system's power consumption.

However, if the PRUP control signal is applied with a rise time of less than 35 μs, anomalous behavior occasionally occurs. The symptoms include low gain, oscillations at the I/Q output of the device, or no valid data occurring at the output of the AD607. The problems cause no damage to the chip, so it will often operate normally again when it has been reset.

To avoid this problem, we had to make sure that the rise time of PRUP signal was more than 35 μs. If the PRUP rise time was slower, then the anomalous behavior would disappear. This could be realised by connecting a simple RC circuit to the PRUP pin, where R can be 4.7 kΩ in series with a 1.5 nF shunt capacitor. This configuration gave us a time constant $\tau = 7.05\mu$s, which meant that the PRUP signal would take about $5\tau = 35.25\mu s$ to be fully charged (99.3 %).

In our design, since each channel was required to perform I/Q demodulation all the time, the AD607 had to remain in the active mode all the time, therefore the PRUP pin was connected to the supply voltage with a RC circuit in between, as shown in Figure 4.8.

4.3.6 Gain Scaling and Gain Distribution

The IF gain of the AD607 is linear in dB with respect to V_G, the voltage at the Pin GAIN. The gain of all IF amplifier stages is at its maximum when V_G is 0, and reduces progressively up to $V_P - 0.8V$. So for example, if the supply power, V_P, is +5 V, the total IF gain will be at its minimum when V_G is 4.2 V. The AD607 also features temperature compensation of the gain scaling. The gain control scaling is proportional to the reference voltage that is applied to the Pin GREF. When this pin is tied to the Pin VMID, as is normally done, the scale is nominally $(V_P/150)$ volts/dB. Therefore, for a +5 V supply, the scale becomes 33.33 mV/dB (30 dB/V), with a proportional change in the V_G. The appropriate range for V_G, suggested in the datasheet, is 0.667 V $\leq V_G \leq$3.333 V, which is equivalent to 67.5 dB ($\approx$5620000) $\leq$ gain $\leq$7.5 dB ($\approx$5.62).

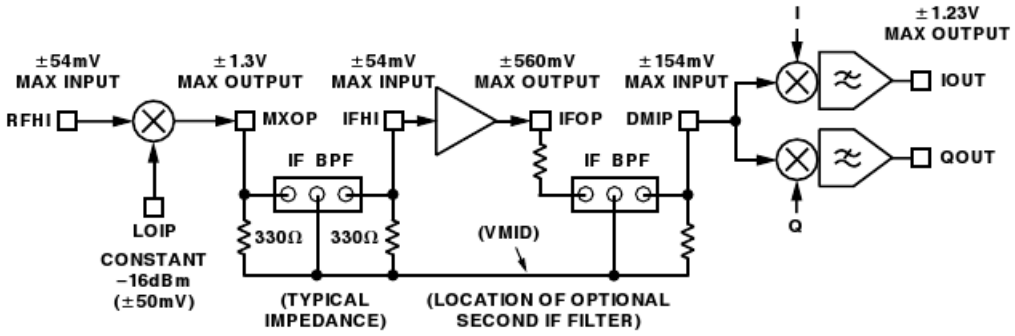

Figure 4.13: Maximum signal levels at each stage in the AD607 (diagram from [56]).

Figure 4.13 shows the maximum input/output levels at each stage in the AD607. In order to maintain the linear operation, it is important to make sure in the design process that all the input signals at each stage must be kept within the maximum signal level. When setting the IF Gain, one needs to be careful that the signal level at the Pin DMIP does not exceed $\pm$150 mV, as signal levels above this will overload the I/Q demodulator, and will give us the outputs that have non-linear behaviors. The maximum input level can be used to decide the magnitude of the excitation signal and the appropriate distance between the coil sensors.

4.3.7 General Circuit Layout Design

The AD607 is a high speed, low power receiver IF subsystem. To deal with the IC which has such a high operating frequency, a good PCB layout is essential, as an incorrect PCB layout will increase the noise interference and therefore degrade the chip's performance. This section will briefly list some PCB layout tips for routing the AD607's input and output. A detailed discussion on high speed PCB layout is given in Appendix B.

- Firstly, place as much ground plane as you can on every side of the board. If possible, a full ground plane covering the back side of the board or an internal layer is recommended.

- Secondly, route RF and LO traces first, as they are the main signal paths of the receiving circuit, so that they can remain as short as possible. One must also avoid routing RF and LO traces travel near each other or side by side and avoid them crossing over each other to prevent crosstalk between two signals. If they must cross, they should cross each other at right angles to minimise the coupling effect.
- For isolation between two signals, make sure there are ground traces or ground planes between them. All circuit ground connections should be connected immediately to the ground plane through a via.
- Finally, be aware of the impedance of RF and LO trances, and thus keep them relatively short and of consistent width.

In fact, the greater concern will be that the signal generator may have a phase noise exceeding the amount of the desired signal, which can lead to erroneous I/Q outputs. This LO phase noise might be a much bigger problem to overcome. For future development, the LO signal generated by the signal generator should be replaced by either a DDS chip or an LC oscillator. Further investigation is necessary to decide whether the DDS can deliver better phase noise than an LC oscillator. At 10 MHz, one should be able to build a very quiet LO using an LC oscillator design, which is a simpler option. However, using a DDS with two channels has the advantage of adjusting the phase relations between the two outputs, which would be a useful way of adjusting the phase of the reference signal fed to the demodulator chip.

Chapter 5

Post Demodulation Signal Conditioning

In the AD607, I/Q demodulation is accomplished by using two synchronous detectors (see Figure 4.7), with $\sin(\omega_0 t)$ and $\cos(\omega_0 t)$ as the reference, followed by internal, two-poles low pass filters (LPF) with a cut off frequency of 2 MHz. The outputs of the low pass filters appear at the Pin IOUT and QOUT of the AD607 respectively, with a maximum ± 1.23 V output swing biased at $V_P/2$.

An extra low pass filtering stage is essential in our design. Its function is to filter out the $2\omega_0$ demodulation product and all the other high frequency components completely, since in I/Q demodulation, we are only interested in the DC output signal. More importantly, the bandwidth of the filters determine the key tomography system performance parameters, such as the effective noise level and the image capture rate. Typically, the value of excitation frequency should be at least ten times larger than f_c to ensure adequate noise rejection, where f_c is the -3 dB bandwidth of the output LPF. For example, an eight channel tomography system with a 10 kHz bandwidth LPF will have a complete settling time for one excitation of approximately 500 μs, which limits the maximum image capture rate of 250 frames/s.

A level shifting stage is implemented in our design prior to sampling, as different data acquisition (DAQ) tools can have different input range limits. For example, a USB-DUX (a USB based DAQ for Linux platform) has an input range from -5 V to +5 V; a microcontroller's built-in ADC generally has a range from 0 V to its supply voltage, like +5 V (PIC18F series) or +3.3 V (dsPIC33F series). Thus by adding level shifters with gain, the output range can be controlled better and thus giving us more flexibility when choosing the DAQ hardware.

In this chapter, the design of both the low pass filter and the DC level shifter will be discussed.

5.1 Low Pass Filter

In general, filters can be divided into two categories: active filters and passive filters. A passive filter is a filter that is constructed with passive components, such as resistors, capacitors and inductors, An active filter implements both op-amps and passive components. There are several reasons why we chose an active filter topology instead of a passive RC filter, although the passive filter would have been much easier to design and implement [57]:

- A first or second order RC passive filter may not give adequate roll-off (one can not achieve a high Q stage as required for filters like Chebyshev)
- The passive filter cannot contribute any gain, if it is required in the circuit.
- The passive filter can potentially have high output impedance, since the resistor value in the RC combination is usually large to keep the capacitor at a reasonable value; the next circuit stage to which the filter output is connected to would thus see a large source impedance.

The Sallen–Key filter is a type of active Butterworth filter that is particularly valued for its simplicity. The circuit produces a 2-pole low pass (or high pass) frequency response using two resistors, two capacitors and an amplifier. Higher order filters can be obtained by cascading two or more stages. Figure 5.1 shows an example of the unity gain low pass configuration. The Sallen-Key topology was selected because it was easy to design, and it required only one op-amp, which made it relatively inexpensive.

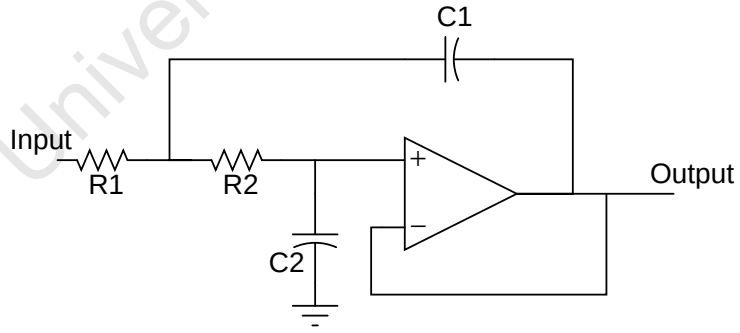

Figure 5.1: Schematic diagram of one stage Sallen-Key low pass filter.

For the topology above, its transfer function is given by [58]

$$H(s) = \frac{1}{1 + C_2(R_1 + R_2)s + (C_1 C_2 R_1 R_2)s^2} \tag{5.1}$$

where the cut-off frequency f_c and the quality factor Q are

$$f_c = \frac{1}{2\pi\sqrt{R_1 R_2 C_1 C_2}} \tag{5.2}$$

and

$$Q = \frac{\sqrt{R_1 R_2 C_1 C_2}}{C_2(R_1 + R_2)} \tag{5.3}$$

A low cut-off frequency of 100 Hz was selected, to get the best noise performance. The image capture rate was not such a big concern for our prototyping system. In our design, R_1 and R_2 were chosen to be 100 kΩ, C_1 was 20 nF and C_2 was 10 nF. This combination gave us a bandwidth of f_c = 112.54 Hz and $Q = 1/\sqrt{2}$, which had a time constant of around $t = 10$ ms. To allow the LPF output to reach the steady state, a 50 ms settling time was a good approximation. If there were eight channels in the system, the total sampling time would be 50 ms × 8 = 400 ms. In addition, the channel switching time and the data acquisition time had to be taken into consideration. Approximately 500 ms was required for the system to complete a full set measurement, which gave us an image frame rate of 2 frames/s, a relatively slow image refresh rate for a tomography system. The filter's schematic and simulated frequency responses are shown in Figure 5.2; the simulation is done with Micro-Cap, Version 8.0.

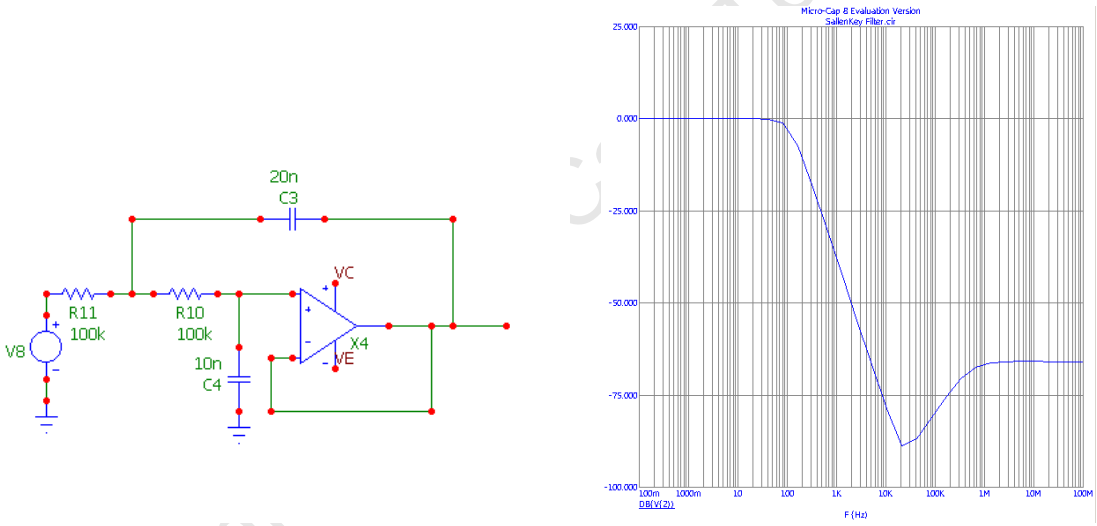

(A) (B)

Figure 5.2: Sallen-Key low pass filter's (A) schematic diagram and (B) its simulated frequency response.

In theory, the magnitude response within the stop band should keep decreasing at a constant rate (-40 dB/decade) as frequency increases. In reality, though the response actually starts to rise again at a high frequency, as shown in Figure 5.2 (B). This is due to the limitation of the real world op-amps, which lose voltage gain at a certain frequency due to their finite bandwidth. Therefore, a properly functioning op-amp is essential to the filter's operation. A LF353 JFET op-amp was selected in our design because of its availability and because it was cost effective.

5.2 Level Shifter

In instrumentation electronics, it is common to have a stage which converts a positive and negative signal into a range suitable for a single supplied ADC. A simple op-amp level shifter can easily achieve this, for example, a level shifter can convert a ± 5 V signal into a 0 to 3.3 V signal so that it can be sampled by an ADC that is built inside a +3.3 V supplied micro-controller.

The level shifter is usually involved with an op-amp, and is sometimes called an adder, as a DC offset is added to the incoming signal. In general, there are two types of level shifters: non-inverting and inverting.

5.2.1 Non-inverting Level Shifter

The schematic of a non-inverting level shifter is shown in Figure 5.3:

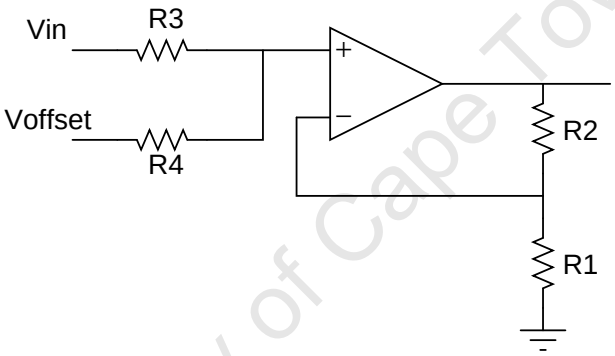

Figure 5.3: Schematic diagram of a non-inverting level shifter.

The output of the non-inverting level shifter is:

$$V_o = \frac{R_1 + R_2}{R_1}\left(V_{in}\frac{R_4}{R_3 + R_4} + V_{offset}\frac{R_3}{R_3 + R_4}\right) \tag{5.4}$$

The input signal thus has a gain V_o/V_{in} of

$$A = \frac{R_4}{R_3 + R_4} \times \frac{R_1 + R_2}{R_1} \tag{5.5}$$

For simplicity, if we make $R_1 = R_3$, and $R_2 = R_4$, then

$$A = \frac{R_4}{R_1} \tag{5.6}$$

The gain of the offset voltage will be:

$$A_{offset} = \frac{R_3}{R_3 + R_4} \times \frac{R_1 + R_2}{R_1} = \frac{R_3}{R_1} \tag{5.7}$$

If $R_1 = R_3$, then the gain of the offset voltage is 1.

5.2.2 Inverting Level Shifter

The schematic of an inverting level shifter is shown in Figure 5.4:

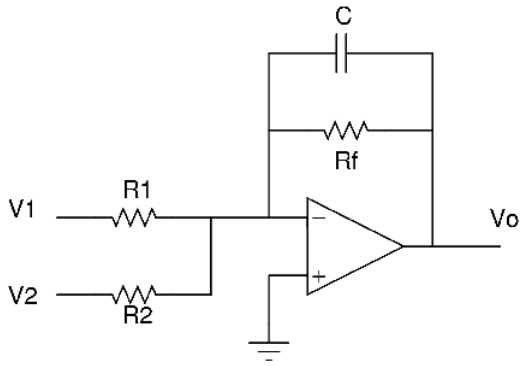

Figure 5.4: Schematic diagram of an inverting level shifter.

This level shifter is also known as an inverting summer. The output of the level shifter is

$$V_o = -\left(V_{in}\frac{R_f}{R_1} + V_{offset}\frac{R_f}{R_2}\right) \tag{5.8}$$

As can be seen, the gain for each input can be controlled by a single resistor, which keeps the interaction between inputs at a minimum. This makes this circuit preferable. It also means one can change the gain or add another input without affecting the gains of the other inputs. By adding a capacitor parallel with R_f, an extra pole is introduced at $f_c = \frac{1}{2\pi R_f C}$, which forms a low pass filter with a cut off frequency f_c.

One must take care to ensure, though, that this circuit will invert the input signal. However, it is believed that the inverted I and Q DC output signals can be adjusted back easily in the software calibration stage.

Both types of level shifting circuits can do level shifting perfectly. In our design, we chose to implement the inverting level shifter because of its simplicity and channel independence.

Chapter 6

Channel Switching, Voltage Gain Control and Data Acquisition

A detailed investigation was presented in Chapter 3 to Chapter 5 of each stage of the electronics design for the MIT transceiver circuit. Figure 6.1 shows a simplified block diagram of the analog measurement system. The final schematic of the board can be found in Appendix E. Figure 6.2 shows the PCB layout for our final board design. Once the board was assembled, the next tasks were to use the digital signal to control the board and to start taking samples from the I/Q outputs, which is discussed in this chapter.

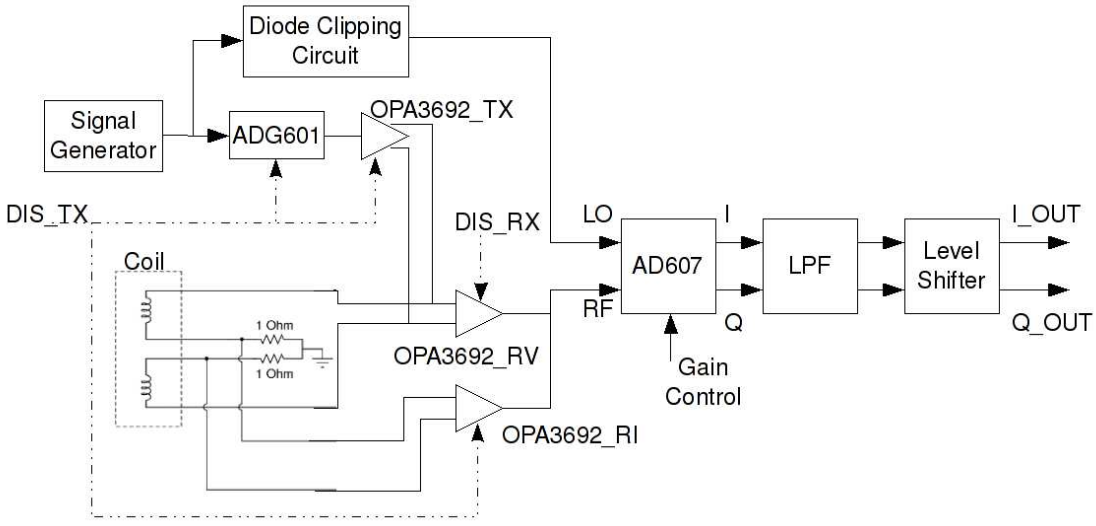

Figure 6.1: Circuitry block diagram.

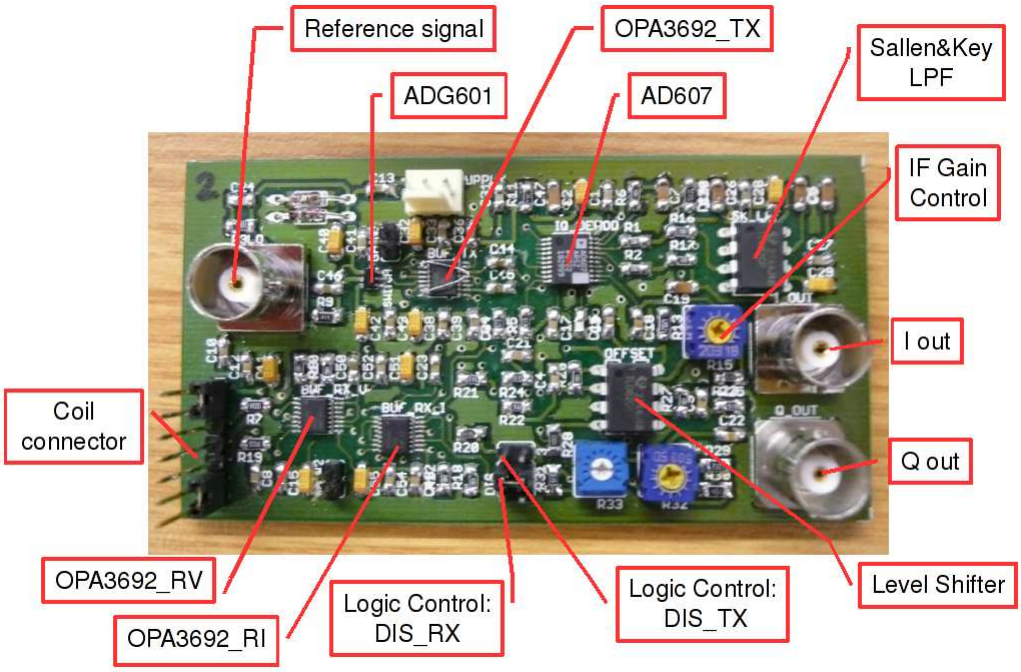

Figure 6.2: Final PCB layout of the analog measurement electronics.

6.1 Channel Switching and Voltage Gain Control

In our design, three OPA3692 buffers are implemented, namely OPA3692_TX, OPA3692_RV and OPA3692_RI, as shown in Figure 6.1, where TX denotes 'transmit', RV denotes 're-ceiver voltage' and RI denotes 'receiver current'. The OPA3692 has a disable feature which can isolate its input and output, like an analog switch. When the OPA3692 is in the normal operating state (i.e. a logic 'high' signal is applied to the'disable' pins on the IC), its input impedance is typically 100 kΩ ||2 pF, however, when the OPA3692 is disabled (i.e. a logic 'low' signal is applied to the'disable' pins on the IC), both its input and output can be viewed as a high impedance state of 1 MΩ in parallel with 2 pF, which offers a -68 dB isolation at 10 MHz. This function allows the circuit to switch between the transmitting mode and the receiving mode.

There are two logic control pins in the circuit: one controls the transmitting state (DIS_TX) and the other controls the receiving state (DIS_RX) of the board. It is designed in such a way that, when the Pin DIS_TX is applied with a logic high and the Pin DIS_RX is applied with a logic low, the coil sensor is in the transmitting mode. In this case, the 10 MHz source sinusoidal signal flows through the OPA3692_TX and drives the coil. The OPA3692_RV that buffers the input receiving signal is disabled, which offers a high impedance at its input and output. The OPA3692_RI that measures the current flowing through the driving coil is enabled, which allows self trans-impedance to be measured. The signal flowing diagram is illustrated in Figure 6.3.

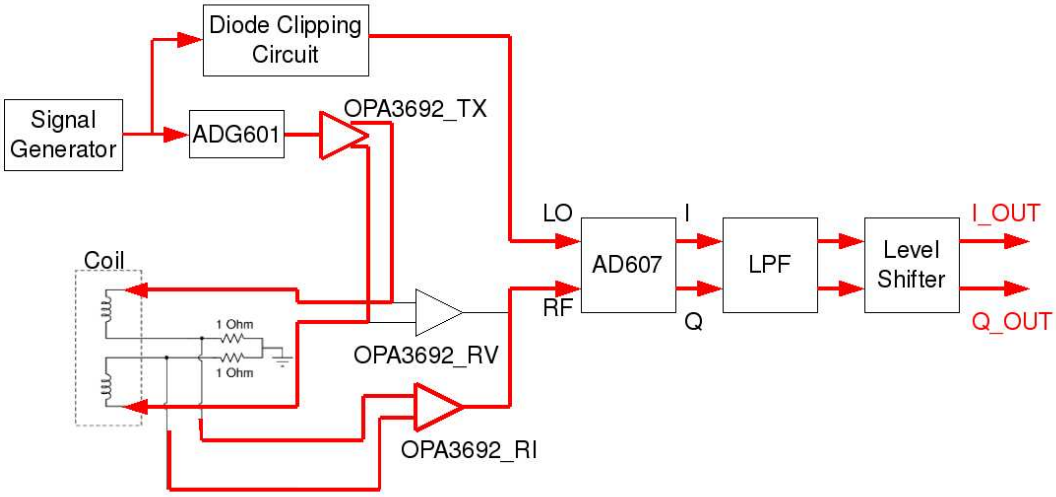

Figure 6.3: Signal flows in the transmitting mode.

When the DIS_TX input is applied with a logic low and the DIS_RX input is applied with a logic high, the coil sensor is in the receiving mode. In that case, the OPA3692_TX that buffers the 10 MHz reference signal has to be disabled, as we do not want the reference signal to interfere with the sensor coil measurement. The OPA3692_RI that measures the current signal must be disabled as well, as the changing flux in the transmitting coil can only induce a voltage at the sensor coil; in theory, therefore, there should be no current flow at the receiving sensor coil, as it is connected to the IC with a very high input impedance (≈100 kΩ). Figure 6.4 shows the signal flows in the circuit when the board is in the receiving mode.

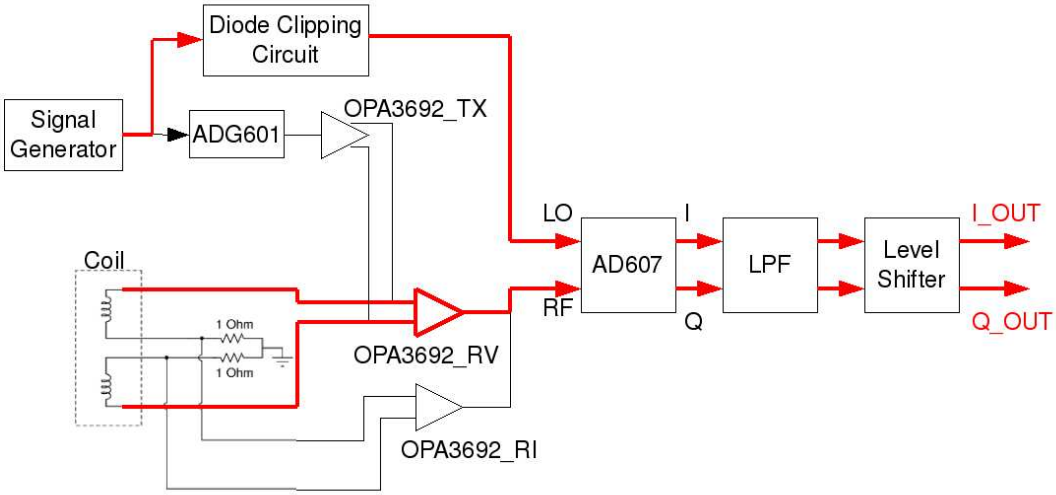

Figure 6.4: Signal flows in the receiving mode.

The Microchip dsPIC33FJ256GP710 was selected to perform the channel logic switching between the boards, due to its availability at UCT and its potential to be used for our

future development. Each of our transceiver board required two control logic signals, thus for an eight channel tomography system, $2 \times 8 = 16$ control signals were needed. The dsPIC33FJ256GP710 is a high performance, 16 bit digital signal controller which has up to 85 programmable digital I/O pins, which is more than sufficient to control a 16 channel MIT system. To program the micro-processor , MPLAB Integrated Development Environment (IDE) and In-Circuit Debugger (ICD 2) are used. MPLAB IDE is a free integrated toolset for embedded system design employing Microchip's microcontrollers; MPLAB ICD 2 is a real time debugger and programmer for both PIC series and dsPIC series microcontroller, ICD2 supports both USB and RS-232 interface to host PC. The dsPIC33FJ256GP710 with its evaluation board and the ICD 2 debugger are shown in Figure 6.5:

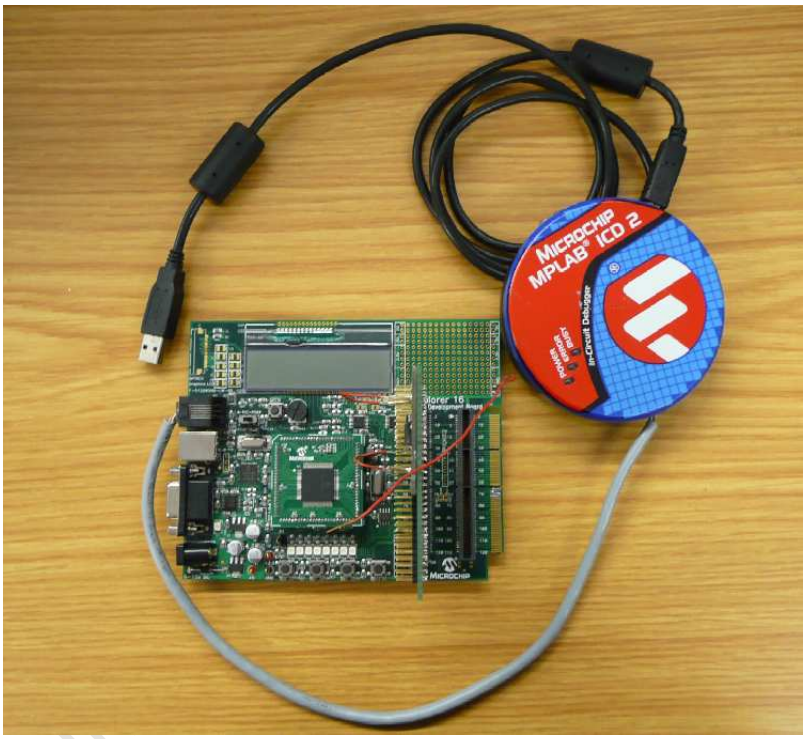

Figure 6.5: The dsPIC33FJ256GP710 on the Explorer 16 evaluation board, with a MPLAB ICD2 debugger.

Each of our transceiver circuits requires an analog DC voltage signal to control the gain of the IF amplifier inside the AD607. For the prototyping circuit, a potentiometer was used to generate a controllable DC voltage that could be used to control the amplification, as shown in Figure 6.2. However, when a multi-channel system is developed in the future and the channel switching is involved, the potentiometer was not suitable for gain control, since the control voltage could only be adjusted manually. A DAC is thus required to generate the gain control signal and perform the electronic switching.

The TLV5630 is an 8 channel, 12 bit, 2.7 V to 5.5 V low power DAC. With a +5 V power supply, its output voltage can be varied from 0 V to 4.6 V, which covers the entire range of the AD607's gain control voltage (0.667 V $\leq V_G \leq$ 3.333 V, see Section 4.3.6). Its low power consumption (18 mW) and fast switching speed (3 μs) also make it suitable for use

in a portable device and for gain adjustment switching [59]. The TLV5630 supports the 16 bits serial peripheral interface (SPI), as the 16 bit serial string can be generated straight from the dsPIC microcontroller in one command line, because the dsPIC33FJ256GP710 is a 16 bit microcontroller.

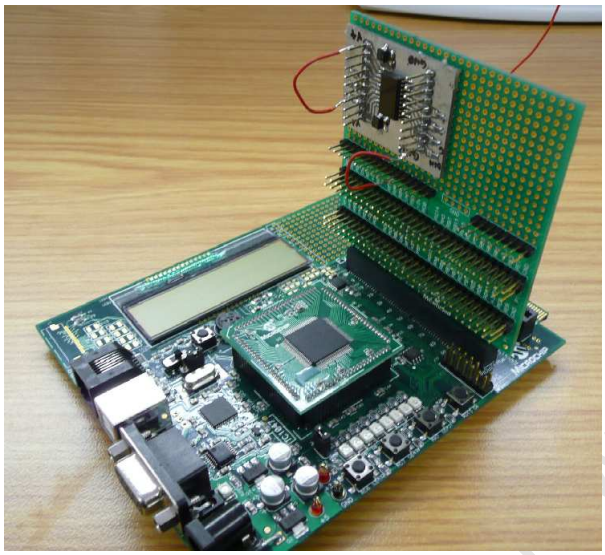

Figure 6.6: TLV5630 circuit board on the Explorer 16 daughter board.

The TLV5630 comes with a 20 pin small outline package (SOIC). Figure 6.6 shows its package appearance and how it can be connected to the dsPIC33FJ256GP710's evaluation board via a daughter board.

6.2 Data Acquisition

The objective of our electronic circuit design was to convert the receiving signal picked up by the sensor coil into the I and Q voltage DC signals. After the conversion, the next stage was the data acquisition.

Data acquisition is the sampling of the real world signal to generate data that can be processed by a computer, sometimes abbreviated DAQ. Data acquisition typically involves acquisition of signal waveforms and processing such signals to extract desired information. In tomography, that would be the image, for example, of the conductivity distribution within the measuring space.

The data acquisition card used during the experiment was the National Instruments NI PCI-6070E card, which has the following specifications:

- 16 ADC inputs at up to 1.25 MS/s, 12 bits resolution
- 2 DAC outputs at up to 1.0 MS/s, 12 bits resolution
- 8 digital I/O lines

- 14 different analog input ranges

Figure 6.7 (A) shows a picture of the NI PCI-6070E (left) and the NI CB-68LP (right). NI CB-68LP is a connector block of the NI PCI-6070E. It has 68 screw terminals for easy input and output of wires. A shielded SH68-68-EP cable (see Figure 6.7 (B)) was used to link the data acquisition card and the connector block in our sampling system. The pin out of the PCI-6070E DAQ cards and the layout of the NI CB-68LP can be found in Appendix C.

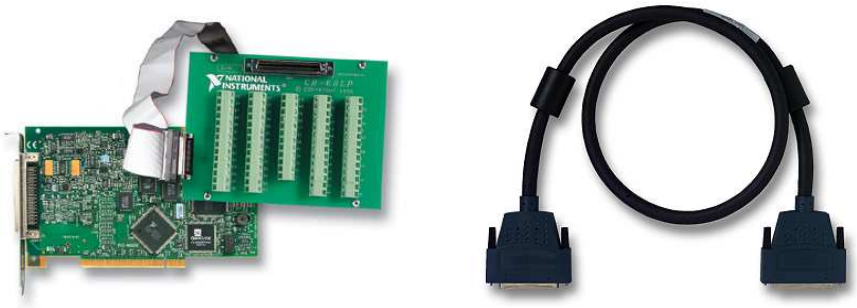

(A) (B)

Figure 6.7: (A) NI PCI-6070E data acquisition card and NI CB-68LP connector block, (B) Shielded SH68-68-EP cable (images from [60])

The NI PCI-6070E instrument card was controlled from a LINUX operating system using the open source COMEDI driver. COMEDI is an acronym for Control and Measurement Device Interface [61]. This is an open source project that includes a collection of drivers for data acquisition hardware. The included drivers were implemented as a core Linux kernel module, thus providing common functionality as their original driver modules. The instructions for installing the COMEDI library are given in Appendix D.

It has been shown above that the NI PCI-6070E only has 16 analog sampling channels, which are just sufficient for an eight channel tomography system, as each circuit board needs two sampling channels for I and Q signals. It might be a limitation in the future, though, if one wanted to increase the number of channels. Considering the need for future expansion, the Microchip dsPIC33FJ256GP710 micro-controller might be a good choice to perform the data acquisition. The dsPIC33FJ256GP710 has 32 ADC inputs with 10 bit, 1.1 MS/s or 12 bit, 500 kS/s conversion. Since the dsPIC33FJ256GP710 has already been implemented in the system for channels switching, it is always an advantage to utilise the micro-controller even more, in order to decrease the amount of system peripheral devices, and therefore minimise the system size. However, the dsPIC33FJ256GP710 may have a disadvantage: it has only one input sampling range, 0 V → supply voltage (generally +3.3 V or +5 V), whereas the NI PCI-6070E has 14 different input sampling ranges, which provides a much larger flexibility for our circuit design.

At this stage, a system level block diagram of our MIT instrumentation system can be illustrated in Figure 6.8.

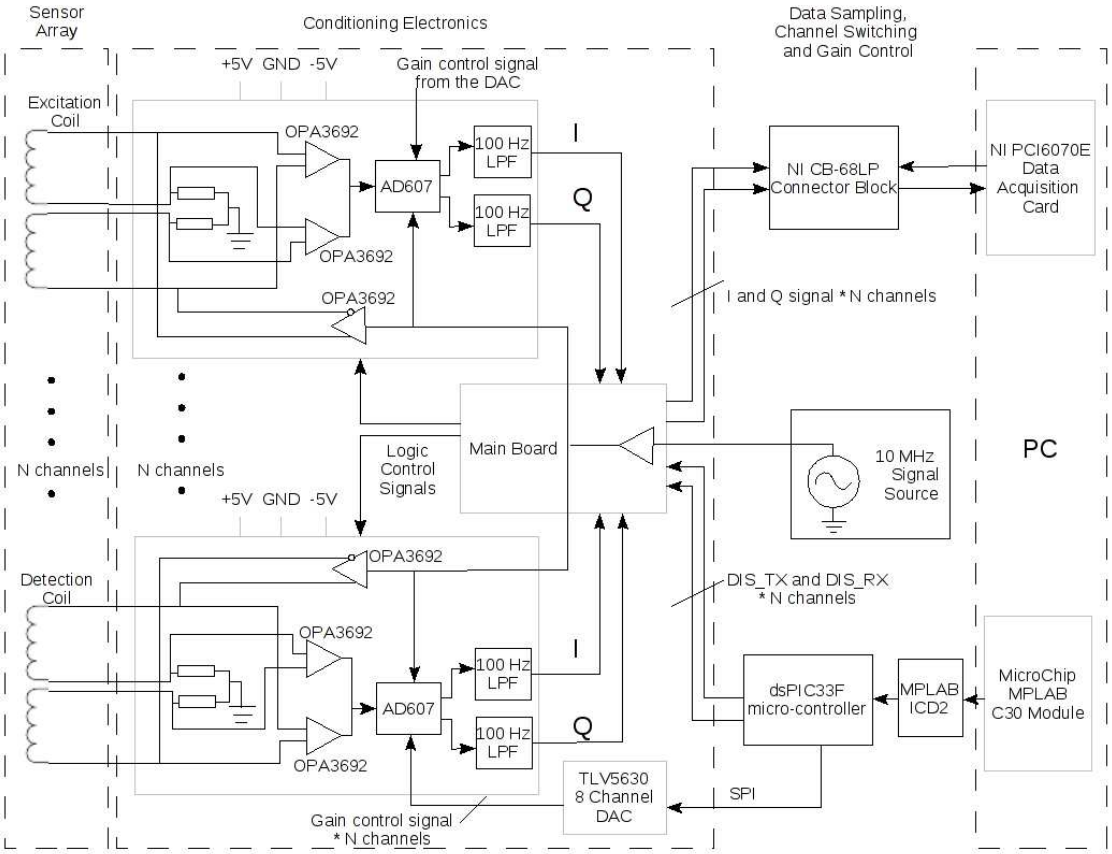

Figure 6.8: A complete system level block diagram of the MIT system.

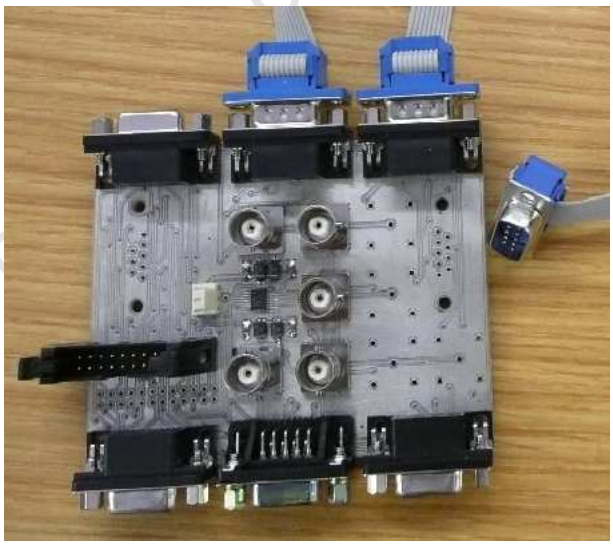

Figure 6.9: Main Board.

In our MIT system, a main switching board was constructed to ease the control and the examination of all the driving, switching and I/Q output signals, as illustrated in Figure 6.8. The main board contains an OPA3692 buffer, which is used to buffer the 10 MHz driving signal coming from the signal generator. The OPA3692's high output current (190 mA $\times$ 3 = 570 mA) makes it an ideal buffer to drive the coils in our multi-channel MIT system. All the I/Q output signals from the transceiver circuits are first connected to the

main board before fed into the CB-68LP connector blocks. All the channel switching signals (DIS_TX and DIS_RX) are also connected to the main board, then are linked to transceiver boards. A diagram of our designed main board is shown in Figure 6.9.

Chapter 7

Results

This chapter examines the performance of our designed MIT transceiver circuit and its suitability for detecting biological tissues and metallic objects. The performance is examined from four aspects:

- Noise characteristics
- Detectability of saline solution with different concentrations
- Detectability of metal with different conductivities
- Time stability

For the tests below, a three channel system was constructed. Each channel contained a transceiver circuit board and a 5+5 turns balanced coil, as shown in Figure 7.1. The coils were attached around a 20 cm diameter plastic former. The system setup is discussed in greater detail in the following section.

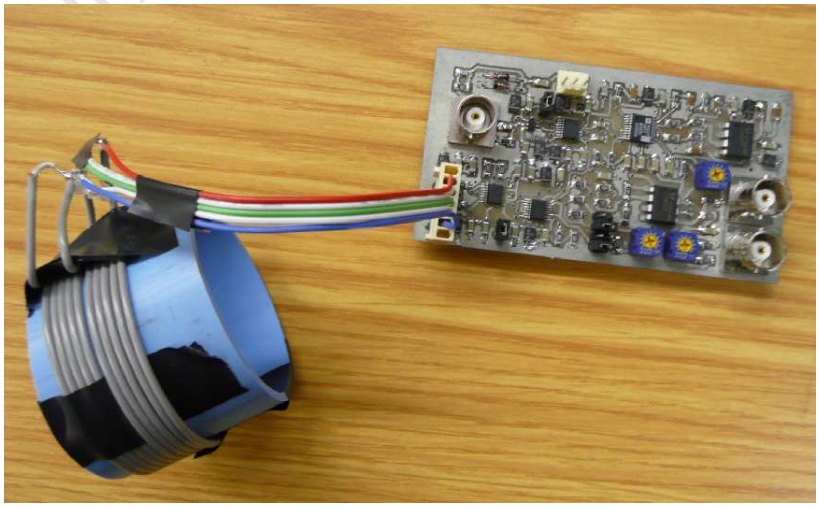

Figure 7.1: One channel of the MIT system.

7.1 System Setup

In order to verify the transceiver's performance, a three channel system was set up, with the sensor arrangement as shown in Figure 7.2.

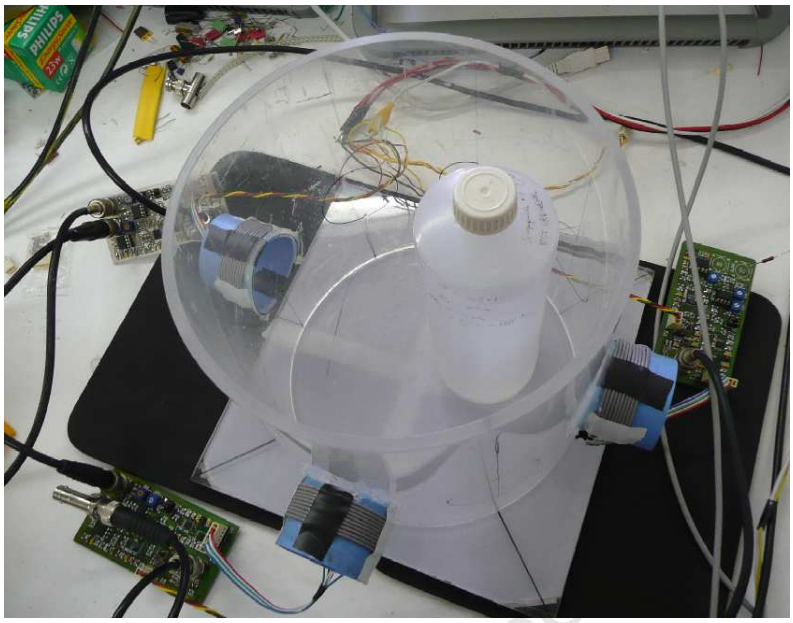

Figure 7.2: Perspex tube with the sensor coils attached.

As shown in the figure, the sensor coils were glued in place with a glue gun. Each sensor was then connected to a transceiver board, and the logic control signals applied to the board determined the behavior of the coil, i.e. whether it acted as a transmitter or a receiver. In this experiment, one transmitter and two receivers were constructed. The transmitter was attached at the left hand side of the tube, as shown in Figure 7.2. The first receiver was attached directly opposite to the transmitter (which is at the right in the figure), whereas the second receiver was attached around the tube but sitting between the transmitter and the receiver 1, at an equal distance from both of them (it appears at the bottom of the figure). No channel switching was involved in the experiments, as channel switching is only required when collecting a full tomography data set for image processing.

Two synchronised signal generators were used in the experiments. One signal generator supplied the driving signal to the transmitting coil, whereas the other signal generator supplied the reference signal to both receivers for I/Q demodulation. Since the signal generators were synchronised, we could adjust the magnitude of the driving signal and the phase difference between the transmitting signal and the reference signal, and therefore could verify the capability of magnitude and phase change measurement for I/Q demodulation. The simplified system's block diagram is shown in Figure 7.3.

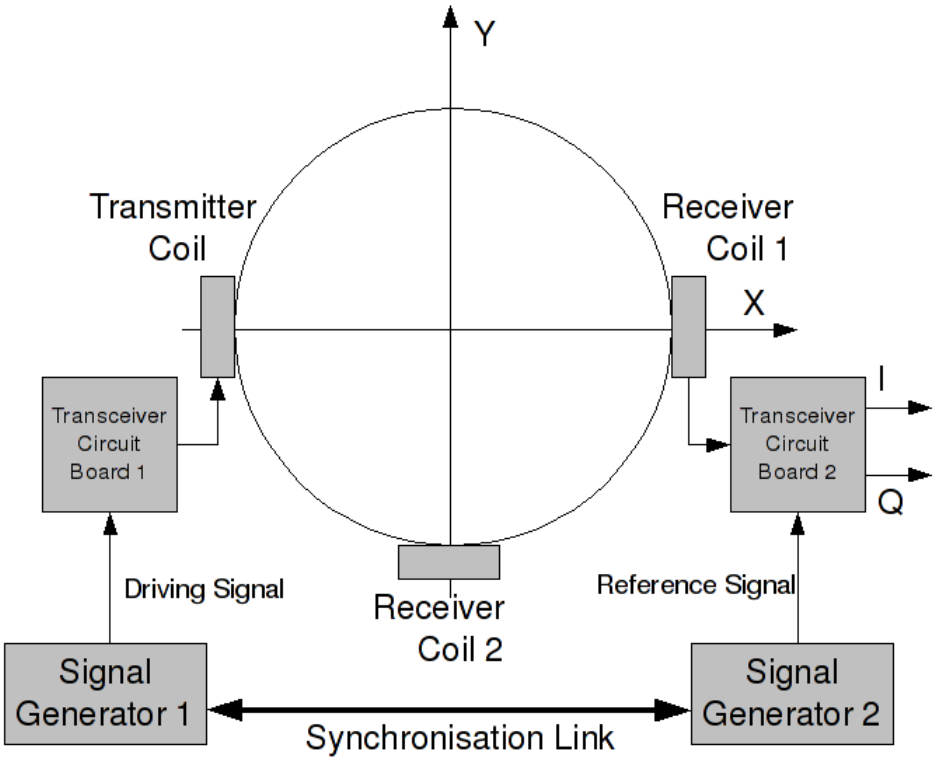

Figure 7.3: System block diagram of the initial experiment setup.

The I/Q outputs were first connected to the Agilent DSO3102A oscilloscope operating in x-y mode for visualisation, due to its simplicity. The I output channel was connected to Channel 1 (x-axis) and the Q channel was connected to Channel 2 (y-axis). This allows the oscilloscope display to show the tip of the phasor vector as in Figure 4.3. In the future MIT experiments, the NI PCI-6070E data acquisition card will be utilised for signal sampling.

7.2 Transceiver Board Testing

In this section, the performance of the transceiver board is examined. The experiments looked at three aspects: we wanted to determine the board's capability of measuring phase change, magnitude change (in receiving mode) and the driving current (in transmitting mode). For the phase and magnitude measurements, the phase and the magnitude of the driving signal were varied, and it was hypothesised that the sensor coil that was located directly opposite to the transmitting coil would be able to detect those changes. To measure the driving current, the transmitting coil was replaced by different values of resistors, and the amplitude of the output was then measured.

7.2.1 I/Q Demodulation Testing

Figure 7.4 shows the result of the phase change experiment on the transceiver circuit. In this experiment, the phase difference between the signal generator was changed from 0° to 180°, whereafter the I/Q output was examined. The driving signal was a 4 Vp-p, 10 MHz sinusoidal signal applied to the driving coil. The IF gain and the level shifter on the transceiver board were adjusted (≈ 250) so that the maximum I/Q outputs swing would be ± 2 V, and when the phase difference between the transmitting signal and the referencing signal was zero, the I and Q outputs would be sitting at +2 V and 0 V respectively, as shown in Figure 7.4 (B). Changing the phase by 180°, moved the point along the x-axis to location I = -2 V, Q = 0 V as expected (see Figure 7.4 (C)). Figure 7.4 (A) shows how the I channel changes as a function of time; the step from +2 V to -2 V is evident. Figure 7.4 (D) and 7.4 (E) shows the result when the phase difference was set to 45° and 135° respectively.

After varying the phase, the magnitude of the driving signal was also changed. An original 4 Vp-p driving signal was changed to 2 Vp-p, and the I/Q output result on receiver 1 is shown in Figure 7.5.

7.2.2 Checking the current measurement capability

To simplify the driving current measurement experiment, the driving coil was replaced by resistors, since the impedance value of the coil was hard to control. The driving signal, however, was still a 10 MHz, 4 Vp-p sine wave. Theoretically, the current flowing through the resistor should be directly proportional to 1/R, if the driving voltage was kept constant. In our designed circuit, the current signal was converted into voltage through a 1 Ω resistor, and the voltage signal was then passed through the OPA3692_RI, with a gain of two. The table and the figure below show the result of the driving current experiment: Table 7.1 shows the voltage measurement at the output of the OPA3692_RI, which was used to calculate the driving current, with respect to different resistor values, and Figure 7.6 shows the relationship between the predicted current flow and the measured current flow, the measurement with 39 Ω and 100 Ω are excluded in the figure, as those measurement values are much larger than the rest of the measurements and are therefore not appropriate to be placed into the figure.

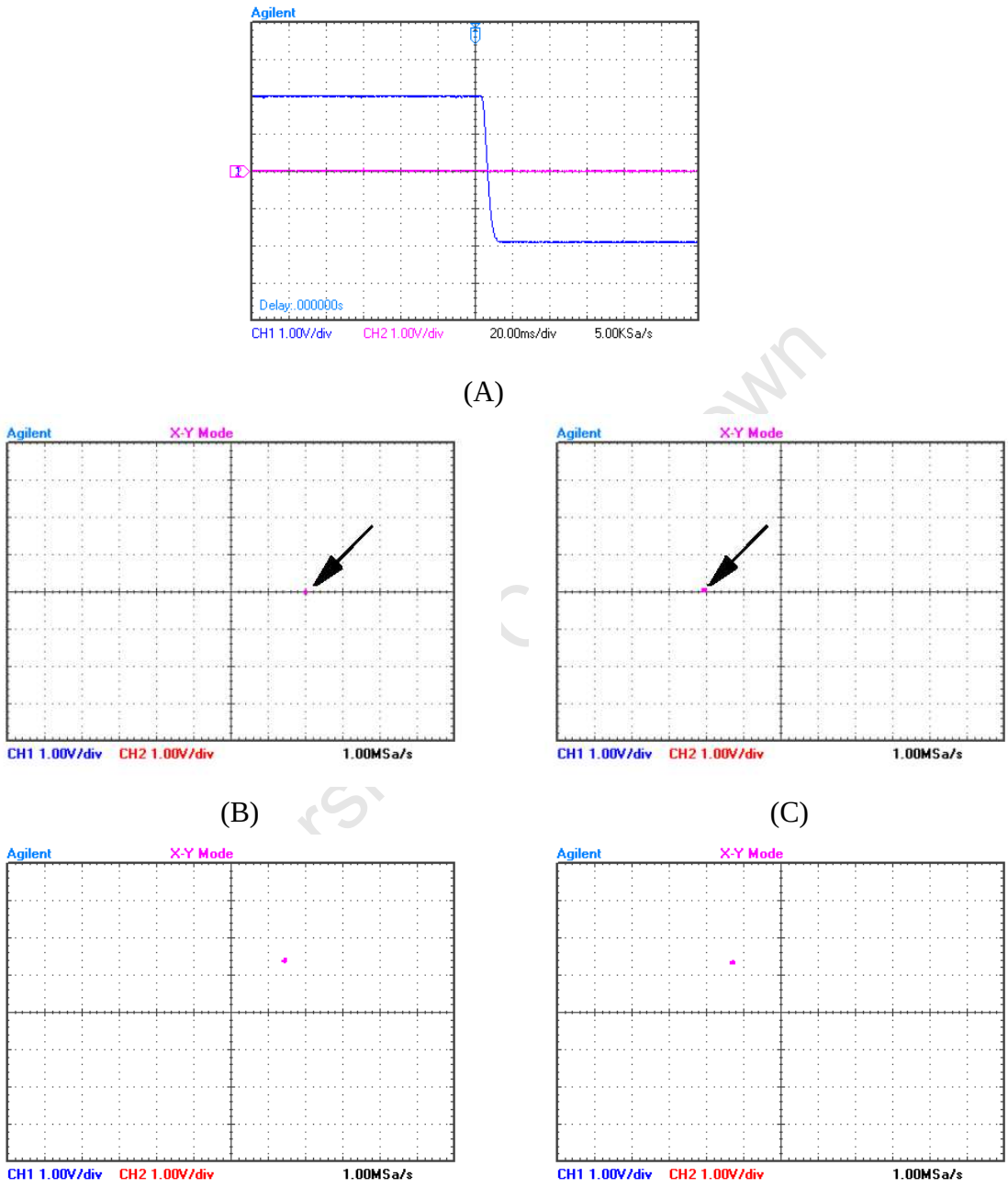

Figure 7.4: The changes of I/Q outputs in (A) Y-t mode and X-Y mode when the phase difference varies from (B) 0°to (C) 180°(D) 45° and (E) 135°.

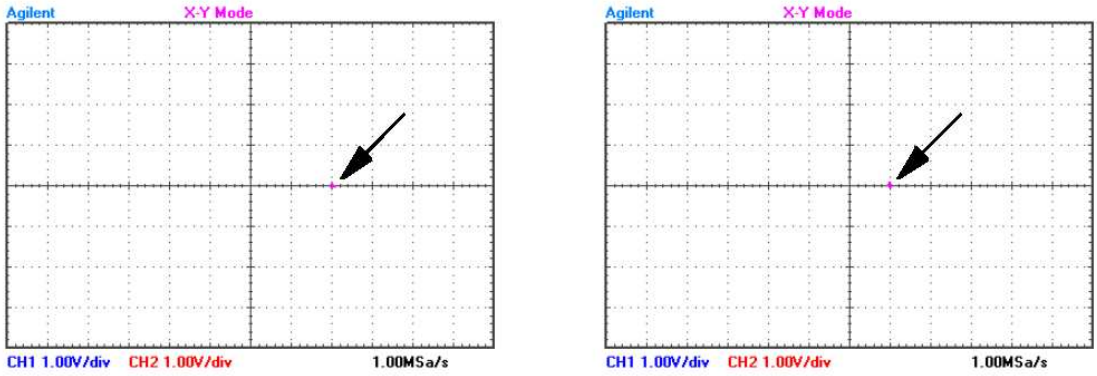

(A) (B)

Figure 7.5: The change of I/Q outputs in X-Y coordinates when the magnitude of driving signal changes from (A) 4 Vp-p to (B) 2 Vp-p.

		$\frac{4}{(R+1)} \times 1000$	sine wave	$\frac{V_{out}}{4} \times 1000$
R (Ω)	1/R	$I_{predicted}$(mA)	V_{out}(Vp-p)	$I_{measured}$(mA)
39	0.025641	100.0	0.37	92.5
100	0.010000	39.60	0.15	37.5
220	0.004545	18.10	0.078	19.5
240	0.004167	16.57	0.070	17.5
270	0.003704	14.76	0.063	15.75
360	0.002778	11.08	0.046	11.5
390	0.002564	10.23	0.043	10.63
470	0.002128	8.493	0.037	9.25
510	0.001961	7.828	0.034	8.5
560	0.001786	7.130	0.031	7.75
620	0.001613	6.441	0.029	7.25
680	0.001471	5.874	0.024	6.0
3900	0.000256	1.025	N/A	N/A
39000	0.000026	0.103	N/A	N/A
1 M	0.000001	0.004	N/A	N/A

Table 7.1: Results of the measured current flow with different resistor values.

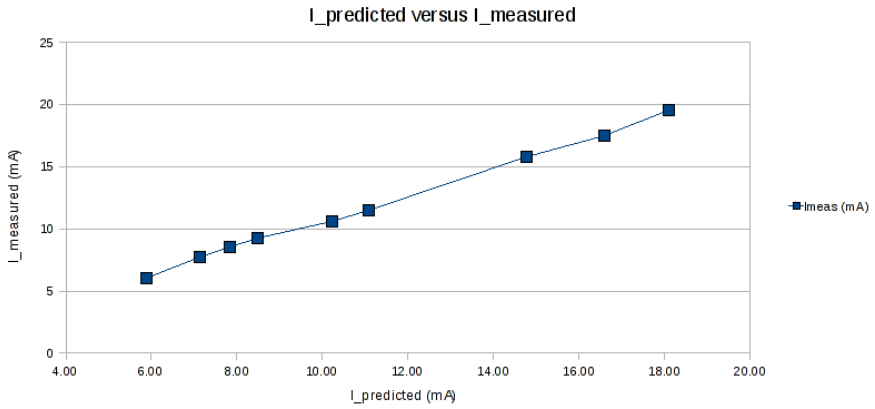

Figure 7.6: The predicted current flow versus the measured current flow.

It is clear from the Figure 7.6 that the transceiver is able to measure the phase change, the magnitude change and the driving current. When we varied the phase and the amplitude of the driving signal, the detector coil successfully picked up the change and represent the change correctly on the I/Q outputs. When the impedance of the sensor was varied, the changes in current's magnitude also obeyed the Ohms law, i.e. driving current $\propto$ 1/impedance. The results were very convincing, and we were thus more confident in using our designed transceiver in actual MIT systems.

For the rest of the experiments, the I/Q outputs of the transceiver board were sampled with the NI PCI-6070E card, as those samples needed to be stored for magnitude and phase calculations. The input sampling range for the NI PCI-6070E was set to ± 2.5 V, which allowed a fine resolution but also made sure that the sampling range was larger than the maximum output swing for the circuits, which was ± 2 V.

7.3 Noise Characteristics

Before running any MIT experiment, it is worth knowing how noisy the actual measurement the NI PCI-6070E DAQ samples is, since a noisy signal can lead to an erroneous result. In order to know the noise characteristics of the sampled data, the standard deviation of the sampled data must be calculated.

An estimate of standard deviation (*S.D.*) and the percentage deviation (*P.D.*) can be calculated using the following formulas:

$$S.D. = \sqrt{\frac{\sum (x_i - \mu)^2}{N-1}} \tag{7.1}$$

$$P.D. = \frac{\sigma}{\mu} \times 100$$

where σ is the estimated of standard deviation of the random process, x_i is the ith sample, μ is the mean of the samples in the sample set, and N is the number of total samples. Many programs contain built-in functions that can calculate the standard deviation easily; for instance, one can use the std() function in MATLAB and the stdev() function in the OpenOffice.org Spreadsheet program, which makes standard deviation calculation much quicker.

In order to obtain an accurate estimate of the standard deviation of the outputs, the data set that is used to calculate the standard deviation should contain sufficient independent samples; a few hundreds or more. The number of independent samples with a sampled waveform of length T seconds depends on the signal bandwidth. According to the Nyquist theory, if one takes samples at a frequency that is twice the signal bandwidth (Nyquist rate), then all the samples will be uncorrelated. In our case, the bandwidths of the I/Q outputs were approximately 100 Hz, and therefore the Nyquist frequency had to be 200 Hz, which gave us a time constant of 5 ms.

To obtain the data set for noise characteristics calculation, a driving channel and a detecting channel was set up (the transmitter and the receiver 1 in Figure 7.3). The driving signal was a 10 MHz, 4 Vp-p sinusoidal signal and an IF gain of approximately 275 was applied to the receiving signal, which gave us a ± 2 V I/Q output swing. The phase difference between the driving and the referencing signal was set to 45°, so the I and Q output would have the same DC value. For the data set shown in Figure 7.7, both I and Q outputs were sampled at 200 Hz for 5 seconds, which gave us 1000 independent samples. Figure 7.7 also shows the plot of the actual data set that we used to calculate the standard deviation.

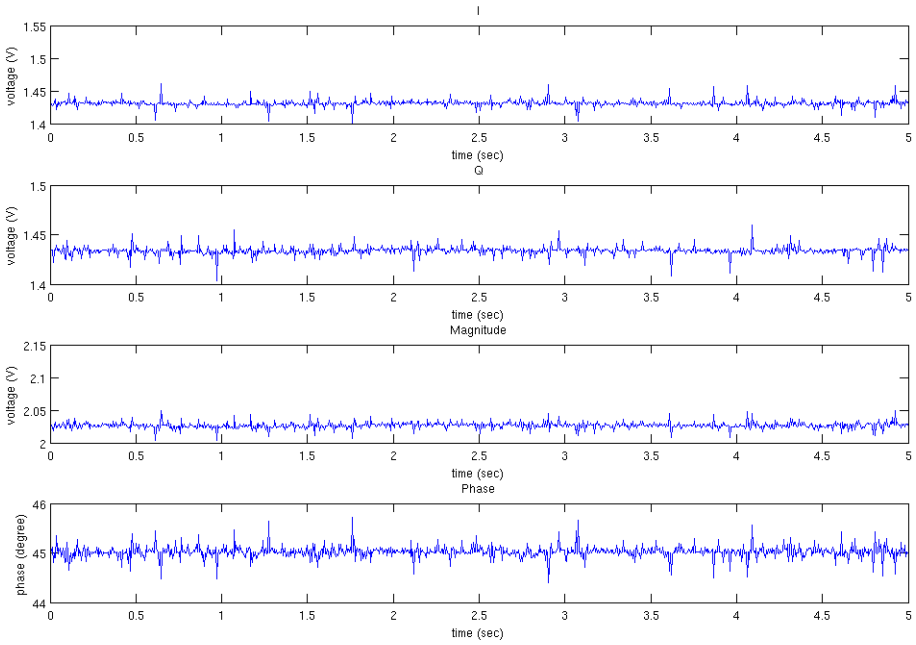

Figure 7.7: Uncorrelated I/Q outputs and the calculated phase and magnitude measurements.

One need to be aware that the sampled data shown in Figure 7.7 is a combination of the measurement circuit noise (in the I/Q waveform) and the noise from the NI-DAQ card. The circuit noise of the I/Q waveform can be estimated briefly by using the oscilloscope built-in RMS function. The standard deviation of the actual I/Q waveform was found out to be ≈ 1 mV.

From the collected data, the magnitude and the phase value could be calculated by using their corresponding I and Q. The standard deviations for the data set shown in Figure 7.7 were calculated as follows:

$$\text{I channel} = 0.0045 \text{ V } (P.D. = 0.31 \%)$$

$$\text{Q channel} = 0.0039 \text{ V } (P.D. = 0.27 \%)$$

Magnitude = 0.0044 V (*P.D.* = 0.22 %)

Phase = 0.11° (*P.D.* = 0.031 % of a cycle)

One can note that the NI-DAQ card added significant noise compared to the analog I/Q waveforms which are around 1 mV. The standard deviations for both I and Q outputs are around 5 mV and *P.D.* ≈ 0.30 %. It is still considered as acceptable for a MIT system [5]. Reducing the LPF's bandwidth can further reduce the standard deviation at the expense of the slower response time and frame rate at the output, i.e. standard deviation $\propto \sqrt{B}$ (for white noise), where B is the LPF's bandwidth. However, if the power spectrum density is $1/f$ (pink noise), then increasing bandwidth does not increase noise as severely as in the white noise case.

From this experiment, the short-term behavior of the system can also be concluded as stable . A good short-term stability represents that the system obtains a satisfactory phase drift relation for the quadrature signals generated by the AD607.

7.4 Measurement - Saline Solution

This section firstly discusses the saline detection ability of our MIT system, at a 10 MHz operating frequency, and thereafter, the operating frequency of the system will be changed to 3 MHz. A simple comparison test is then launch to prove that our MIT system can still work under 3 MHz, which is below the resonance frequency. Figure 7.8 shows the three channel experimental setup for measuring the saline solution that was carried out. Three different concentrations of saline solution were used in the experiment: 1 % by weight (0.48 S/m), 3 % (1.264 S/m) and 5 % (1.736 S/m). The conductivity of the saline solution was measured by the IONcheck 30 conductivity meter. An 8 cm diameter plastic bottle was used as the container of the solution, as shown in Figure 7.9.

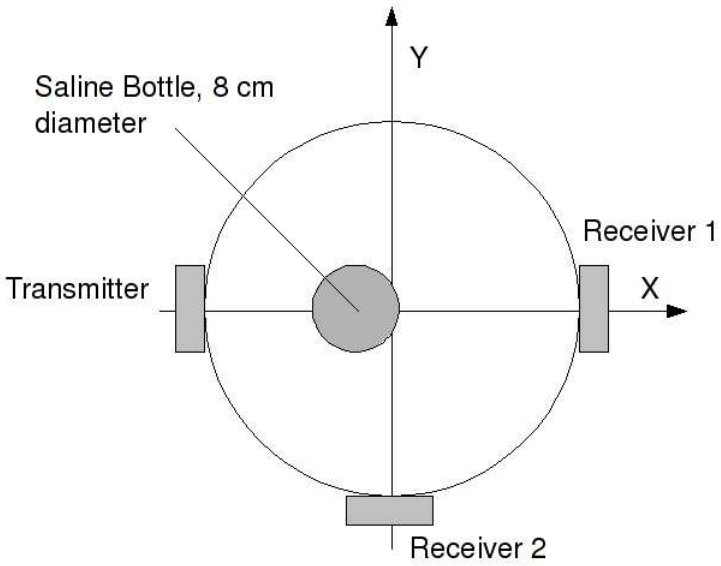

Figure 7.8: The system setup for the saline measurement.

Figure 7.9: Saline bottles.

In the experiment, one transmitting channel and two receiving channels were set up, as shown in Figure 7.8. The driving signal is still a 10 MHz, 4 Vp-p sinusoidal waveform. A gain of 275 and 21.4 were applied to receiver 1 and receiver 2 respectively. These gain values were selected to make the receivers' I and Q outputs swing between ± 2 V when the phase difference between the driving and referencing signal was varied from 0° to 360°, as discussed in Section 7.2.1.

The saline bottles were moved along the x-axis and the y-axis, as illustrated in Figure 7.8. The I and Q outputs for both receiver 1 and receiver 2 were connected to the NI PCI-6070E for data acquisition. For each position along the axes, 300 samples were captured

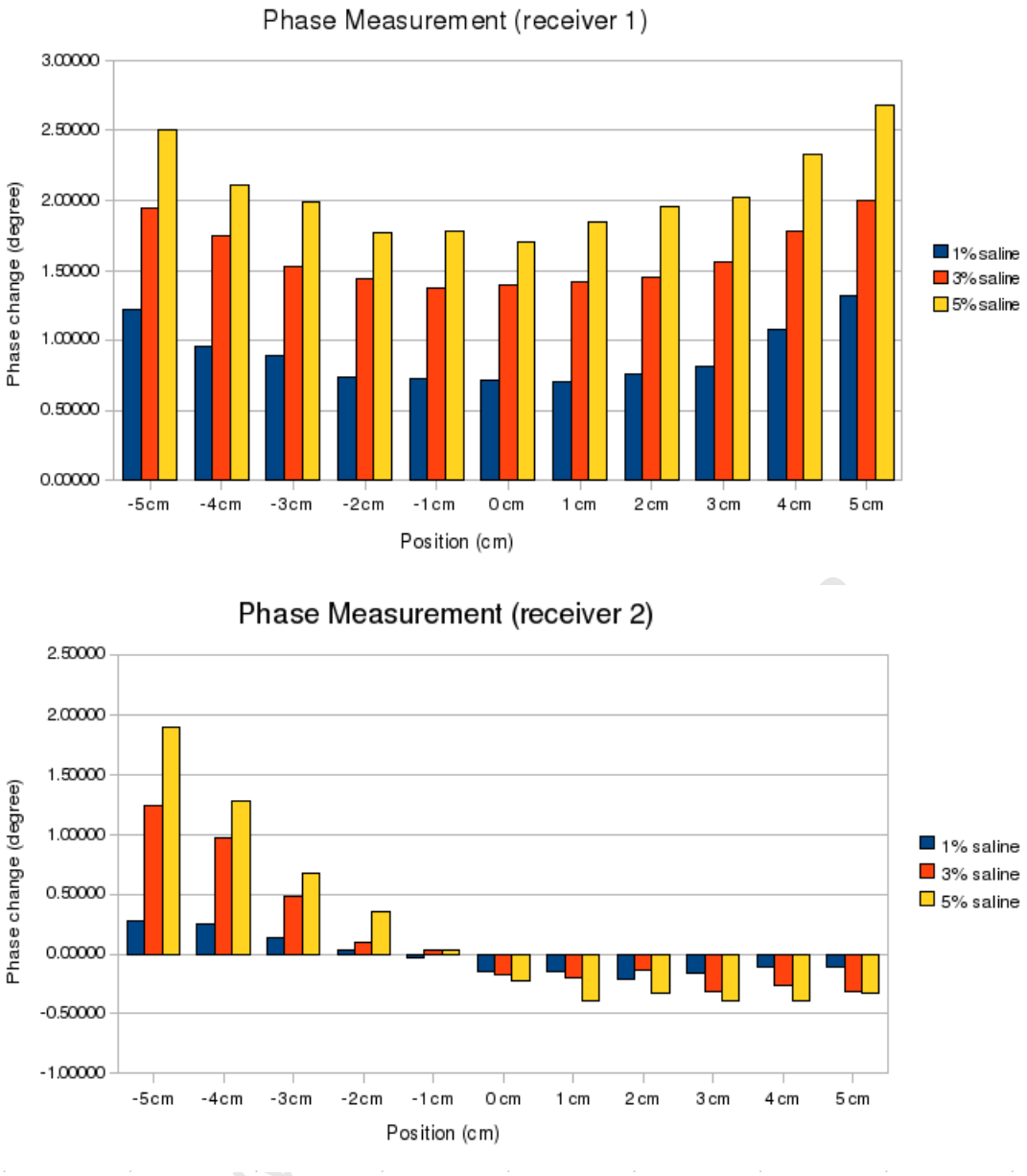

Figure 7.10: Phase change versus the saline bottle position along the x-axis.

in a rate of 75 kHz at each output. The average value and the standard deviation of those samples can then be calculated, and thereafter, a simple data processing was done to determine the magnitude and the phase change for both receiving coils. The standard deviation for the data set is approximately 6 mV. Figure 7.10 shows the phase change on both receivers when different saline bottles were at different positions along the x-axis, with cm displacement, relative to the center. Figure 7.11 shows the same results with the saline bottles moving along the y-axis. Figure 7.12 shows the comparison between the phase change and magnitude change when the 5 % saline bottle was moved along the y-axis.

As illustrated, the measured phase shifts were in direct proportion to the conductivity of the saline, and the magnitude change is relatively small compared to the phase change (see Figure7.12). This fact is in agreement with the theory of MIT and confirms the low

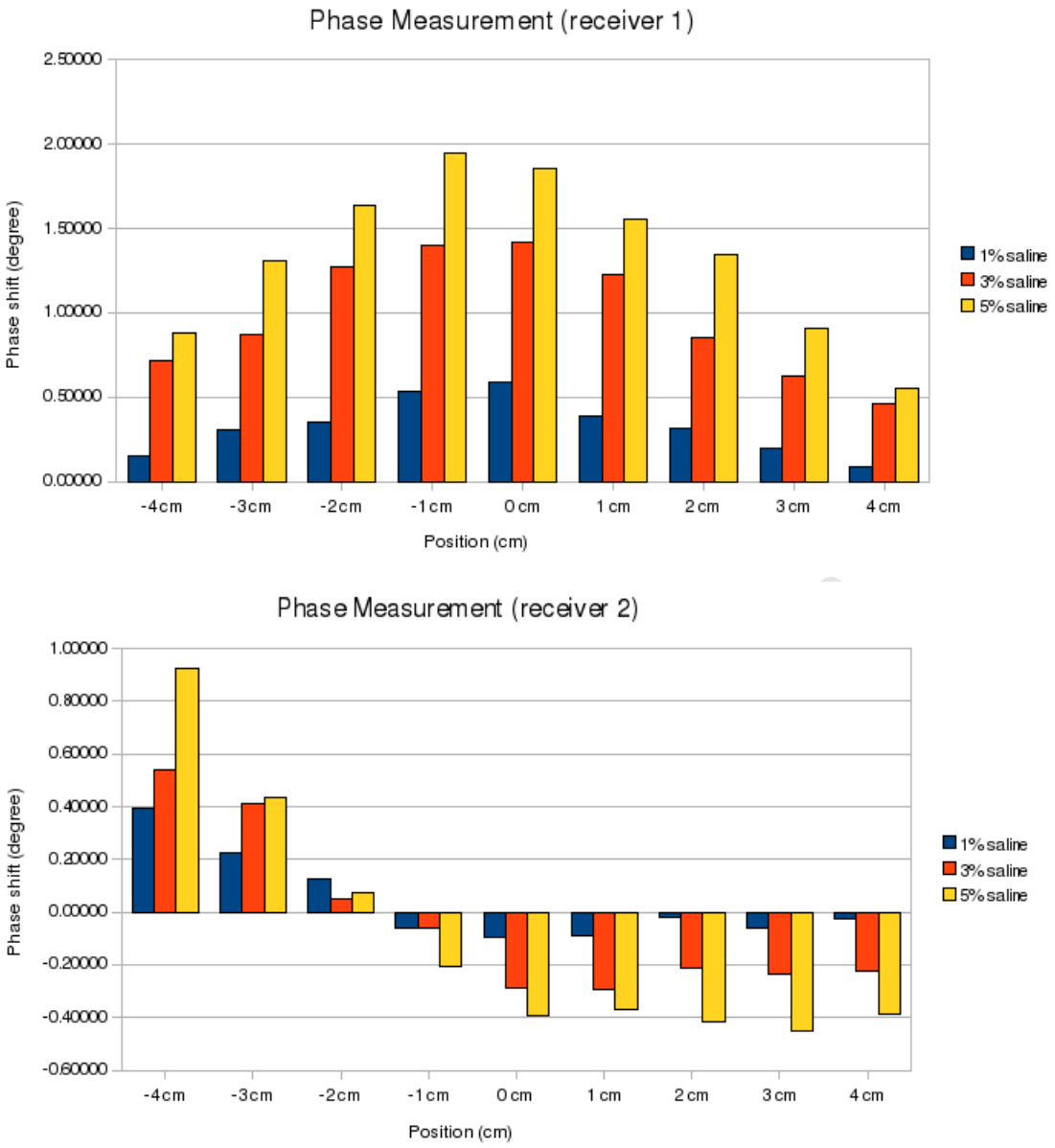

Figure 7.11: Phase change versus the saline bottle position along the y-axis.

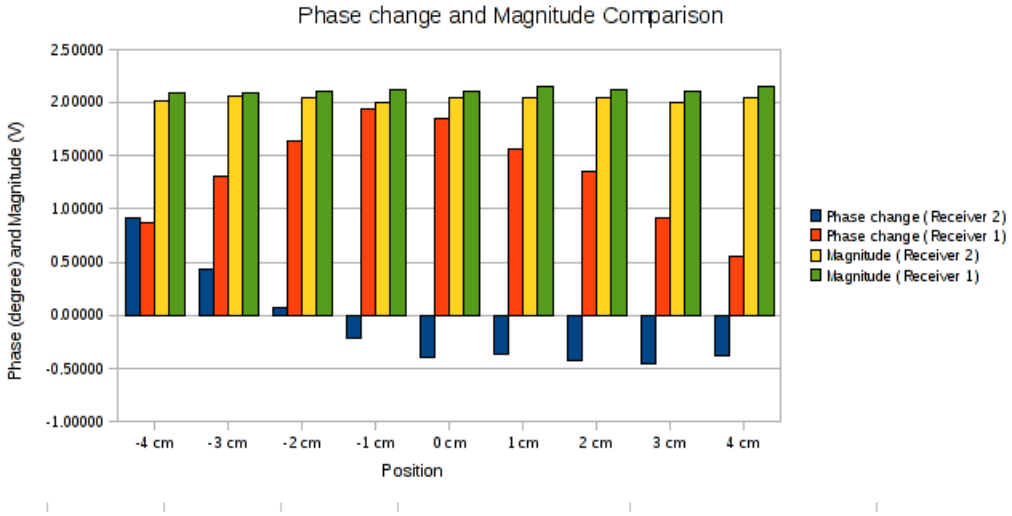

Figure 7.12: Phase change and magnitude measurement when the 5 % saline bottle is moved along the y-axis.

influence of the electric coupling between inductors and detectors. Although in some of the cases the phase change was not symmetrical and smooth with respect to the saline bottle's position, it is believed that this was due to human errors, such as sensor misalignment and position accuracy of the bottles.

The captured result was very similar to the result published in [11]. Their system setup was very similar to our own, except that the solution they used had a much higher conductivity (7 S/m and 3.5 S/m), which could have made the output phase change even more significant. Figure 7.13 shows theirs single channel measurement result for comparison, with the position of the receiver directly opposite to the transmitter.

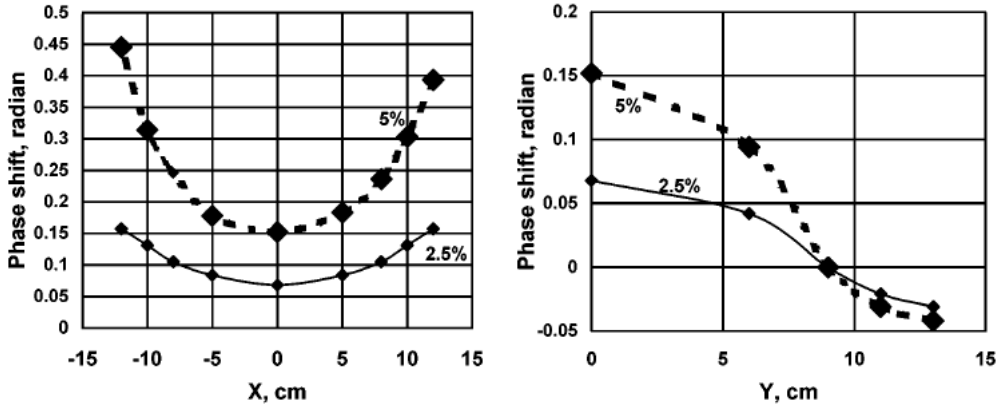

Figure 7.13: Measured phase shift as a function of position of the test object along the x-axis and the y-axis in the single channel measurements (graphs from [11]).

An experiment was also launched in this section, as we would like to see whether operating at a lower frequency would affect the system's ability to detect the phase change due to the presence of the saline bottle. In the experiment, one transmitting channel and one receiving channel were used, as described in Section 7.3. The driving signal's amplitude was still 4 Vp-p, but the frequency was changed to 3 MHz, which is below the coil resonance of 4.67 MHz. A gain of 34 dB was applied to the receiver 1 (much larger than the 10 MHz case) so the receiver's I and Q outputs would swing between ± 2 V when the phase difference, between the driving and referencing signal, was varied from 0° to 360°, as discussed in Section 7.2.1.

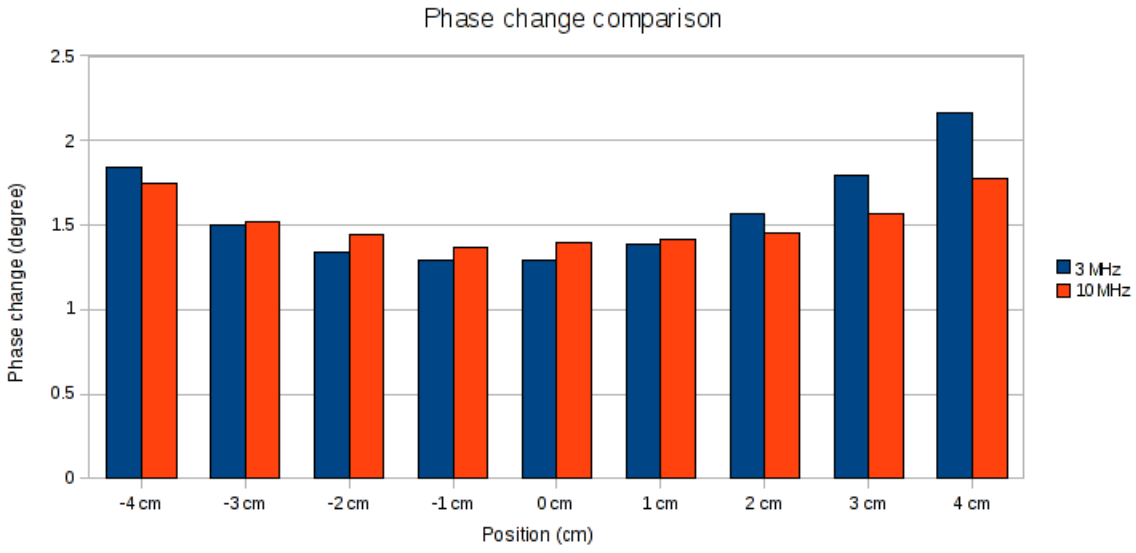

Figure 7.14: Phase measurement comparison when operating at 10 MHz and 3 MHz.

The 3 % saline bottle was moved along the x-axis, and the phase measurement was captured at each position along the axis by the data acquisition card. Figure 7.14 shows the phase changes when operating at 3 MHz and at 10 MHz. The 10 MHz measurements were taken in the previous experiment described above in the section. As shown in Figure 7.14, one can see that the system behaves in a similar way when operating at 3 MHz, i.e. the greatest phase change occurs when the saline bottle is closed to the transmitter and the receiver.

7.5 Measurement - Metal

Using the same 2 channel system setup, which is described in Section 7.3, a similar experiment was done using different types of metal sheets. Three different types of metal sheets were used: a thin aluminum sheet, a thick aluminum sheet and a thick steel sheet, as shown in Figure 7.15. All the sheets had the same dimensions (112 mm$\times$214 mm), but different thicknesses: the thin aluminum sheet: 0.5 mm; the thick steel sheet: 1 mm and the thick aluminum sheet: 2 mm. The characteristics of both aluminum and steel are shown in Table 7.2.

	Aluminum	Steel
Conductivity	37.8×10^6 S/m	$\approx10.41\times10^6$ S/m
Permeability	1.2566650 N/A^2	875 N/A^2

Table 7.2: Characteristics of aluminum and steel.

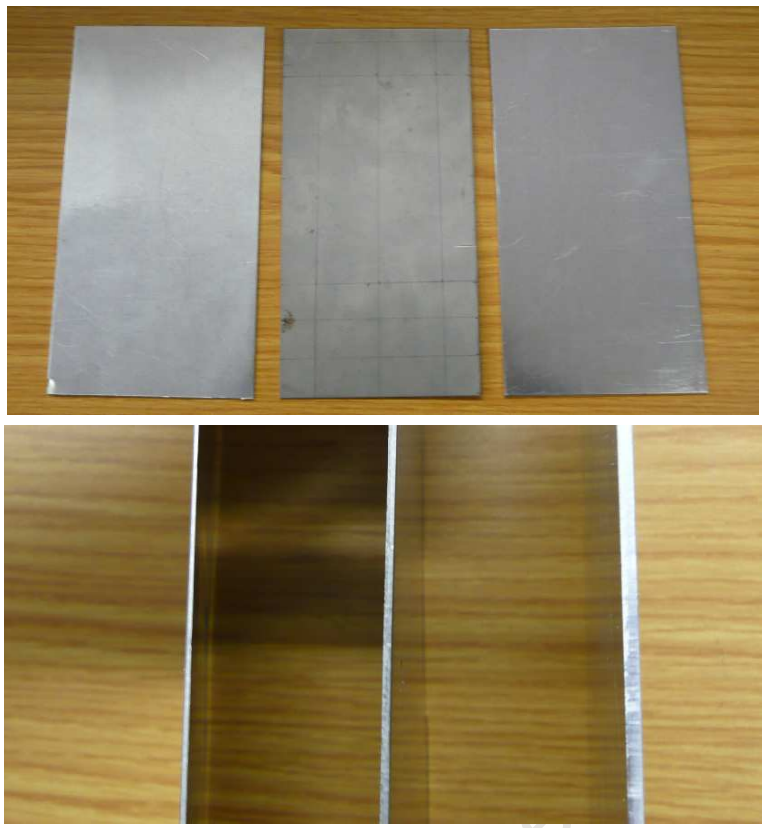

Figure 7.15: (Top, from left to right): A 0.5 mm thick aluminum sheet, a 1 mm thick steel sheet and a 2 mm thick aluminum sheet. (Bottom): Edge view of the metal sheets.

The exact conductivity for steel could not be found on the internet, as steel is an alloy consisting mostly of iron. One can see that both aluminum and steel have very high conductivities. However, there is a huge difference in permeability between these two materials. The aim of this experiment is therefore to find out whether our MIT is able to identify these two materials as well as the thickness of the sheets.

According to the literature, for the sample that has a high conductivity, due to the skin-depth and eddy current effect, the perturbation signal would mainly be a negative real signal, i.e. it should result in a decrease in magnitude at the sensor coil. Therefore, the phase change was not calculated in this experiment. In this experiment, a 4 Vp-p 10 MHz driving signal was applied to the driving coil. Each metal sheet was positioned along the x-axis, 300 samples (with a 75 kHz sampling frequency) for each I and Q output were captured by the NI PCI-6070E at every positions along the x-axis, with cm displacement relative to the center. The average of these 300 I and Q samples were then used to calculated the magnitude change. Figure 7.16 shows the magnitude change at receiver 1 when the metal sheets were moved along the x-axis.

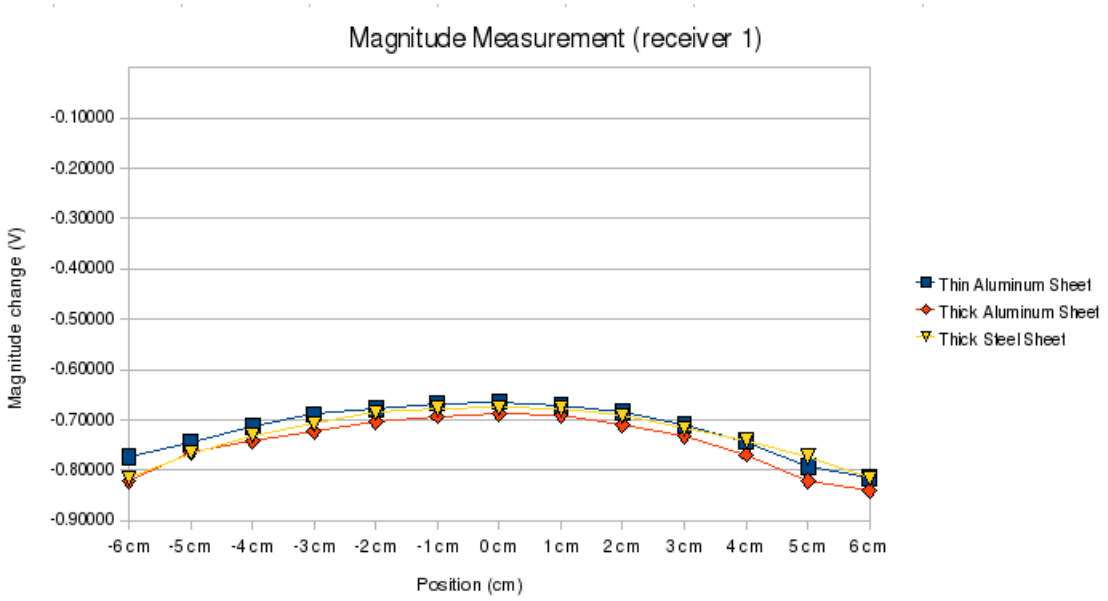

Figure 7.16: Magnitude change versus the metal sheet position along the x-axis.

The results show that the metallic objects do cause real negative signals on the receiver, and that the signal change is more significant when the metal sheet is close to the transmitter and the receiver. The results also show that the magnitude changes were very similar for all three metal sheets. However, the huge difference in permeability seemed to have no effect on the magnitude change. The skin depth effect is believed to be the reason of this. At 10 MHz, the skin depth of aluminum and iron are 1.84 μm and 0.17 μm respectively [Skin depth calculator: www.microwaves101.com/encyclopedia/calsdepth.cfm], which means there is only a small electromagnetic penetration into both metals. This could explain the observed similarity in all three metal sheets. This is maybe also the reason why most of the industrial MIT systems operate at low frequencies, as the difference between metals such as aluminum and iron is more easily detected at lower frequencies. Once the operation frequency is dropped to the point where the skin depth difference between aluminum and iron is large enough, the result shown in Figure 7.16 should be more distinguishable for different types of metal objects.

There were some slight differences in magnitude changes between the signals. This may be caused by the thickness of the metal sheet, as the thick aluminum sheet had the greatest thickness, which resulted in a slightly larger magnitude change. The thin aluminum sheet had the thinnest thickness, which caused the least magnitude change.

7.6 Stability

In MIT hardware, the small perturbations, which are caused by low conductivity objects, $\triangle$V need to be detected against a much larger background signal, V. As a result, the system's stability is an important parameter that determines the quality of the measurement. Stability is often divided into two categories: short-term stability and long-term stability.

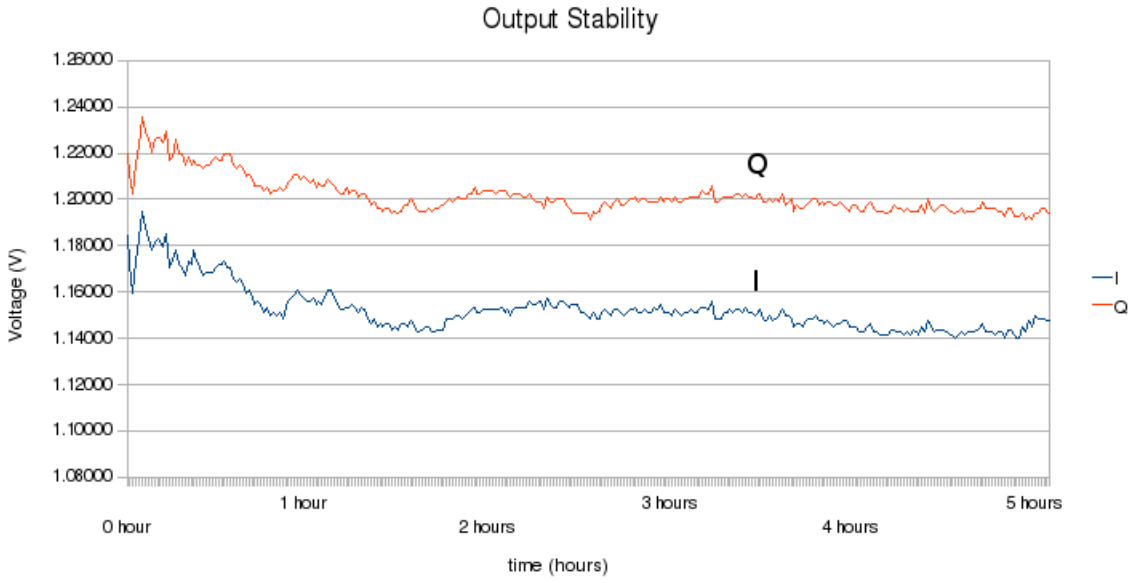

Figure 7.17: Output stability result: plot of I(t) and Q(t) over five hours.

Short-term stability is measured in the frequency domain as phase noise or phase drift, the observation interval is normally less than few seconds. It has been concluded from the result in section 7.3 that the short-term stability for our system is satisfactory.

The long-term stability is normally tied to the sensitivity to the environmental changes. In the section, we had to determine how long the transceiver took to reach a stable state once it was switched on. Before running the experiment, both signal generators had been warmed up for 2 hours to make sure the signal generators' stability would not affect the result.

In this experiment, the same two channel system setup was used, as described in previous section (or see Figure 7.3). The driving signal is still a 10 MHz, 4 Vp-p sine wave. A program was written for the NI PCI-6070E to take an average sample (1000 samples, 5 kHz) every minute automatically. As soon as the system was powered on, the program was executed. The stability test ran for five hours. The IF receiver gain and the phase difference were randomly chosen in this test, as this experiment only focused on the output stability of the circuits. All the other parameters such as the driving signal's magnitude and the phase were kept constant through out this experiment. Figure 7.17 shows the I/Q output drifting over the five hours.

It can be clearly seen that the I/Q outputs were quite unstable for the first 30 minutes, but they stabilised after the first hour. There was still a small signal variation ($\approx$15 mV) after the system had stabilised, however, this was considered to be the change of the environmental temperature. No attempt was made to stabilise temperature. It is believed that if the experiment was run inside a temperature-controlled room, the drift may be significantly smaller.

The stability test revealed that, in order to sample the most accurate outputs, the system had to be warmed up for at least 30 minutes before taking the actual tomography mea-

surement.

7.7 Phase Skew

The phase skew is defined as the variation of phase measurement when the input amplitude is changed, whilst keeping the true phase constant [33]. In this phase skew experiment, a two channel setup described in Section 7.3 was used, a 0° phase difference was set between the driving and the referencing signals (i.e. I = +2 V and Q = 0 V). The input amplitude of the 10 MHz driving signal was first set to a 4 Vp-p. A 100 mV decrement of the driving signal was then applied, and the outputs were measured again. This was repeated until the driving amplitude gradually decreased to 2 Vp-p. Table 7.3 shows the result of the phase skew measurement.

Driving amplitude	Phase	Driving amplitude	Phase
4.0 Vp-p	0.000°	2.9 Vp-p	0.360°
3.9 Vp-p	0.030°	2.8 Vp-p	0.313°
3.8 Vp-p	0.040°	2.7 Vp-p	0.352°
3.7 Vp-p	0.044°	2.6 Vp-p	0.377°
3.6 Vp-p	0.063°	2.5 Vp-p	0.380°
3.5 Vp-p	0.054°	2.4 Vp-p	0.441°
3.4 Vp-p	0.068°	2.3 Vp-p	0.458°
3.3 Vp-p	0.137°	2.2 Vp-p	0.469°
3.2 Vp-p	0.104°	2.1 Vp-p	0.437°
3.1 Vp-p	0.181°	2.0 Vp-p	0.472°
3.0 Vp-p	0.254°		

Table 7.3: Phase skew versus driving amplitude.

One can see from the result that, when the driving signal started to decrease, the 0° phase relation between the driving signal and the reference signal also started to deviate. When the driving signal decreased to 2.0 Vp-p, the amount of phase skew could go as high as 0.472°. Given that we were trying to measure a perturbation signal of less than 1° at times, this was considered as not acceptable.

The phase skew result shown in this section suggests that, once the startup calibration was completed, the amplitude of the input driving signal should not be varied anymore. As shown in Table 7.3, varying the input driving amplitude could influence the phase measurement significantly.

Chapter 8

Tomography Image Reconstruction

The demodulated signals that are sampled onto a PC need to be processed in order to retrieve a conductivity distribution image within the measuring space. Although the image reconstruction was not the focus of this project, a general image reconstruction algorithm for a tomography system was studied. This chapter briefly introduces about the concepts involved in the reconstruction of the tomography image.

8.1 General Algorithm

For an electrical tomography imaging system, two problems usually have to be solved, namely the forward and inverse problems [16].

- Forward Problem: Given the distribution of conductivity (or of the other passive electromagnetic properties) with boundary current density and voltage distribution, the aim is to solve for the voltage or current distribution on the electrodes around the measuring space [16]. In MIT, the differential forward model is expressed in term of Maxwell's equations, and solved numerically using a technique such as the finite element method (FEM).
- Inverse Problem: Given the voltage distribution (or current density), then solve for the distribution of conductivity (or the other passive electromagnetic properties). The inverse problem is sometimes also called the boundary value problem [16]. Inverse algorithm usually make use of the forward model as part of the solving process [62].

8.1.1 The Forward Problem

The first step of image reconstruction is to solve the forward problem. This is because in order to solve the inverse problem, one first needs to solve the forward problem for some assumed conductivity, so that the predicted voltage can be compared with the actual

measurement. Some numerical techniques like the finite element method (FEM) are used for solving the forward model [16, 62].

Let $Z = \frac{V}{I}$, where V is the induced voltage at the receiver coil and I is the driving current at the transmitter coil. Z is known as the trans-impedance (or mutual impedance) between the transmitter and the receiver. A change in the medium (i.e. change in σ, ε or μ) results in a change $\triangle Z$ in Z, and hence a voltage change $\triangle V = I\triangle Z$ at the receiving coil. The mutual impedance change $\triangle Z$ caused by the presence of the target within the measuring space can be equate as [62]:

$$\triangle Z = Z_b - Z_a = \frac{1}{I^2}\int_v j\omega(\mu_b - \mu_a)H_a \cdot H_b - (\sigma_b + j\omega\varepsilon_b - \sigma_a + j\omega\varepsilon_a)E_a \cdot E_b dv \quad (8.1)$$

Equation 8.1 is a generalised equation that can be applied to any pair of coils. Z_a is the mutual impedance between two coils when the medium properties are μ_a, ε_a and σ_a and an alternating current I with frequency ω is applied to one of the coil to produce the magnetic field H_a and the electric field E_a. Z_b is the mutual impedance when there is an object in the measuring space, with medium properties μ_b, ε_b and σ_b. H_b and E_b are the magnetic and electrical fields produced by the same coil when the same driving signal is applied to it [62].

For biomedical MIT systems, the equation can be simplified by ignoring permeability changes as the permeability of biological tissue is very similar to the permeability of air. The σ_a and ε_a parameters can also be ignored because, for most MIT systems, the measurements are made with respect to empty space. For this case, the conductivity of air, σ_a is 0 and the effect of permittivity, ε_a is negligible.

The equation now becomes

$$\triangle Z \approx -\frac{1}{I^2}\int_v (\sigma_b + j\omega\varepsilon_b)E_a \cdot E_b dv \quad (8.2)$$

Solving for voltage changes in the receiving coil then gives

$$\triangle V = I\triangle Z \approx -\frac{1}{I}\int_v (\sigma_b + j\omega\varepsilon_b)E_a \cdot E_b dv \quad (8.3)$$

In MIT systems, the direct electric field coupling is generally eliminated by all sort of screenings, therefore, when the sensing area is empty, the electric field is

$$E_a \approx -\frac{\partial A_a}{\partial t} = -j\omega A_a \quad (8.4)$$

where A_a is the magnetic vector potential within the sensing area, and the current density J_b inside the target is given by Ohm's law for the complex conductivity

$$J_b = (\sigma_b + j\omega\varepsilon_b)E_b \quad (8.5)$$

Substituting Equation 8.4 and 8.5 into 8.3 gives

$$\triangle V \approx \frac{j\omega}{I}\int_v A_a \cdot E_b(\sigma_b + j\omega\varepsilon_b)dv = \frac{j\omega}{I}\int_v A_a \cdot J_b dv \tag{8.6}$$

Equation 8.6 calculates the voltage changes across the receiver coil with respect to the voltage on the coil in the empty space. It is clear that σ_b and ε_b are the parameters that affect the voltage which appeared on the receiving coils. In Equation 8.6, I and ω are known in a current driven MIT system. The current density J_b and magnetic vector potential A_a need to be computed for the area covered by the volume of integration in order to solve the forward problem, however, in different conditions. The A_a field is calculated for the empty space and will not be affected even if a target is presented in the measuring space. Therefore A_a is only related to the geometry of the system, the driving current and its frequency, and it only requires to be computed once. The J_b is calculated with the presence of the target, or the induced eddy current on the target. Therefore it is related to the conductivity distribution of the object and must be re-calculated each time when the conductivity is changed.

The forward model is solved either for the purposes of sensitivity computation or for implementing a nonlinear iterative reconstruction algorithm, such as Gauss Newton Method [16].

8.1.2 Inverse Problem

The inverse problem is typically carried out by minimising a cost function, i.e. the error function between the measured values and the predicted values [16]:

$$\Phi(\sigma,\varepsilon) = (f(\sigma,\varepsilon) - \triangle V_0)^T (f(\sigma,\varepsilon) - \triangle V_0) \tag{8.7}$$

where Φ is the error function; σ and ε are the conductivity and permittivity distribution; $f(\sigma,\varepsilon)$ is the estimated voltage and $\triangle V_0$ is the change of measured voltage. To minimise Φ, one needs to take the derivative and equate it to zero,

$$\Phi'(\sigma,\varepsilon) = (f'(\sigma,\varepsilon))^T (f(\sigma,\varepsilon) - \triangle V_0) = 0 \tag{8.8}$$

where $f'(\sigma,\varepsilon)$ is the Jacobian matrix and is made up of the partial derivatives of f, the calculated voltage, with respect to the conductivity and permittivity distribution (i.e. the result from the forward model).

The Gauss Newton Method [16] is an iterative reconstruction algorithm specifically developed for non-linear problems, which can solve the inverse problem in an indirect way: It compares the voltage responses of the conductivity distribution (from forward model) with the actual measured response. If the error function is larger than the threshold, the σ and ε will be adjusted by $\triangle\sigma$ and $\triangle\varepsilon$. The adjusted value can be calculated by expressing the Taylor polynomial of $\Phi'(\sigma,\varepsilon)$. If the voltage responses of the assumed conductivity distribution match the real distribution, it can be claimed that the assumed distribution is

the answer of the inverse problem. Figure 8.1 shows the flow chart of the implementation of the Gauss Newton Method.

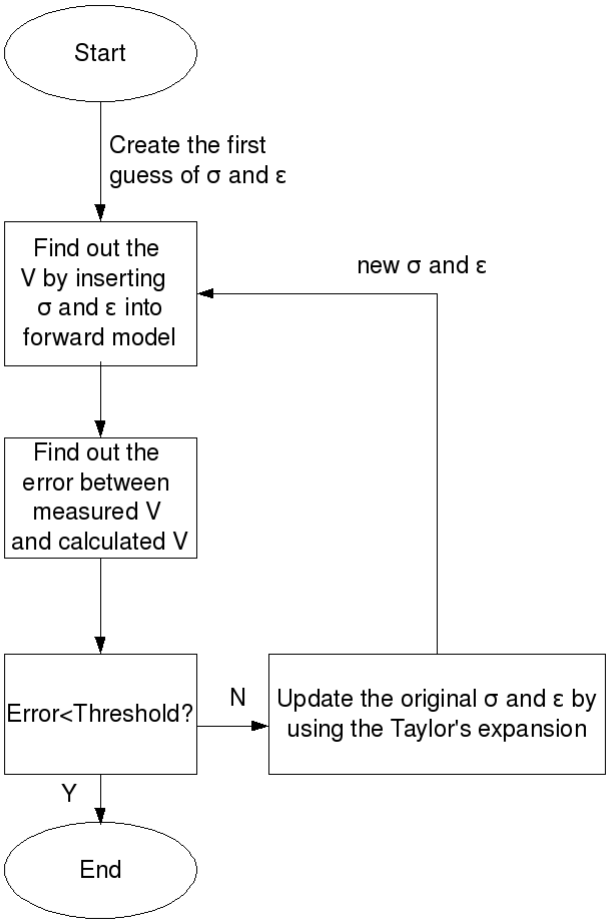

Figure 8.1: Flow chart of the Gauss Newton Method.

The spatial resolution of the conductivity image is primarily determined by the number of sensors used in a tomography system. The data capturing procedure is a sequential process: if there are N coils in total, we will drive coil 1 and take the measurements from coil 2 to coil N. Then we drive coil 2 and measure from coil 3 to coil N and also coil 1; the same procedure is repeated until we reach the Nth coil. In that case, the number of measurements taken from a N channel system will be $N(N-1)$. However, since most of the geometry of tomography systems is symmetrical, the measurement taken from coil 1 when driving coil 2 will be the same as the measurement taken from coil 2 when coil 1 is driven. This will further reduce the number of independent measurements for a N channel system to $N(N-1)/2$. For example, for an eight channel MIT system, the number of independent measurement will be $8 \times (8-1)/2 = 28$, if the self trans-impedance measurements are excluded. Therefore, we can only determine a number of conductivity values less than or equal to 28.

In practice, some algorithms [63, 64] solve for more unknowns (σ and ε values) than the

number of independent measurements. These algorithms however introduce a smoothing constraint (or regularisation) on the solution. Examples of these kinds of images obtain using such method are shown in Figure and in Chapter 2.

Chapter 9

Conclusion and Recommendations

The measurement electronics for a multi-channel MIT data acquisition system has been developed in this project. In the past, metal detection has always been the major application for the sensor coils [52], due to their high sensitivity to the high conductivity materials. However, from the results presented in Chapter 7, we were able to develop a MIT system that is not only sensitive to high conductivity objects such as metal, but that also has the ability to measure the tiny signal alteration caused by low conductivity materials. Different concentrations of salt water (i.e. different conductivity) could also be identified clearly from the output of our MIT circuits. These encouraging results suggest that it is possible to create a functional biomedical MIT system using our hardware.

Table 9.1 summarises the circuit characteristics from the experiments in Chapter 7.

	Value	**Condition**
Noise characteristics	≈5 mV deviation for both I and Q channels	200 Hz sampling rate in 5 seconds (i.e. 1000 samples) Post demodulator's bandwidth = 100 Hz
Settling time	≈ 1 hour after switching on the system	After 1 hour, the fluctuation is less than 20 mV over subsequent 5 hours (see Figure 7.17)
Phase skew	≈+0.02° /100mV increment	driving signal varies from 2 Vp-p to 4 Vp-p
Quadrature Phase Accuracy (Inside AD607)	-1 degree [56]	Operating frequency is at 10.7 MHz. However, the phase mismatch problem can be compensated by using the software calibration

Table 9.1: Characteristics of the transceiver circuits.

For the transceiver circuit, the bandwidth of the output filters determines the image capture rate, which is a key performance criterion for a tomography system. In our transceiver circuit, the bandwidth of the low pass filter was set to a low value (100 Hz) in order to minimise the noise, but this also limited the rate of change of the output. For a 100 Hz bandwidth, its settling time can be $5\times\frac{1}{B}$ (≈50 ms), if an eight channel system was constructed, the image refresh rate would be roughly two frames per second. This is a relatively slow image refresh rate compared to other published electrical tomography systems. In the future, if one wanted to increase the image update rate, the bandwidth of the output LPF would have to be adjusted. Increasing the output bandwidth would definitely affect the

noise performance; however, because of the pink noise's $1/f$ characteristics[1], the noise level might not be worsened by such a big factor.

The project has confirmed the theory given in other publications on MIT. The future focus of this project will be:

- to increase the number of channels for our current MIT system (if the NI PCI-6070E DAQ is used for the data acquisition, a maximum of 8 channels can be used, due to the limited amount of sampling channels. However, in the future, if we decide to replace the NI_DAQ with the dsPIC33FJ256GP710 microcontroller, the number of channels for our MIT system can be extended to 16);
- to develop another 10 MHz signal source, in a digital approach (programming a DDS chip) or in an analog approach (constructing a LC crystal oscillator), to replace the laboratory signal generators. This can significantly improve the portability of our MIT system;
- to determine the optimum number of coil turns for operation at 10 MHz. It is perhaps better to operate the coil below resonance in the region where the physical coil behaves more like an ideal inductor, which is assumed in the forward model;
- to find out the possibility of using a PCB coil instead of a hand-wound coil. PCB coils are easy to reproduce and can give us an accurate rigid construction, which might decrease the amount of software calibration during the image reconstruction stage;
- and finally, to investigate and implement the image reconstruction algorithm for MIT, which is discussed in Chapter 8, i.e. solving the forward model and the inverse problem. There are several journal papers which discusses the MIT image reconstruction process, the topics include implementing FEM, solving the inverse problem and the sensitivity map computation [63, 65, 66, 67, 68, 64, 69].

[1]Pink noise is a type of noise that has a power spectrum density which is proportional to the reciprocal of the frequency, i.e. pink noise's power density = $1/f$. Therefore, increasing the bandwidth may not worsen the noise severely, but it can improve the frame update rate significantly.

Appendix A

Mathematical Model for MIT system

This chapter shows the derivation of a mathematical model of a simple two channel MIT system, which was previously mentioned in Section 2.1.2. The mathematical derivation was derived from [23] and [25].

Consider a circular disk of radius R and thickness t, placed co-axially and centrally between a transmitting coil and a receiving coil, as shown in Figure A.1. The coils are distance $2a$ apart. The circular disk has conductivity σ and permeability μ_0, i.e. it is non-ferromagnetic. The skin depth δ is assumed to be much greater than t, which means that the attenuation produced by the disk is small.

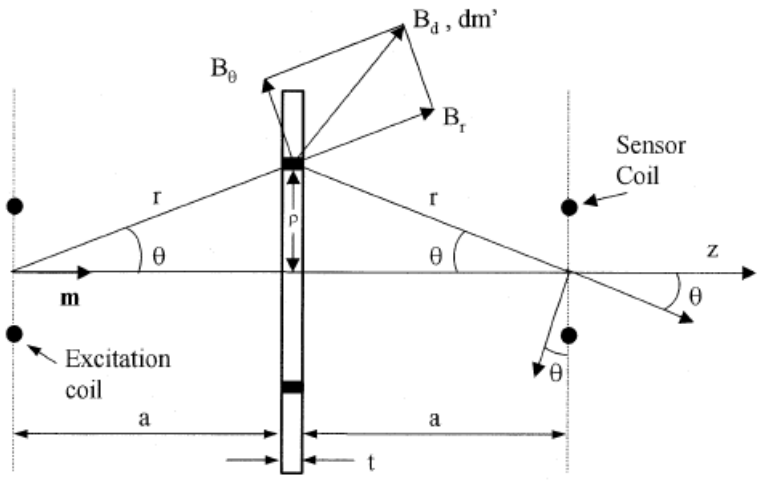

Figure A.1: Model of the electromagnetic coupling between a cylindrical sample and a two coil system (illustration from [25]).

At point P of the disk, the magnetic B-field has components (in polar co-ordinates)

$$B_r = \frac{\mu_0 m}{4\pi r^3} 2\cos\theta \tag{A.1}$$

$$B_\theta = \frac{\mu_0 m}{4\pi r^3} \sin\theta \tag{A.2}$$

where m is the equivalent magnetic dipole moment of the coil. The field along the z-axis is then

$$B_z = \frac{\mu_0 m}{4\pi r^3}\left(2\cos^2\theta - \sin^2\theta\right) = \frac{\mu_0 m}{4\pi r^3}\left[\frac{2a^2-\rho^2}{\left(a^2+\rho^2\right)^{5/2}}\right] \tag{A.3}$$

Hence, the flux threading a circular path of radius ρ centered on the axis is

$$\Phi = \int_0^{\rho} B_z(\rho')2\pi\rho' d\rho' \tag{A.4}$$

which is readily shown to be

$$\frac{\mu_0 m}{2}\left[\frac{\rho^2}{\left(a^2+\rho^2\right)^{3/2}}\right] \tag{A.5}$$

The induced voltage around this path is $-j\omega\Phi$, which is also equal to the line integral $2\pi\rho E_\phi$ of the induced electric field. The current density is given by $J = \sigma E$, so

$$J_\phi = \frac{-j\omega\sigma\mu_0 m}{4\pi}\frac{\rho}{\left(a^2+\rho^2\right)^{3/2}} = \frac{-jm}{2\pi\delta^2}\frac{\rho}{\left(a^2+\rho^2\right)^{3/2}} \tag{A.6}$$

where δ is the skin depth $(2/\omega\mu\sigma)^{1/2}$. Consider now a thin annulus of the disk, between ρ and $\rho + d\rho$. The current it caries is

$$dI = J_\phi t d\rho = \frac{-jmt}{2\pi\delta^2}\frac{\rho}{\left(a^2+\rho^2\right)^{3/2}}d\rho \tag{A.7}$$

The field produced by this induced current at the sensing coil is given by the usual formula for a single turn circular coil:

$$dB = \frac{\mu_0\rho^2 di}{2\left(a^2+\rho^2\right)^{3/2}} = \frac{-j\mu_0 mt}{4\pi\delta^2}\frac{\rho^3}{\left(a^2+\rho^2\right)^{3/2}}d\rho \tag{A.8}$$

Now, the field at the sensing coil due to the excitation coil is $B = \mu_0 m/(16\pi a^3)$,so

$$\frac{dB}{B} = \frac{-4jta}{\delta^2}\frac{\rho^3}{\left(a^2+\rho^2\right)^3}d\rho \tag{A.9}$$

The total field $\triangle B$ due to the induced currents in the entire disk is found by integrating this equation which gives

$$\frac{\triangle B}{B} = \frac{-jta^3}{\delta^2}\left[\frac{1}{a^2} - \frac{a^2+2R^2}{(a^2+R^2)^2}\right] = -jta^3\frac{\omega\mu_0\sigma}{2}\left[\frac{1}{a^2} - \frac{a^2+2R^2}{(a^2+R^2)^2}\right] \tag{A.10}$$

If the disk has significant relative permittivity ε_r, the imaginary term $j\omega\varepsilon_0\varepsilon_r$ must be added to the conductivity in the expression for δ, which gives finally

$$\frac{\triangle B}{B} = \left(\frac{ta^3\omega\mu_0}{2}\right)(\omega\varepsilon_0\varepsilon_r - j\sigma)\left[\frac{1}{a^2} - \frac{a^2+2R^2}{(a^2+R^2)^2}\right] \tag{A.11}$$

where ε_0 is the permittivity of free space.

In [25], Equation A.11 is modified so the relative permeability is taken into consideration, an extra term is introduced in the equation:

$$\frac{\Delta B}{B} = \frac{ta^3}{2}\left\{\chi_m\frac{R^2(8a^2-R^2)}{(a^2+R^2)^4} + (\omega\varepsilon_0\varepsilon_r - j\sigma)\omega\mu_0\left[\frac{1}{a^2} - \frac{a^2+2R^2}{(a^2+R^2)^2}\right]\right\} \tag{A.12}$$

where $\chi_m = \mu_r - 1$, which represents the magnetic susceptibility of the material. The derivation of the extra term in Equation A.12 can be found in [70]. One should be noted that the Equation A.12 is valid only in the case of 'weak perturbation,' i.e., if the alteration of the excitation field by the sensing material is negligible and if μ_r is close to 1. This is the case for biological objects (conductivity < 2 S/m) up to several MHz.

Appendix B

High Speed PCB Layout Guide

In our tomography system design, there are several high speed ICs involved in the circuitry, such as the OPA3692, the ADG601 and the AD607. In order to achieve the optimum system performance, a careful PCB layout and external components selection were required. Although this topic is too large to be covered in appendix, this appendix summarises some general recommendations that were used to optimise the high speed circuit performance. The content of this appendix comes mainly from papers [71, 72].

B.1 Decoupling of Power Supplies

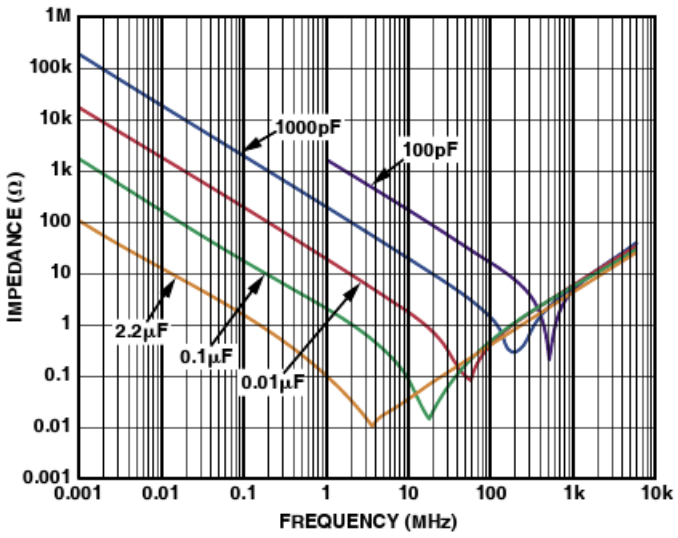

Figure B.1: AC impedance versus frequency with different capacitor values (graph from [71]).

Every power supply signal that goes into high speed PCB circuitry must be carefully bypassed ('decoupled') to its ground return to prevent noise from entering into the circuit. Capacitors are used to let the power supply pins see a low AC impedance to the ground.

Different capacitor values have different AC impedances at different frequencies. Figure B.1 shows the relationship between the capacitor impedance and the frequency for different capacitor values. By placing multiple capacitors in parallel across the supply, a low impedance over a wide frequency range can be achieved. The figure shows the importance of connecting multiple capacitors: when one capacitor's frequency response is rolling off, the other capacitor starts to dominate. Therefore paralleling capacitors with different values ensures that the power supply pins see a low AC impedance across a wide range of frequencies.

Generally, two parallel capacitors are sufficient to maintain a low AC impedance for several decades of frequency. Small value ceramic capacitors (0.01 to 0.1 μF) are used to eliminate the high frequency noise, and the distance from the power supply pins to the capacitors should be as short as possible. Larger tantalum capacitors of 3 to 20 μF, effective at lower frequency, should also be used on the supply pins to keep the low frequency ripple off the circuit. These capacitors may be placed somewhere farther from the power supply pin and may be shared among several devices in the same area of the PCB.

B.2 System Grounding

A ground plane acts as a common reference voltage, providing shielding, dissipating heat, and reducing stray inductance. However it also increases the parasitic capacitance. Attention needs to be paid when laying out the ground plane, because there are some situations which can worsen the stability when using more ground plane.

Ideally, one entire layer of PCB should be used as the ground plane. The best results are achieved when the entire ground plane is not broken, therefore one needs to avoid routing any signal onto this dedicated layer. The ground plane reduces trace inductance by canceling the magnetic field between the conductor and the ground plane. When there is no ground plane, unexpected parasitic inductance is easily introduced in the high speed circuitry. Figure B.2 shows how the ground plane can remove the output oscillation when there is stray inductance present at the inverting input of an op-amp.

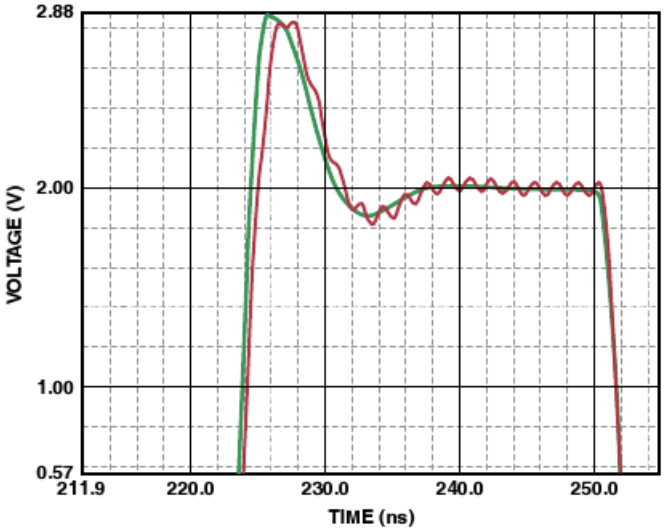

Figure B.2: Pulse response with (green) and without (red) ground plane (graph from [71]).

Nevertheless, there are some exceptions where adding a ground plane can cause instability. High speed op-amps will perform better if the ground plane is removed at the signal I/O pins. As mentioned before, adding a ground plane may introduce extra parasitic capacitance. Parasitic capacitance on the op-amp's output can lower the phase margin and cause instability. For non-inverting op-amp based amplifiers, the stray capacitance to ground at the non-inverting input can react with the source impedance, which causes the unintentional band limiting [73]. To reduce unwanted stray capacitance, the ground plane around the signal I/O pins of the op-amp should be removed to achieve the best op-amp performance. Besides the care of op-amps, the ground plane should be unbroken elsewhere on the PCB.

When laying out a board that includes both analog and digital circuitry, their ground planes should be kept separate when possible. Fast rising edges in digital circuitry create current spikes flowing in the ground plane. These current spikes can create noise that seriously interferes with the analog performance. The analog and digital ground should be tied at only one point, in order to minimise the interaction between the digital and analog ground currents.

B.3 Selection of External Components

When dealing with high frequency PCBs, external components need to be carefully selected and placed in order to ensure the performance of the high speed ICs.

Generally, components that have low reactance at high frequencies should be used. Surface mounted components work the best and allow a tight overall layout. Wire wound type resistors or capacitors should never be used in high frequency applications, as their leads can easily introduce parasitic capacitance as well.

A good surface mounted component has approximately 0.2 pF capacitance in shunt with the resistor. For resistor values > 10 kΩ, this parasitic capacitance can create a pole or a zero below 80 MHz that might affect the circuit performance. Resistor values should thus be kept as low as possible after taking loading into considerations.

B.4 Parasitic

In electronic circuits, the term ‘parasitic’ refers to the unavoidable and usually unwanted capacitive coupling between components, and the unwanted inductance of interconnecting wires that exist among the electronic circuits. They are the hidden stray capacitors and inductors that infiltrate high speed circuits. Parasitic capacitance and inductance can exist between the PCB traces, the IC pins, the ground plane, interaction between vias, and there are many other possibilities. Figure B.3(A) shows a typical schematic of a non-inverting op-amp. If parasitics are considered, the same circuit will look like Figure B.3(B). One can see the parasitics can really complicate the system, and may cause the circuit’s behavior to depart from its ideal performance.

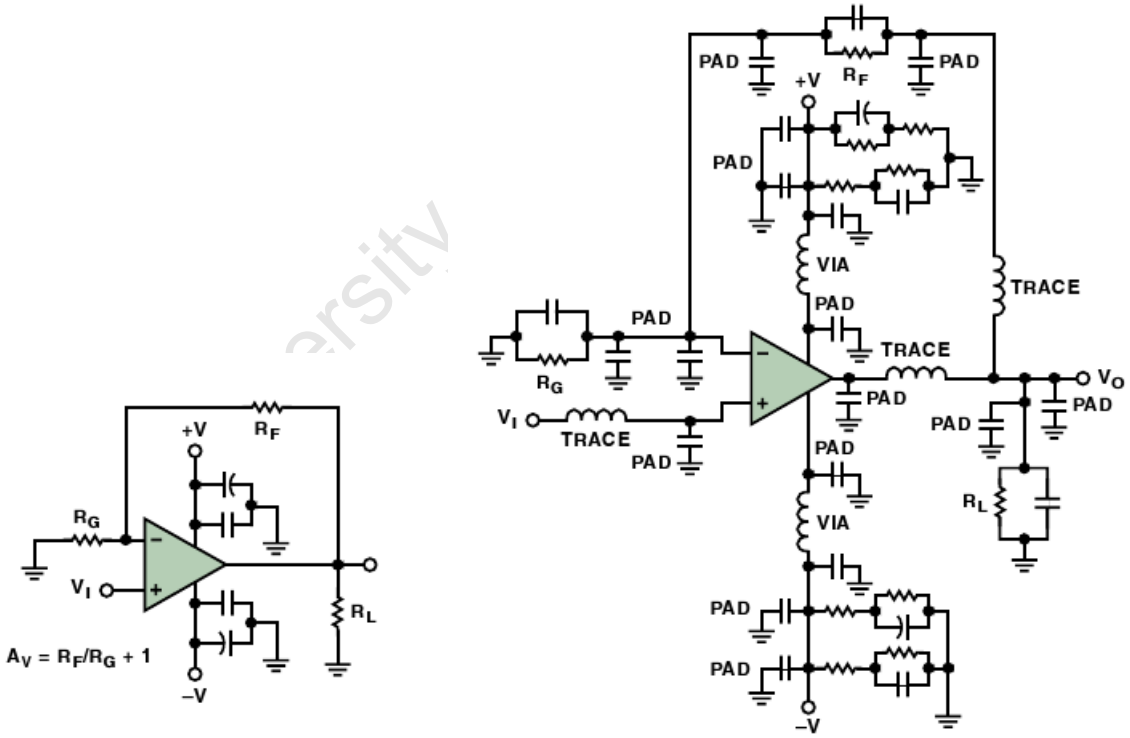

(A) (B)

Figure B.3: Typical op-amp circuit, as (A) designed and (B) with parasitic (images from [71]).

Parasitic does not need to be much to influence the circuit behavior. As shown in Figure B.4, if 1 pF of additional stray capacitance is presented at the inverting input of the op-amp, it can cause almost 2 dB of peaking in the bode plot. If enough capacitance is presented, it can even cause instability and oscillation.

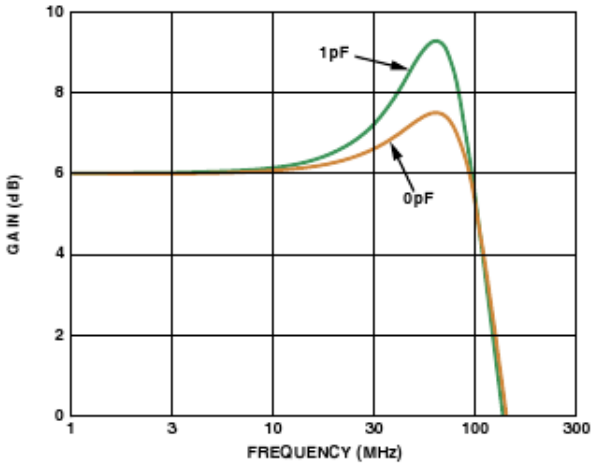

Figure B.4: Additional peaking caused by a 1 pF stray capacitance (graph from [71]).

One cannot eliminate parasitics completely, simply because the finite dimensions on lay-out configuration of electronic circuits. However, there are some general tips that we can follow to minimise parasitic capacitance and inductance.

- Increase the spacing between wires, to reduce trace to trace capacitance.
- Minimise the trace length, to reduce trace to ground capacitance.
- Place the external components that are connected to high speed ICs as close to it as possible, in order to minimise extra parasitic capacitance.
- In general, a 1 cm trace will contribute about 10 nH of inductance [71]. Therefore, one can minimise the parasitic inductance by minimising trace length and using short, wide traces instead. The lack of a ground plane can also be the reason for excessive parasitic inductance.
- Socketing a high speed IC is not recommended. The additional lead length and pin-to-pin capacitance introduced by the socket can create extremely troublesome IC performance. Soldering the ICs directly onto the board gives the best high frequency performance.

Appendix C

Data Acquisition Card

Figure C.1 and C.2 show the layout of the CB-68LP connector board and the pin out for NI PCI-6070E DAQ Card respectively. The information and figures below can be found in the PCI-6070E's datasheet [74] and on the National Instruments website.

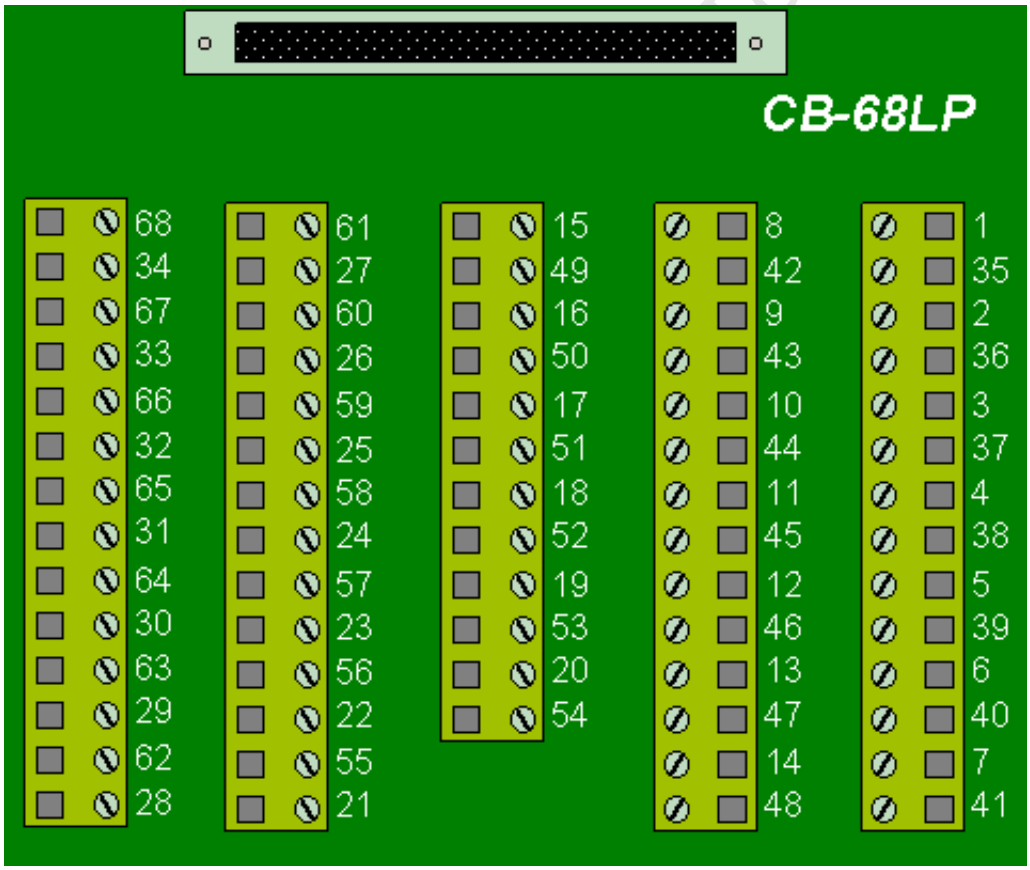

Figure C.1: Layout of CB-68LP connector board (diagram from[74]).

Figure C.2: Pin out for NI PCI-6070E DAQ Card (diagram from [74]).

Appendix D

Comedi Instruction

This appendix gives some basic instructions for installing the comedi drivers, and configuring them for use with the NI PCI-6070E card.

D.1 Using Linux Debian Archive

apt-get install the following:

- ‘comedi-source’ - Comedi kernel module source
- ‘libcomedi-dev’ - Development library for Comedi
- ‘libcomedi0’ - Library for Comedi
- ‘comedi-modules-2.6.20.1-slh-smp-2’ - comedi modules for Linux (kernel 2.6.20.1-slh-smp-2).

Read ‘/usr/src/modules/comedi/INSTALL’

Read ‘/usr/share/doc/comedi-source/README.Debian’

To compile modules for your particular kernel, run(One may have to install "apt-get install libtool" first):

- ‘apt-get update module-assistant auto-install comedi’
- Type ‘cd /usr/src/modules/comedi make install’

At this point the /dev/comedi0 etc devices do not exist, to create devices, from the directory: /usr/src/modules/comedi, type:

- ‘make dev’

One needs to use the ‘comedi_config’ command to configure the device. To configure a driver module for a particular device, check /usr/src/modules/comedi/Documentation/comedi/drivers.txt

- for NI PCI-6070E, type: ‘comedi_config /dev/comedi0 ni_pcimio’
- for USBDUX, type: ‘comedi_config /dev/comedi0 usbdux’

D.2 Using the Comedi website

- Go to http://www.comedi.org/download/
- Download the latest version of comedi source (comedi.tat.gz) and comedi library (comedilib.tar.gz)

Repeat the following for both comedi source and comedi library files:

- Unzip the zipped file, and save it to some other location (e.g. /Desktop/comedi/)
- Under the source directory (e.g. /Desktop/comedi), type ‘./configure’
- Type ‘make’
- Type ‘sudo make install’
- Type ‘make dev’

To configure the device, use the ‘comedi_config command’, for NI PCI-6070E card, type:

- ‘sudo comedi_config /dev/comedi0 ni_pcimio’

The command ‘dmesg’ can be used to check the kernal logs, in case of the event of failure.

Appendix E

MIT Transceiver Circuit Schematics

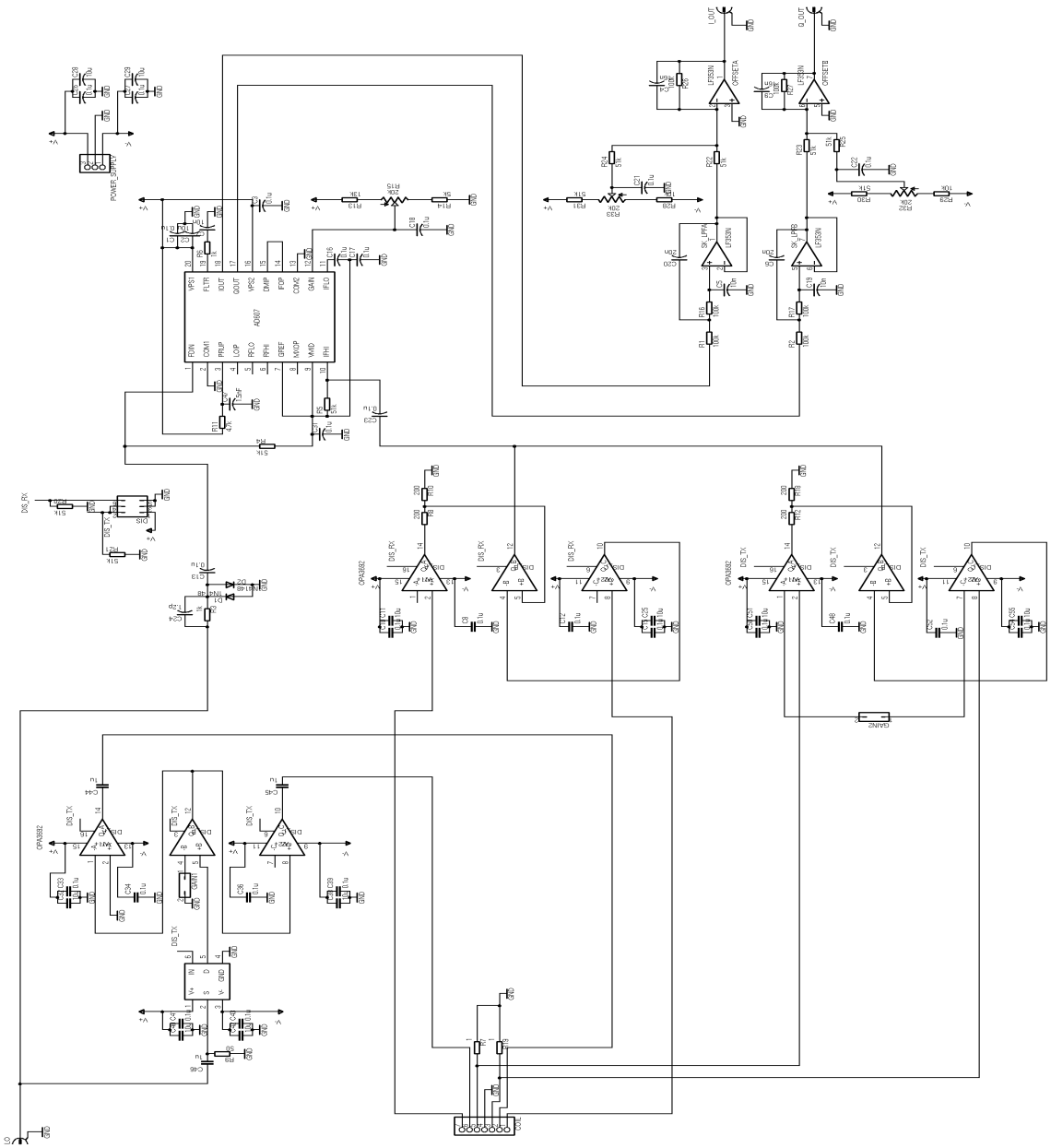

Figure E.1: MIT transceiver schematics.

Bibliography

[1] J.A. Simpson and E.S.C. Weine, editors. *The Oxford English Dictionary - 2nd edition*. Oxford : Clarendon Press, 1989.

[2] McGraw-Hill and Sybil P. Parker. *McGraw-Hill dictionary of scientific and technical terms - 6th edition, pages 1883*. 2003.

[3] David S. Holder. *Electrical impedance tomography : methods, history, and applications*. Bristol ; Philadelphia : Institute of Physics Pub., 2005.

[4] T Peyton. Industrial tomography - electrical tomography presentation slides for industrial applications.

[5] H Griffiths. Magnetic induction tomography. *Institute of Physics Publishing Meas. Sci. Technol.*, Vol. 12:pages 1126–1131, Dec. 2001.

[6] A V Korjenevsky and V A Cherepenin. Progress in realization of magnetic induction tomography. *Annals of the New York Academy of Sciences*, Vol. 873:pages 346–352, 1999.

[7] W Daily and A Ramirez. Environmental process tomography in the united states. *Chemical Engineering Journal And The Biochemical Engineering Journal*, Vol. 56, No. 3:pages 159–165, 1995.

[8] A J Wilkinson, E W Randall, T M Long, and A Collins. The design of an ert system for 3d data acquisition and a quantitative evaluation of its performance. *Meas. Sci. Technol.*, Vol. 17:pages 2088–2096, 2006.

[9] Fayaaz Ali Sattar. Rot detection in wooden poles using electrical impedance tomography (supervision under Dr. A J Wilkinson). Master's thesis, Department of Electrical Engineering, University of Cape Town, 2005.

[10] A J Peyton, Z Z Yu, and G M Lyon. An overview of electromagnetic inductance tomography: Description of three different systems. *Measurement Science & Technology*, Vol. 7, No. 3:pages 261–271, Mar 1996.

[11] A Korjenevsky, V Cherepenin, and S Sapetsky. Magnetic induction tomography: experimental realization. *Physiol. Meas.*, Vol. 21, No. 1:pages 89–94, 2000.

[12] I L Freeston and R C Tozer. Impedance imaging using induced currents. *Physiological Measurement*, Vol. 16, No. 3A:pages A257–A266, 1995.

[13] J C Tozer and R H Ireland D C Barber. Magnetic impedance tomography. *Annals Of The New York Academy Of Sciences*, Vol. 873:pages 353–359, 1999.

[14] S Levy, D Adam, and Y Bresler. Electromagnetic impedance tomography (EMIT): A new method for impedance imaging. *IEEE Transactions On Medical Imaging,*, Vol. 21, No. 6, 2002.

[15] Z Z Yu, A J Peyton, and L A Xu. Electromagnetic inductance tomography (EMT): sensor, electronics and image reconstruction algorithm for a system with a rotatable parallel excitation field. *IEE Proceedings-Science Measurement And Technology*, Vol. 145, No. 1:pages 20–25, Jan 1998.

[16] J G Webster, editor. *Electrical Impedance Tomography*. Adam Hilger, Bristol and New York, 1990.

[17] H Scharfetter, Helmut K Lackner, and J Rosell. Magnetic induction tomography: Hardware for multi-frequency in biological tissue. *Physiological Measurement*, Vol. 22, No. 1:pages 131–146, Feb 2001.

[18] C H Riedel, M A Golombeck, M von Saint-George, and O Dossel. Data acquisition system for contact-free conductivity measurement of biological tissue. *Proc. Int. Fed. Med. Biol. Eng. EMBEC02*, Vol. 3, Part 1:pages 86–87, 2002.

[19] Ze Liu, Min He, and Hanliang Xiong. Simulation study of the sensing field in electromagnetic tomography for two-phase flow measurement. *Flow Measurement and Instrumentation*, Vol. 16:pages 199–204, 2005.

[20] J Z Wang, C L Gong, G Y Tian, and G P Lucas. Numerical simulation modelling for velocity measurement of electromagnetic flow meter. *International Symposium on Instrumentation Science and Technology - Journal of Physics*, Vol. 48:pages 36–40, 2006.

[21] Simon Ramo, John R. Whinnery, and Theodore Van Duzer. *Fields and Waves in Communication Electronics - Third Edition*. John Wiley & Sons, Inc., 1994.

[22] Bhag Guru and Huseyin Hiziroglu. *Electromagnetic Field Theory Fundamentals - Second Edition*. Press Syndicate of the University of Cambridge, 2004.

[23] H Griffiths, W R Stewart, and W Gough. Magnetic induction tomography - a measuring system for biological tissues. *Annals Of The New York Academy Of Sciences*, Vol. 873:pages 335–345, 1999.

[24] W A Wan-Daud, A J Peyton, R Mackin, D Goss, E Crescenzo, N H Saunders, and H S Tapp. Addressing the difficulties in using inductive methods to evaluating human body composition. *Biometrie Humaine et Anthropologie*, Vol. 21, No. 1/2:pages 69–77, 2003.

[25] H Scharfetter, R Casanas, and J Rosell. Biological tissue characterization by magnetic induction spectroscopy (MIS): Requirements and limitations. *IEEE Transactions On Biomedical Engineering*, Vol. 50, No. 7:pages 870–880, Jun 2003.

[26] G M Lyon, Z Z Yu, A J Peyton, and M S Beck. Developments in electromagnetic tomography instrumentation. *Advances in Electrical Tomography (Digest No: 1196/143)*, pages 12/1–12/4, 1996.

[27] X Ma, S R Higson, A Lyons, and A J Peyton. Development of a fast electromagnetic induction tomography system for metal process applications. *Proc. 4th World Congress on Industrial Process Tomography (WCIPT4), Aizu, Japan*, pages 196–201, Sept 2005.

[28] X Ma, A J Peyton, S R Higson, A Lyons, and S J Dickinson. Hardware and software design for an electromagnetic induction tomography (EMT) system applied to high contrast metal process applications. *Meas. Science and Technology*, Vol. 17, No. 1:pages 111–118, 2006.

[29] W Q Yang and Peng Lihui. Image reconstruction algorithms for electrical capacitance tomography. *Meas. Sci. Technol.*, Vol. 14:pages R1–13, 2003.

[30] A J Peyton, M S Beck, A R Borges, J E de Oliveira, G M Lyon, Z Z Yu, M W Brown, and J Ferrerra. Development of electromagnetic tomography (EMT) for industrial applications. part 1: Sensor design and instrumentation. *Proc. 1st World Congress on Industrial Process Tomography*, pages 306–312, 1999.

[31] A R Borges, J E de Oliveira, J Velez, C Tavares, F Linhares, and A J Peyton. Development of electromagnetic tomography (EMT) for industrial applications. part 2: Image reconstruction and software framework. *Proc. 1st World Congress on Industrial Process Tomography*, pages 219–225, 1999.

[32] S Al-Zeibak and N H Saunders. A feasibility study of in vivo electromagnetic imaging. *Physics in Medicine and Biology,*, Vol. 38:pages 151–160, 1993.

[33] S Watson, R J Williams, H Griffiths, W Gough, and A Morris. Magnetic induction tomography: phase versus vector-voltmeter measurement techniques. *Physiol. Meas.*, Vol. 24:pages 555–564, 2003.

[34] D Goss, R O Mackin, E Crescenzo, H S Taoo, and A J Peyton. Development of electromagnetic inductance tomography (EMT) hardware for determining human

body composition. *3rd World Congress on Industrial Process Tomography, Banff, Canada*, pages 377–383, 2003.

[35] H Scharfetter H, P Riu, and M Populo. Sensitivity maps for low-contrast perturbations within conducting background in magnetic induction tomography. *Physiological Measurement*, Vol. 23, No. 1:pages 195–202, Feb. 2002.

[36] A V Korjenevsky. Electric field tomography for contactless imaging of resistivity in biomedical applications. *Physiol. Meas.*, Vol. 25, No. 1:pages 391–401, 2004.

[37] A Korjenevsky, V Cherepenin, and S Sapetsky. Magnetic induction tomography - new imaging method in biomedicine. *Proc. 2nd World Congr. Industrial Process Tomography (Hannover)*, pages 240–246, 2001.

[38] C Ktistis, R O Mackin, H S Tapp, and A J Peyton. Initial experimental results from an electromagnetic induction tomography system with low conductivity materials. *Proc World Congress Industrial Progress Tomography, Banff, Canada*, pages 567–581, 2005.

[39] H Scharfetter, R Merwa, and K Pilz. A new type of gradiometer for the receiving circuit of magnetic induction tomography. *Physiological Measurement*, Vol. 26 , No. 2:pages S307–S318, 2005.

[40] Z Z Yu, A J Peyton, and M S Beck. Imaging system based on electromagnetic tomography (EMT). *Electronics Letters*, Vol. 29, No. 7:pages 625–626, 1993.

[41] M H Pham, Y Hua, and N B Gray. Eddy current tomography for metal solidification imaging. *Proc. 1st World Congress on Industrial Process Tomography, Buxton, UK*, pages pages 451–458, 1999.

[42] J A Coveney, M H Pham, A K Kyllo, and N B Gray. Comparison of modelling approaches for the eddy current problem as applied to the geometry of a taphole. *Measurement Science & Technology*, Vol. 17, Issue 2:pages 340–352, 2006.

[43] S Ramli and A J Peyton. Feasibility study for planar array electromagnetic inductance tomography. *Proc. 1st World Congress on Industrial Progress Tomography, Buxton, UK*, 1999.

[44] D J SADLER and Chong H AHN. On-chip eddy current sensor for proximity sensing and crack detection. *Sensors and actuators. A, Physical*, Vol. 91:pages 340–345, 2001.

[45] X Ma and A J Peyton. Eddy current measurement of the electrical conductivity and porosity of metal foams. *IEEE Transactions On Instrumentation And Measurement*, Vol. 55, No. 2:pages 570–576, Apr. 2006.

[46] Gwan Soo Park and Dong Seok Kim. Development of a magnetic inductance tomography system. *IEEE Transactions On Magnetics*, Vol. 41, No. 5:pages 1932–1935, 2005.

[47] Z Z Yu, G M Lyon, S Al-Zeibak, and M S Beck. A review of electro-magnetic tomography at UMIST. *Institute of Electrical Engineers*, 1995.

[48] Nevzat G Gencer and M Nejat Tek. Electrical conductivity imaging via contactless measurements. *IEEE Transactions On Medical Imaging*, Vol. 18, No. 7:pages 617–626, 1999.

[49] H Griffiths W Gough S Watson, R J Williams and A Morris. A transceiver for direct phase measurement magnetic induction tomography. *23rd Annual International Conference of the IEEE Engineering in Medicine and Biology Society*, pages 25–27, Oct. 2001.

[50] S Watson, R J Williams, H Griffiths, W Gough, and A Morris. Frequency downconversion and phase noise in MIT. *Physiol. Meas.*, Vol. 23:pages 189–194, 2002.

[51] S Watson, C H Igney, O Dossel, R J Williams, and H Griffiths. A comparison of sensors for minimizing the primary signal in planar-array magnetic induction tomography. *Physiol. Meas.*, Vol. 26:pages S319–S331, 2005.

[52] S Tumanski. Induction coil sensors - a review. *Meas. Sci. Technol.*, Vol. 18:pages R31–R46, 2007.

[53] Robert Schetgen, Larry Wolfgang, Joel P Kleinman, and James E Kearman, editors. *The ARRL handbook for radio amateurs*. The American Radio Relay League, 1994.

[54] AD8348 - 50 MHz to 1000 MHz Quadrature Demodulator. Technical report, Analog Devices, Inc., 2006.

[55] AD8333 - DC to 50 MHz, Dual I/Q Demodulator and Phase Shifter. Technical report, Analog Devices, Inc., 2006.

[56] AD607 - low power mixer 3 V receiver if subsystem. Technical report, Analog Devices, Inc., 2002.

[57] Paul Horowitz and Winfield Hill. *The Art of Electronics - Second Edition*. Cambridge University Press, 1989.

[58] Texas instruments application report: Analysis of the sallen-key architecture. Technical report, Texas Instruments Incorporated, 2002.

[59] TLV5630 - 8 Channel, 12-/10-8- bit, 2.7 V to 5.5 V Low Power Digital to Analog Converters With Power Down and Internal Reference. Technical report, Texas Instruments Incorporated, 2005.

[60] National Instruments Corporation. Ni pci-6070e/cb-68lp academic starter kit. Technical report, http://sine.ni.com/nips/cds/view/p/lang/en/nid/13116.

[61] Maintainer: David Schleef, Frank Mori Hess, and Ian Abbott. Comedi - control and measurement interface. Technical report, http://www.comedi.org.

[62] C Ktistis, D W Armitage, and A J Peyton. Calculation of the forward problem for absolute image reconstruction in MIT. *Physiol. Meas.*, Vol. 29:pages S455–S464, 2008.

[63] M Soleimani, W R B Lionheart, A J Peyton, and X Ma. A 3D inverse finite element technique applied to experimental magnetic induction tomography data. *4th World Congress on Industrial Process Tomography, Aizu, Japan*, pages 1054–1059.

[64] M Soleimani and William R B Lionheart. Absolute conductivity reconstruction in magnetic induction tomography using a nonlinear method. *IEEE Transactions On Medical Imaging*, Vol. 25:pages 1521–1530, Dec. 2006.

[65] R Merwa, K Hollaus, P Brunner, and H Scharfetter. Solution of the inverse problem of magnetic induction tomography (MIT). *Physiol. Meas.*, Vol. 26:pages S241–S250, 2005.

[66] R Merwa, P Brunner, A Missner, K Hollaus, and Hermann Scharfetter. Solution of the inverse problem of magnetic induction tomography (MIT) with multiple objects: analysis of detectability and statistical properties with respect to the reconstructed conducting region. *Physiol. Meas.*, Vol. 27:pages S249–S259, 2006.

[67] M Soleimani. Sensitivity maps in three-dimensional magnetic induction tomography. *Insight No 1 January 2006*, Vol. 48, No. 1:pages 39–44, Jan. 2006.

[68] M Soleimani, William R B Lionheart, A J Peyton, Xiandong Ma, , and Stuart R. Higson. A three-dimensional inverse finite-element method applied to experimental eddy-current imaging data. *IEEE Sensors Journal Transactions on Magnetics*, Vol. 42:pages 1560–1567, May 2006.

[69] K-H Hauer, R Potthast, and M Wannert. Algorithms for magnetic tomography - on the role of a priori knowledge and constraints. *Inverse Problems*, Vol. 24:pages 1–18, 2008.

[70] R R Casanas, H Scharfette, A Altes, and J Rosell. Magnetic induction system for noninvasive measurement of susceptibility and conductivity of biological tissues. *Proc. 11th Conf. on Electrical Bio-Impedance*, pages 623–626, 2001.

[71] J Ardizzoni. A practical guide to high-speed printed-circuit-board layout. Technical report, Analog Dialogue 39-09, 2005.

[72] D Brockman and A Williams. Ground rules for high-speed circuits. Technical report, Analog Devices, Inc.

[73] OPA3692 - triple, wideband, fixed gain video buffer amplifier with disable. Technical report, Texas Instruments Incorporated, 2002.

[74] NI, DAQ E series user manual. Technical report, National Instruments Corporation, Feb. 2007.

[75] O Biro. Edge element formulations of eddy current problems. *Comput. Methods Appl. Mech. Engrg.*, Vol. 169:pages 391–405, 1999.

[76] V Cherepenin, A Karpov, A Korjenevsky, V Kornienko, A Mazaletskaya, D Mazourov, and D Meister. A 3D electrical impedance tomography (EIT) system for breast cancer detection. *Physiol. Meas.*, Vol. 22:pages 9–18, 2001.

[77] O Deblecker, J Lobry, and C Broche. Use of transmission-line modelling method in FEM for solution of nonlinear eddy-current problems. *IEE Proc.Sci. Meas. Technol.*, Vol. 145, No. 1:pages 31–38, Jan. 1998.

[78] W Gough. Circuit for the measurement of small phase delays in MIT. *Physiol. Meas.*, Vol. 24:pages 501–507, 2003.

[79] H Griffiths, W Gough, S Watson, and R J Williams. Residual capacitive coupling and the measurement of permittivity in magnetic induction tomography. *Physiol. Meas.*, Vol. 28:pages S301–S311, 2007.

[80] Min He, Ze Liu, Xiao Yan Xu, Han Liang Xiong, and Ling an Xu. Application of perturbation methods to image reconstruction in electromagnetic tomography. *Flow Measurement and Instrumentation*, Vol. 16:pages 205–210, 2005.

[81] K Hollaus and O Biro. Comparison of tetrahedral edge finite-elements using different potential formulations. *IEEE Transactions on Magnetics*, Vol. 41, No. 5:pages 1676–1679, May 2005.

[82] Basak Ulker Karbeyaz and Nevzat G. Gencer. Electrical conductivity imaging via contactless measurements: An experimental study. *IEEE Transactions On Medical Imaging*, Vol. 22, No. 5:pages 627–635, 2006.

[83] A V Korjenevsky and T S Tuykin. Electric field tomography: setup for single channel measurements. *Physiol. Meas.*, Vol. 28:pages S279–S289, 2007.

[84] Q Marashdeh, W Warsito, L-S Fan, and F L Teixeira. A multimodal tomography system based on ECT sensors. *IEEE Sensors Journal*, Vol. 7:pages 426–433, Mar. 2007.

[85] H Scharfetter, K Hollaus, J Rosell-Ferrer, and R Merwa. Single-step 3-D image reconstruction in magnetic induction tomography: Theoretical limits of spatial resolution and contrast to noise ratio. *Annals of Biomedical Engineering*, Vol. 34, No. 11:pages 1786–1798, Nov. 2006.

[86] W Yin and A J Peyton. A planar EMT system for the detection of faults on thin metallic plates. *Meas. Sci. Technol.*, Vol. 17:pages 2130–2135, 2006.